INAUGURAL – DISSERTATION

zur

Erlangung der Doktorwürde

der

Gesamtfakultät für Mathematik, Ingenieur- und Naturwissenschaften

der

Ruprecht-Karls-Universität Heidelberg

Vorgelegt von

Jan Lukas Scheiderer (M.Sc.)

Tag der mündlichen Prüfung:

29. November 2022

Kinesin-1 stepping dissected with MINFLUX and MINSTED tracking

–

Spontaneous blinkers for live-cell MINFLUX imaging

Gutachter: Prof. Dr. Joachim P. Spatz

Prof. Dr. Dr. h. c. mult. Stefan W. Hell

The works of the Lord are great, sought out of all them that have pleasure therein.

Psalm 111:2 KJV

Abstract

The fluorescence-based nanoscopy methods MINFLUX and MINSTED are currently revolutionizing the field of imaging and single molecule tracking by achieving molecular spatial precision with low photon numbers. Using a polymer-based *in vitro* assay with strongly reduced fluorescence background, I identified MINFLUX-compatible spontaneously blinking fluorophores by quantifying their blinking properties. Due to the spontaneous blinkers being live-cell compatible and having few-milliseconds-short on-events, I expect them to advance the imaging field by drastically accelerating MINFLUX measurements. The main focus of this work, however, is the application of the nanoscopy methods MINFLUX and MINSTED for tracking of the motor protein kinesin-1. Requiring an only ~1 nm small fluorophore as label, they are inherently less artefact-prone than established techniques which require the attachment of comparatively large beads for a similar spatio-temporal resolution. With an improved interferometric MINFLUX approach, we successfully resolved regular steps and substeps of the kinesin-1 stalk and heads. By discovering that ATP binds to the motor in the one-head-bound state and is hydrolyzed in the two-head-bound state, we aim to solve a long-standing controversy in the field. Furthermore, we deduced that when the rear head of kinesin-1 detaches form the microtubule, it rotates around its front into a rightward-displaced unbound state. In conjunction with an observed stalk rotation, I concluded the motor to walk in a symmetric hand-over-hand fashion. Finally, we successfully resolved the stepping of kinesin-1 with MINSTED, confirming many findings from the MINFLUX experiments and observing motor sidestepping and protofilament switching. These findings will prove helpful in developing treatments for diseases linked to malfunction of kinesins. Beyond that, this thesis establishes MINFLUX and MINSTED for the tracking of dynamic biological processes on the single molecule level.

Zusammenfassung

Die fluoreszenzbasierten Nanoskopiemethoden MINFLUX und MINSTED revolutionieren derzeit die Bereiche von Bildgebung und Einzelmolekülverfolgung, indem sie mit geringen Photonenzahlen eine molekulare räumliche Auflösung erreichen. Mit Hilfe eines polymerbasierten in-vitro-Tests mit stark reduziertem Fluoreszenzhintergrund ermittelte ich MINFLUX-kompatible spontan blinkende Fluorophore, indem ich ihre Blinkeigenschaften quantifizierte. Da die spontanen Blinker mit lebenden Zellen kompatibel sind und kurze Einschaltzeiten von wenigen Millisekunden haben, erwarte ich, dass sie das Forschungsfeld der Bildgebung durch drastisch beschleunigte MINFLUX-Messungen voranbringen werden. Der Hauptfokus dieser Arbeit ist jedoch die Anwendung der Nanoskopiemethoden MINFLUX und MINSTED für die Einzelmolekülverfolgung des Motorproteins Kinesin-1. Indem sie nur einen ~1 nm kleinen Fluoreszenzfarbstoff als Markierung benötigen, sind sie von Natur aus weniger anfällig, Messartefakte zu erzeugen, als etablierte Techniken, die für eine ähnliche räumlich-zeitliche Auflösung das Anbringen eines vergleichsweise großen Kügelchens voraussetzen. Mit einem verbesserten interferometrischen MINFLUX-Ansatz gelang es uns, sowohl regelmäßige Schritte als auch Teilschritte des Stiels und der Köpfe von Kinesin-1 aufzulösen. Durch die Entdeckung, dass ATP bindet, wenn nur einer der Köpfe gebunden ist, und hydrolysiert wird, wenn beide Köpfe gebunden sind, versuchen wir, eine seit langem bestehende Kontroverse des Forschungsfeldes zu lösen. Darüber hinaus fanden wir heraus, dass sich der hintere Kopf von Kinesin-1, nachdem er sich vom Mikrotubulus abgelöst hat, um seine Vorderseite dreht und in einen nach rechts verschobenen, ungebundenen Zustand übergeht. In Verbindung mit der beobachteten Rotation des Stiels folgerte ich, dass der Motor in einer symmetrischen Hand-über-Hand-Weise läuft. Abschließend gelang es uns, das Laufverhalten von Kinesin-1 mit MINSTED zu untersuchen, wobei wir viele Ergebnisse der MINFLUX-Experimente bestätigen und das Ausweichen des Motors und Protofilamentwechsel beobachten konnten. Diese Erkenntnisse werden bei der Entwicklung von Therapien für Krankheiten, die durch eine Fehlfunktion von Kinesinen verursacht werden, hilfreich sein. Vor allem jedoch etabliert diese Arbeit MINFLUX und MINSTED für die Verfolgung dynamischer biologischer Prozesse auf der Ebene einzelner Moleküle.

Acknowledgements

In the following, I would like to thank everyone involved in my academic path leading up to this thesis.

I am grateful to Prof. Stefan W. Hell for letting me join his group and work on exciting topics with amazing nanoscopy techniques. Thank you for interesting insights into the scientific community and motivating me to focus on the bigger picture. I appreciate your creativity and am very glad that you approved of my wish to start the protein-tracking project using MINFLUX.

I thank Prof. Joachim P. Spatz for being my first referee and taking the time and effort of examining my thesis. Likewise, I would like to thank the other examiners for being part of my examination committee.

I acknowledge Dr. Mariano Bossi, Dr. Alexey Butkevich and M.Sc. Michael Remmel for their contributions to the spontaneously blinking fluorophore project. Alexey, thank you for designing and synthesizing the fluorophores. Mariano, thank you for writing and re-writing the Matlab scripts and helping me enter the single molecule field. Thanks also for letting me work so independently, but being open for scientific discussion when needed. Mitsch, thank you for picking up and finishing the project with amazing live-cell MINFLUX images after I decided to switch to the kinesin-1 tracking project. Also, thanks a lot for letting me use your setup – and for re-aligning it and fixing it whenever it caused problems.

I acknowledge M.Sc. Otto Wolff, Dr. Tobias Engelhardt, Dr. Hans Engelhardt and Dr. Jessica Matthias for their contributions to the kinesin-1 MINFLUX tracking project. Otto (aka Jan 'Flotto-Otto' Woolf), I really enjoyed working with you on this project. I appreciate your drive to continuously improve the MINFLUX setup and our personal conversations during measurements and sample preparation. Tobi and Hans, thanks a lot for your work on the setup(s) in the group. It is amazing seeing your (probably hereditary) compassion for microscopes. Jessi, thanks for letting me work so freely on the project. I appreciate your drive and your kind nature. Thanks also for letting me use your setup in the beginning.

I acknowledge M.Sc. Henrik von der Emde and Dr. Michael Weber for their contribution to the kinesin-1 MINSTED tracking project. Henrik, thanks for showing me around the labs and being my primary contact person in Göttingen. I really enjoyed your happy nature. Michael, thanks for also re-activating your setup.

I thank Dr. Richard Lincoln for (partially) proof-reading my thesis. Ricky, I really cherished our deep conversations about all kinds of topics during lunch. I was often motivated by your compassion for science.

I thank M.Sc. Jasmine Hubrich for the preparation of cells.

I also thank the rest of Optical Nanoscopy group for all the interesting conversations and assistance during the past few years.

I acknowledge Dr. Miroslaw Tarnawski and protein expression facility for expressing various proteins for my projects. Mirek, thank you for your kind help and for working so fast and reliably.

I acknowledge Dr. Sebastian Fabritz and the mass sprectrometry facility for recording the mass spectrometry data.

I thank my former teachers Herr Schick and Frau Bayer for instilling/nurturing my early interest in science.

Furthermore, I want to express my gratefulness to my family and friends.

Tim, Rahel and Gideon, thanks for your hospitable and faith-based support during the writing phase. I am so thankful to know you.

Mama and Papa, thanks for raising me and putting me first so many times. I cannot grasp how much you contributed to this thesis by always supporting me and being confident in my plans.

Christian, Lisa and Jannis, I am thankful for all the time we had together before my life of lectures and research. I am looking forward to all our (family) reunions in the future.

La, I am immensely happy and deeply grateful to call you my beloved wife. You constantly enrich me with your whole nature and I cherish all the time I have with you. You support me in my work, faith and everyday life. Coco and Cara, miaooo.

Last but certainly not least, I dedicate this thesis to my savior Jesus Christ for giving me a purpose in life that is even greater than science. And for creating kinesin.

Table of Contents

Introduction

I.1 Kinesin-1 fundamentals

Kinesins are motor proteins that are essential for the directional transport of cargo along microtubules in cells. So far, there are 15 different families known that form the kinesin superfamily. The processive kinesins consist of a motor domain, a neck linker, a stalk and a cargo-binding domain. The first kinesin was discovered in 1985, named kinesin-1 and is the arguably best-studied member of the kinesin superfamily[1]. There are three isoforms of kinesin-1 (KIF5A, KIF5B, KIF5C), which are responsible for the transport of vesicles, synaptic vesicle precursers, lysosomes, organelles, protein complexes and neurofilament proteins[2] towards the plus-end of microtubules in the cell periphery, called anterograde transport. A plethora of diseases is likely at least partially caused by the malfunction of kinesin-1, like Alzheimer's disease[3], amyotrophic lateral sclerosis (ALS)[4], cortical dysplasia[5], Huntington's disease[6], hereditary spastic paraplegia[7] and cancer[8], caused by mutations in the motor or its premature detachment due to blockages on microtubules. Better understanding of the detailed transport mechanism would be instrumental in creating therapies and drugs for patients.

Kinesin-1 typically exists in a dimeric form, where the long alpha-helical stalk regions of two kinesin heavy chain (KHC) monomers intertwine to form a stable coiled-coil. Cargo attaches to the C-terminal end of the stalk, either directly to the tail, via the kinesin light chain (KLC) or via adaptor/scaffold proteins. In a dimer, two motor domains, commonly called 'heads', are connected to the stalk via neck linkers, flexible chains consisting of 14 amino acids (as illustrated in Fig. I1).

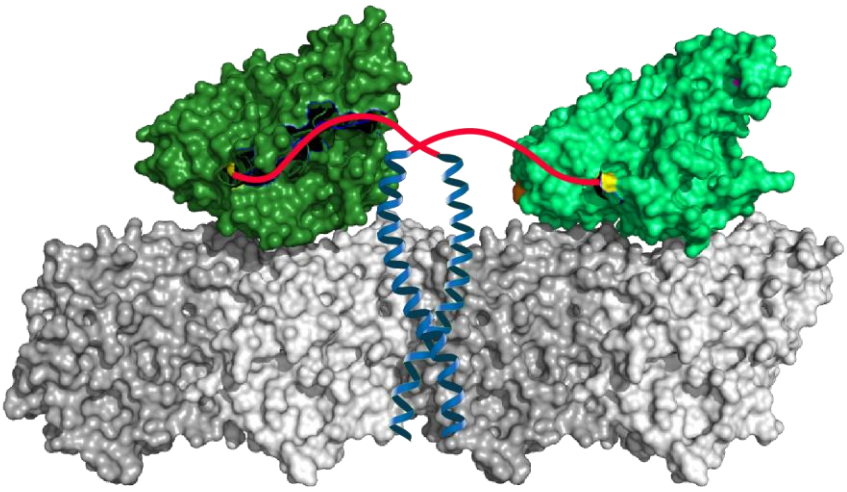

Figure I1: Visualization of kinesin-1 (rear head: dark green; front head: bright green) on a microtubule (grey). The heads are connected via the neck linkers (red) to the coiled-coil stalk (blue, only partially shown). At the end of the full stalk, cargo can attach.

The heads, which are very similar across the kinesin superfamily, each have a microtubule-binding domain and a catalytic center for the binding and hydrolysis of adenosine triphosphate (ATP), which

provides the chemical energy for the directed transport. When the head is in its ATP-bound or nucleotide-free (apo) state, it has a high affinity to bind to the microtubule, whereas it has a low microtubule affinity when it is adenosine diphosphate (ADP)-bound after hydrolysis[9]. By binding of ATP to the catalytic site, the so-called switch II helix moves like a piston, allowing the neck linker on the other side of the head to dock to the head, as interpreted from crystal structures, pointing the neck linker in walking direction[2].

I.2 Tracking techniques

Kinesin heads attach via their microtubule-binding domain to the outside of microtubules (which consist of ~13 protofilaments with alternating alpha- and beta-tubulins) at the groove in the middle of a tubulin dimer. By binding and hydrolyzing ATP, the heads are alternatingly stepping forward, building up forces large enough to carry cargo along the microtubule track. Tracking of silica beads (diameter of ~200 nm) revealed, that kinesin-1 takes ~8 nm steps, which is the distance between binding sites on the protofilament track, and consumes one ATP molecule per step[10]. The velocity of the motor protein is increasing strongly with greater ATP concentrations, with kinesin-1 taking roughly one step per second for ~1 uM ATP, but having a velocity of a few hundred nanometers per second at physiological ATP concentrations[11]. Individual kinesin-1 motors can move a few micrometers before detaching and teams of motors attached to the same cargo can transport it over even longer distances.

But despite kinesin-1, the founding member of the kinesin superfamily, being heavily studied with different techniques, many parts of its stepping mechanism remain contested. For example, the question, in which states ATP binds and is hydrolyzed, respectively, has not been answered conclusively and whether kinesin rotates while walking remains elusive.

Besides the state where both kinesin heads are microtubule-bound, Förster-resonance energy transfer (FRET) experiments have predicted a distinct state, in which one of the heads is unbound by measuring relative distances between regions on the kinesin heads[12, 13]. Experiments of bead-based tracking techniques with a sufficient spatio-temporal resolution have confirmed the existence of this state. An optical trap experiment tracking germanium nanospheres (diameter of ~70 nm) attached to the stalk observed 4 nm substeps and two independent scattering-based experiments of large gold beads (diameter ≥30 nm) attached to the kinesin head directly identified the unbound state of the labeled head in-between binding sites. But strikingly, the latter methods derived conflicting results as to whether ATP binds to the catalytic center when both heads or only one head are microtubule-bound. They also disagreed on the state during which ATP hydrolysis occurs.

Simulations have predicted that due to the large bead, whose volume is >200-times larger than that of the kinesin head, the attachment position of the label leads to these different conclusions[14]. Furthermore, the bead, which needs to be so large to yield a sufficient spatio-temporal resolution, probably interacts with its surrounding[15].

A much more suitable label would be a drastically smaller fluorophore with a diameter of ~1 nm. Fluorescence-based tracking has been performed with the camera-localization-based Fluorescence Imaging with One-Nanometer Accuracy (FIONA) technique, which resolved the 16 nm steps of fluorescently labeled kinesin-1 heads[16]. However, due to its comparably low time resolution of a few hundreds of milliseconds, the motors had to be slowed down drastically by using ATP concentrations about a thousand times lower than in a cell and substeps were thus not observable.

I.3 Fluorescence microscopy

Fluorescence-based microscopy techniques are based on the principle that incident photons excite the delocalized π-electron system of a fluorophore molecule, bringing it from the singlet ground state (S_0) to a singlet excited state (e.g. S_1), as shown in the Jablonski diagram (Fig. I2). According to Kasha's rule, the system usually relaxes into its lowest-energy vibronic level in the S_1 state, before typically retuning to the ground state (S_0) with a delay of a few nanoseconds and simultaneously emitting a photon with a longer wavelength than that of the incident one. This wavelength change is called Stokes shift and is caused by the system's energy loss when the S_1 state relaxes into its lowest-energy state. The emitted photon can be detected and used to localize the fluorophore. This $S_0 \rightarrow S_1$ cycle can repeated until the S_1 state undergoes intersystem-crossing into a 'dark', long-lived triplet state (T_1), causing interrupted fluorescence emission ('blinking'). From T_1, the system can return into the ground state via a forbidden emission of a phosphorescent photon or via a second intersystem-crossing process. This return to S_0 can be accelerated by reaction with triplet (ground-state) oxygen ($^3O_2$) present. However, this produces singlet oxygen ($^1O_2$), a reactive oxygen species (ROS) that can react with the fluorophore and interrupt its conjugated delocalized π-electron system, irreversibly rendering the fluorophore non-fluorescent, which is called bleaching. Therefore, for achieving a stable and long-term emission of the fluorophore, oxygen is often removed from the sample, either technically or using an oxygen scavenger system (OSS) consisting of oxygen-consuming enzymes. An alternative to quickly return the system from T_1 to S_0 is the use of a reducing and oxidizing system (ROXS), a combination of reducing and oxidizing chemicals that, via an intermediate R^+/R^- state, take away the excitation energy of T_1 to yield its S_0 state. The fluorescence cycle ends when the fluorophore is irreversibly bleached during an excited state.

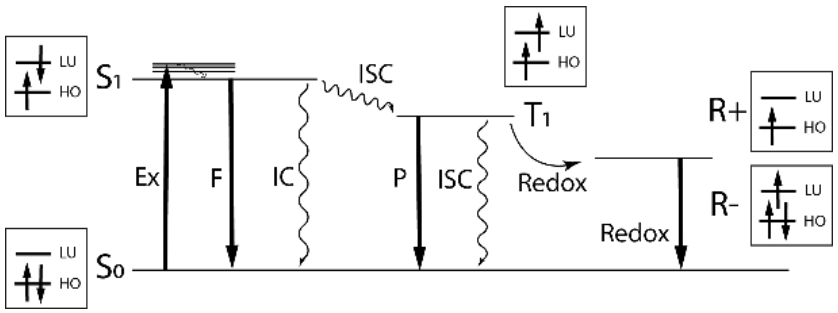

Figure I2: Jablonski diagram of a fluorophore with excitation (Ex), fluorescence (F), internal conversion (IC), intersystem crossing (ISC), phosphorescence (P), reduction/oxidation reaction (Redox), oxidized state (R+), reduced state (R-), highest occupied molecular orbitals (HOMO) and lowest unoccupied molecular orbitals (LUMO).

I.4 Widefield microscopy

In a widefield measurement, the emission of the fluorophore is directed onto a camera, which allows its localization. In confocal measurements, an excitation laser beam is focused to a spot which is scanned over the region of interest. If it scans over a fluorophore, the latter gets repeatedly excited and emits a fluorescent photon when returning to the ground state. The emitted photon is detected and used to localize the fluorophore. But the spatial resolution of both methods is diffraction-limited according to the Abbe limit. It states that the smallest resolvable distance d between emitters is

$$d_{abbe} = \frac{\lambda}{2\mathrm{n}*\sin\alpha} = \frac{\lambda}{2NA} \qquad \text{(eq. 1)}$$

where n is the refractive index of the medium, α is the half-angle of the light beam cone and $NA = n * sin(\alpha)$ is the numerical aperture (with a typical value of ≤1.5). Therefore, with for instance an incident light wavelength of ~600 nm, the lateral distance between two emitters needs to be at least ~200 nm in order to discern them in widefield or confocal measurements. The details of most biological structures are significantly smaller and hence not resolvable with these techniques. Electron microscopy is able to resolve biological structures with sub-nanometer resolution, but tracking and live-cell imaging is not possible with it, as samples must be fixed for the measurement.

I.5 Deterministic STED nanoscopy

The diffraction-limit was broken with the advent of fluorescence-based diffraction-unlimited ('super-resolution') techniques. The first super-resolution technique to break the diffraction limit in biological samples was stimulated emission depletion (STED). Its basic concept is that with a first laser pulse, all fluorophores within a diffraction-limited spot are excited, but by superimposing a second, delayed pulse of a red-shifted wavelength, stimulated emission of most fluorophores is triggered deterministically, bringing them back into their ground state (as illustrated in Fig. I3). By shaping the stimulated emission pulse to e.g. a doughnut shape with minimal intensity in its center, only fluorophores in the periphery are depleted and those in the center can fluoresce. For STED, the improved smallest resolvable distance between emitters is given by

$$d_{sted} = \frac{d_{abbe}}{\sqrt{1+\frac{I}{I_{sat}}}} = \frac{\lambda}{2n*\sin\alpha\sqrt{1+\frac{I}{I_{sat}}}} = \frac{\lambda}{2NA\sqrt{1+\frac{I}{I_{sat}}}} \quad \text{(eq. 2)}$$

where I is the maximal intensity of the depletion pattern and I_{sat} is the intensity at which the probability of fluorescence emission is reduced to a half. By increasing the applied intensity I, lateral resolutions down to ~20 nm are possible. STED has been employed heavily for resolving various biological structures in detail, but also for some use in tracking. Its spatio-temporal resolution is usually reported to be >10 nm within 1 second[17, 18], but with ultrafast STED nanoscopy, a spatio-temporal resolution of ~70 nm within ~8 ms was achieved[19].

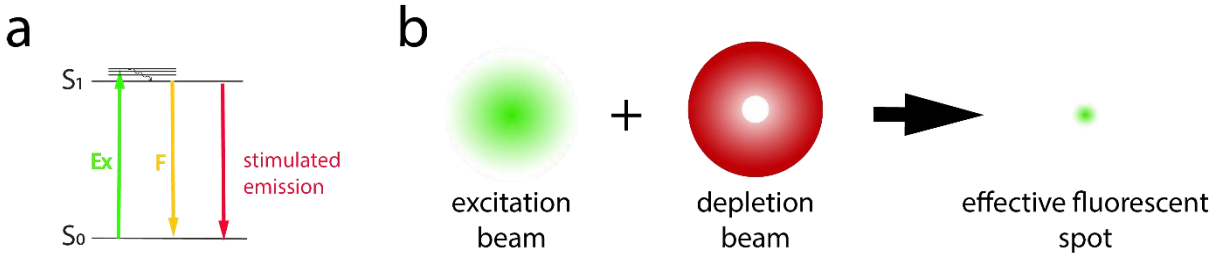

Figure I3: Concept of stimulated emission depletion (STED) (a) A fluorophore in an excited, fluorescent S_1 state can be depleted by stimulated emission. (b) By overlaying an excitation beam with a doughnut-shaped depletion laser, a diffraction-unlimited effective fluorescent spot is achieved.

I.6 Stochastic nanoscopy

Another way to image densely labeled (biological) structures with diffraction-unlimited resolution is with stochastic super-resolution techniques like Stochastic Optical Reconstruction Microscopy (STORM) or Photoactivated Localization Microscopy (PALM). In STORM, fluorophores are employed that transition between a short fluorescent and a long non-emissive state, so that at maximum one fluorophore per diffraction-limited spot is emissive at a given time and hence can be precisely localized (as illustrated in Fig. I4). In PALM, all fluorophores are inactive in the beginning and a small subset is activated, so that not more than one emitter is active per diffraction-limited spot. After the emitters are localized and bleached, the next subset is activated and so on. In both techniques, the individual emitters can then, in an ideal, background-free case, be localized by centroid fitting with a localization precision of

$$\sigma_{storm/palm} = \frac{s}{\sqrt{N}} \quad \text{(eq. 3)}$$

where s is the standard deviation of the point-spread function (PSF), the pattern resulting from the spreading of the image of a point-like object by the optical imaging system, and N is the number of the emitter's fluorescence photons detected by the camera. A super-resolved image can be reconstructed by determining the positions of active fluorophores in each video image and by overlaying them in the end. With a typical s of 300 nm, a lateral resolution of ~10 nm can theoretically be achieved for ~1000 photons.

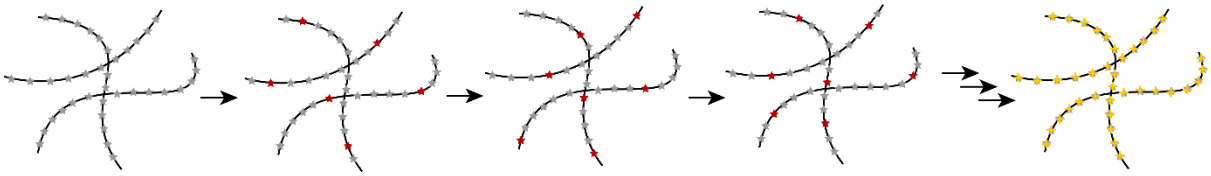

Figure I4: Concept of Stochastic Optical Reconstruction Microscopy (STORM). A small subset of 'dark' fluorophores (grey) is brought into a 'bright' state and localized. By repeating this process, all fluorophores in a densely labeled structure can be localized with diffraction-unlimited precision.

In super-resolution widefield tracking, like FIONA or single-particle tracking photoactivated localization microscopy (sptPALM), the movement of individual fluorescent particles is followed. By collecting enough photons, the spatial resolution can be enhanced according to equation (eq. 3), but at an unchanged photon rate, this inevitably worsens the time resolution of the method. A FIONA tracking experiment of kinesin labeled with the organic fluorophore Cy3 reported a low single-digit nanometer spatial resolution with ~4000 photons collected every 330 ms[16].

I.7 MINFLUX nanoscopy

Another leap in the field of diffraction-unlimited fluorescence microscopy was achieved by the invention of the Minimal photon Fluxes (MINFLUX) concept, which pushed the resolution down to molecular dimensions. It introduced the paradigm shift to not localize a molecule with the maximum, but rather the minimum of an excitation pattern (as illustrated in Fig. I5). The microscope presented in the initial publication featured an excitation doughnut with a minimum in the center surrounded by the steep slopes of the beam profile. During a MINFLUX measurement, the approximate position of a fluorophore is gathered from a confocal measurement and subsequently, the minimum of the MINFLUX excitation doughnut is positioned at the determined approximate position. Next, the fluorescent signal is recorded for different positions of the minimum near the fluorophore (of which one usually is the assumed fluorophore position). The precise position of the emitter can be determined with the rule that the closer the minimum is to the true position of the fluorophore, the lower the resulting emission should be. The signal, which is assumed to be proportional to the laser intensity the fluorophore experiences, can be fitted with a quadratic approximation of the intensity pattern near the minimum. As the approximate position is injected by the well-defined excitation pattern, the photons emitted by the fluorophore can be used efficiently for the fine-tuning of the position estimate, making MINFLUX extremely photon-efficient. The localization precision can be further enhanced by zooming in and decreasing the distances $L/2$ of the surveyed positions from the assumed fluorophore position whilst increasing the intensity and hence the slope of the excitation pattern.

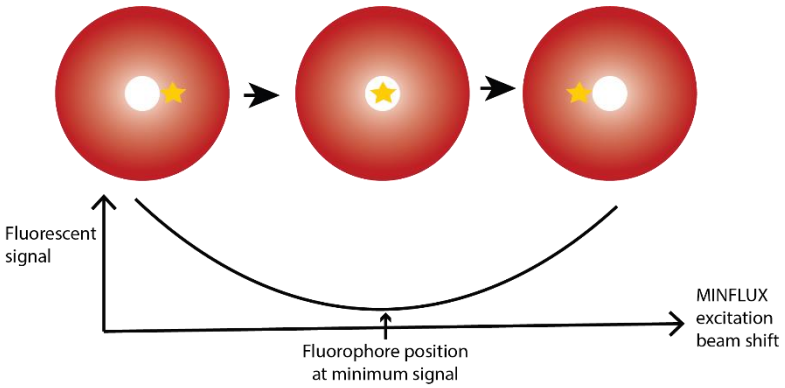

Figure I5: Concept of MINFLUX. A fluorophore (yellow) is scanned with the minimum of a (doughnut-shaped) excitation beam (red). The closer the minimum to the fluorophore position, the lower the fluorescent signal.

I.7.1 Tracking

The doughnut-shaped MINFLUX setup achieved a spatial precision of <2.5 nm, requiring only ~100 detected photons. Due to this photon efficiency, the temporal resolution of MINFLUX tracking was reported to be 100-fold enhanced compared to camera-based tracking techniques. The standard deviation of the localization precision achieved by MINFLUX is given by

$$\sigma_{minflux} \geq \frac{L}{4\sqrt{N}} \qquad \text{(eq. 4)}$$

which indicates that the resolution increases with more photons, but more efficiently by decreasing the interval size L. Decreasing L reduces the signal-to-background ratio (SBR) of the measurement, so increasing the resolution indefinitely by decreasing L is prevented by the background of the experiment. As N is the product of temporal resolution (τ) and the detected photon rate (Φ), the following equation can be derived, which indicates the trade-off between spatial resolution (σ) and temporal resolution (τ) in an ideal MINFLUX measurement

$$\sigma_{minflux} * \sqrt{\tau} \geq \frac{L}{4\sqrt{\Phi}}. \qquad \text{(eq. 5)}$$

Decreasing sigma by a factor of 2 requires increasing τ by a factor of 4, decreasing L by a factor of 2 or increasing Φ by a factor of 4.

MINFLUX tracking in living E. coli bacteria yielded a spatial precision of <50 nm within ~125 µs using <10 detected photons[20]. Tracking of single labeled lipids in an artificial lipid-bilayer membrane achieved a localization precision of <20 nm within ~100 µs[21]. For a non-biological DNA origami swinger, a spatial precision of 1.7 nm was achieved with 1 ms temporal resolution[22].

I.7.2 Imaging

For MINFLUX imaging of densely labeled structures, the fluorophores need to be switched between their on- and off-states, so that a single emitter can be precisely localized at a given time. This is

achieved by using blinking or photoactivatable/caged fluorophores. For photoactivatable/caged fluorophores, (high-energy-) irradiation causes an intramolecular reaction or removes caging groups, both of which turn the fluorophore on. After successful localization of a subset of fluorophores, they turn off or are bleached before the next subset is activated and localized. The final image is constructed from all successful localizations. With MINFLUX, blinking fluorophores (Alexa Fluor 647) spaced by down to ~6 nm on a DNA origami were localized with a precision of ~1 nm using ≥1000 detected photons[20]. MINFLUX imaging is also possible in fixed and living cells, as has been demonstrated by the successful revelation of the eightfold symmetry of protein Nup96 in nuclear pore complexes with a spatial precision of ≤2 nm[23].

I.7.3 Fluorescent background

The main strengths of MINFLUX are its photon-efficiency yielding a superior spatio-temporal resolution and it requiring only a small fluorescent label, which allows live-cell tracking and imaging experiments. However, as previously mentioned, its attainable resolution is limited by the fluorescent background of the sample. Therefore, high-performance measurements require rigorous minimization of the sample's fluorescent background and optimization of the minimum of the excitation pattern. It is hence of great value to develop an assay that mimics the biological function of the molecule or structure of interest, whilst displaying a strongly reduced fluorescent background compared to a (living) cell. Furthermore, employing other excitation patterns with steeper slopes surrounding the lower minimum would be highly advantageous. With this, studying fast biological processes of relevant targets with MINFLUX is a promising ambition.

I.8 MINSTED nanoscopy

A novel fluorescence-based nanoscopy method, which is much less sensitive to fluorescent background, is called MINSTED. It uses co-aligned excitation and STED beams to create an effective Gaussian-shaped excitation beam whose FWHM can be decreased with increasing power of the STED beam according to equation (eq. 2), which also increases the slope of the excitation beam's flank. By approaching a single fluorophore with the narrow beam, the fluorophore only experiences a small intensity until the doughnut minimum is very close, where the fluorescence response rises sharply (as illustrated in Fig. I6). Circling around whilst coming closer to the emitter allows for its precise localization with the highly informative steep excitation slope. With every detected photon i, the circle radius R_i is decreased to half the FWHM of the effective excitation beam, which ensures the fluorophore to only experience moderate intensities of the depletion laser. The center position of the circle is moved in the direction of the detected photon by a fraction of R_i, which makes the center of the circle coincide with the fluorophore position. With MINSTED, sub-nanometer localization precisions are possible with <1000 detected photons. Fluorophores consecutively attaching to a DNA origami via DNA points accumulation for imaging in nanoscale topography (PAINT) were localized with a median spatial

precision of 4.7 Å with only 2000 detected fluorescence photons[24]. As the STED beam suppresses fluorescent background, the technique is less impaired by it, making MINSTED suitable for imaging and tracking in environments with intrinsically high background.

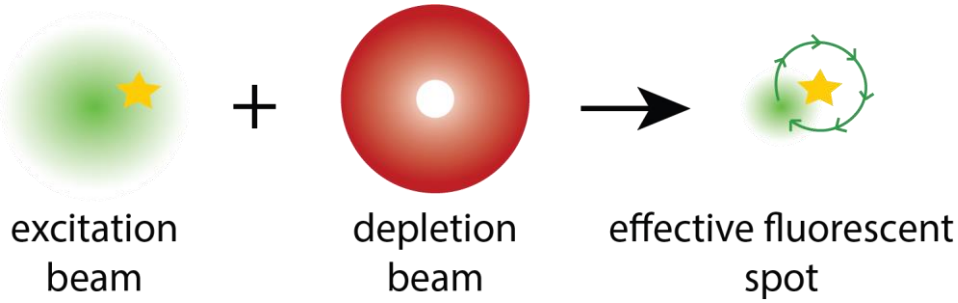

Figure I6: Concept of MINSTED. The FWHM of an excitation beam is narrowed with a depletion beam. The narrow effective fluorescent beam is circled around the fluorophore (yellow) and moved closer for each fluorescent photon triggered by the flank of the excitation beam. After a successful measurement, the circle center coincides with the fluorophore position.

MINSTED tracking has so far not been evaluated and reported, but due to its spatial precision and robustness against background, establishing it as a tracking technique should prove to be highly beneficial for the field.

Chapter 1: Polymer-based *in vitro* assays with decreased fluorescence background

Aim

The following chapter aims to compare different immobilization methods for single molecule studies and to identify the most suitable one for MINFLUX investigations. The ideal method immobilizes the target specifically and restricts its diffusional movement while reducing sample background from target molecules or contaminants attaching non-specifically to the sample surface. Optimally, it is easy to construct, reproducible and stable over extended periods. In biological studies, the immobilizations of for instance proteins must also not alter their function due to unnatural interactions with their nano-environment.

Overview

The simplest immobilization techniques are spin-coating or dip-coating, during which the substrate (i.e. the coverslip) is covered with a solution containing the target. After evaporation of the solvent, the non-volatile target sticks directly and non-specifically to the surface by electrostatic interactions. These interactions arguably alter the function of proteins[25-28], and as immobilization forces are weak and non-specific, immersion in an aqueous buffer would detach them from the surface, making biologically relevant *in vitro* measurements impossible.

Aminosilanes like (3-Aminopropyl)triethoxysilane (APTES) are commonly used to covalently bind amino-reactive targets. The activated glass surface is silanized with APTES in a condensation reaction, after which the surface is modified with primary amines. Amino-reactive functional groups, like aldehydes, can be reacted with the amines, leading to a stable covalent bond that immobilizes the target molecule to the surface. However, as APTES renders the surface hydrophobic[29], immobilized proteins are likely to exhibit altered behavior when linked to the silanized coverslip.

Another established method makes use of the biotinylated protein bovine serum albumin (BSA-bt) attaching to the glass surface via electrostatic interactions. Biotin-binding proteins like streptavidin, neutravidin or avidin are immobilized to the biotins of the surface-covering BSA-bt via one of the strongest non-covalent biological bonds with a dissociation constant of ~$4x10^{-14}$ M[30]. As the biotin-binding proteins have four binding sites, other biotinylated fluorophores, DNA constructs or proteins can be attached in a following step.

The arguably most biologically relevant systems for the study of proteins are in cellulo or even live-cell. Here, the targets are in their natural environment, so measurement artefacts should in principle be minimal, but measurements in cells with fluorescence microscopy have major drawbacks compared to

those of the previously mentioned *in vitro* assays. Growing and preparing cells is very time-consuming and involved. For live-cell measurements, cells usually need to be transfected with the plasmid of the target mutated to carry a fluorescent protein or labeling tag. The choice of probes is hence restricted to live-cell-compatible fluorescent dyes and the intrinsic dynamics in a living cell, for instance the movement of cellular structures, may lead to artefacts in longer measurements. To circumvent these issues, cells can be fixed and the cell membrane permeabilized. This lifts the restriction for usable constructs and dyes, but proteins of cellular structures need to be stabilized by covalent cross-linking, which changes their local nano-environment and potentially also their function.

Results and Discussion

1.1 BSA-bt assay

The initial assay of choice for screening fluorophores and developing a molecular motor system for MINFLUX tracking was the previously mentioned BSA-bt *in vitro* assay. It offers more versatility compared to cell-based assays and retains a much more natural nanoenvironment compared to the APTES assay. It has been extensively used in previous single molecule studies with, amongst others, MINFLUX microscopy. Hence, I performed tests, how well it specifically immobilizes the target while blocking the surface to reduce fluorescent background by minimizing unspecific binding.

For all measurements, I used coverslips rinsed with isopropanol and cleaned in an oxygen plasma, as it had been previously shown that plasma treatment effectively removes potential fluorescent contaminants[31]. Furthermore, oxygen plasma increases wettability of the surface by making it more hydrophilic. I built a flow chamber by attaching the coverslip to an objective slide via two parallel double-sided adhesive strips. Between steps, the flow chamber was washed thoroughly with buffer.

First, I created the complete assay by flowing in BSA-bt, then neutravidin (NVD) and finally 100 fM of the biotinylated fluorophore ATTO 647N (ATTO 647N-bt) (as illustrated in Fig. 1.1). After a last washing step, I imaged the sample and observed single molecule coverage with the fluorophore (Fig. 1.2a). But a control sample, where I used unbiotinylated bovine serum albumin (BSA) instead of BSA-bt, also immobilized many fluorophores (Fig. 1.2b), indicating that neutravidin and/or the fluorophore immobilize unspecifically to the surface coated with BSA. However, as the coverage was less, some specific immobilization via the biotin-neutravidin bond seems to occur. In another control, where I added ATTO 647N-bt directly to the BSA-bt-coated surface, no immobilized fluorophores were observed (Fig. 1.2c), showing that the fluorophores in the previous control bound to neutravidin unspecifically attached to BSA or the glass. Hence, the BSA-bt assay apparently does not efficiently prevent unspecific immobilization of proteins to the surface and I deemed it to not reduce fluorescent background effectively resulting from the unspecific immobilization of fluorescently labeled proteins.

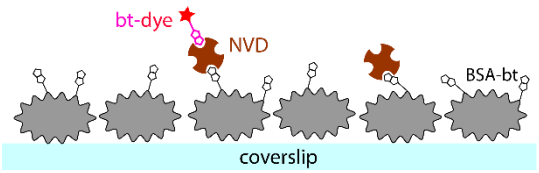

Figure 1.1: Illustration of the BSA-bt assay for immobilization of biotinylated fluorophores via neutravidin.

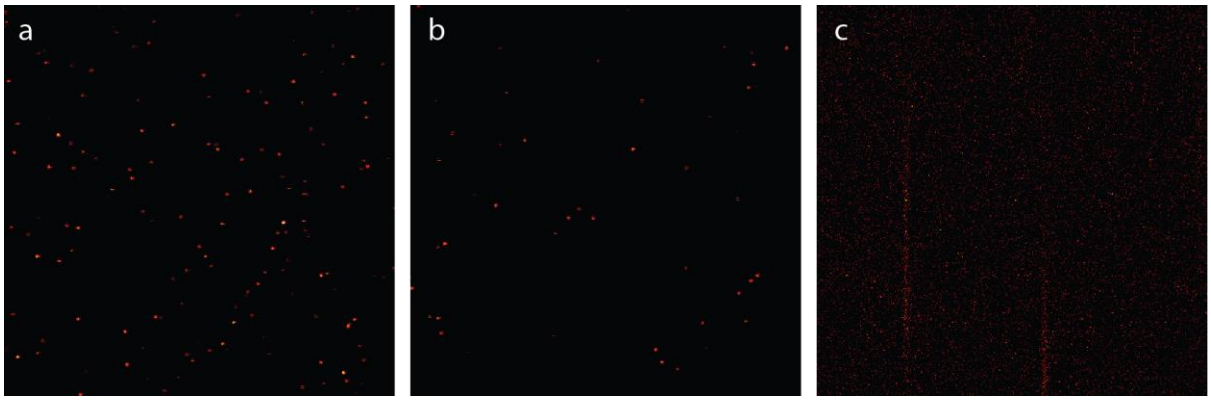

Figure 1.2: Confocal images of the BSA-bt assay for immobilization of biotinylated fluorophores. (**a**) The complete assay gave single molecule coverage. (**b**) The control assay with unbiotinylated BSA instead of BSA-bt gave an only slightly reduced coverage. (**c**) The control assay with neutravidin (NVD) omitted immobilized no biotinylated fluorophores. Size: a/b/c: 50 µm*50 µm; Scalebar min/max: a/b: 0/50, c: 0/5.

1.2 PLL-bt assay

These results motivated finding and applying of a better assay for single molecule studies with MINFLUX. I identified the grafted polymer Poly(L-lysine)-g-Poly(ethylene glycol)-biotin (PLL-bt) as a promising candidate. It consists of a Poly-L-lysine (PLL) back chain that, due to its positive charges at physiological pH, is known to have a strong affinity to attach to and cover the glass surface[32]. The grafted hydrophilic Polyethylene glycol (PEG) chains are assumed to form dense, brush-like structures into the sample that have a great surface-passivating function as they allow water to enter. A fraction of brushes carries terminal biotin functions, allowing streptavidin/neutravidin/avidin to bind.

For the complete assay (illustrated in Fig. 1.3), I coated a coverslip with PLL-bt by immersing it in an aqueous solution of the polymer with 1% (v/v) of Tween-20 (T20) added, a non-ionic surfactant for filling the gaps not covered by the polymer. I then added neutravidin and finally 100 pM of ATTO 647N-bt, which resulted in a single molecule coverage of the fluorophore (Fig. 1.4).

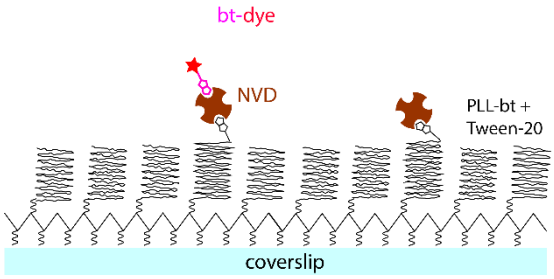

Figure 1.3: Illustration of the envisioned PLL-bt assay for immobilization of biotinylated fluorophores via neutravidin (NVD).

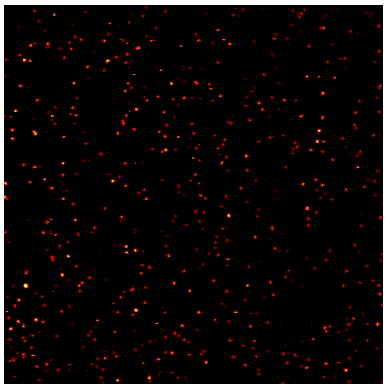

Figure 1.4: Confocal image of the complete PLL-bt assay for immobilization of biotinylated fluorophores. The complete assay gave single molecule coverage. Size: 50 µm*50 µm; Scalebar min/max: 0/50.

In a first control, I added PLL-bt/T20, neutravidin and an excess of biotin (1 mg/ml) to block the binding sites of neutravidin. This significantly reduced the coverage of ATTO 647N-bt added afterwards (Fig. 1.5). The remaining fluorescent spots might be caused either by unspecific binding or by ATTO 647N-bt specifically binding to neutravidin not fully occupied with biotin. The reduced immobilization in the control shows that most fluorophores bind specifically via the biotin-neutravidin bond in the complete assay. Furthermore, fluorescent signal of the background is very low (see Fig. A1.1).

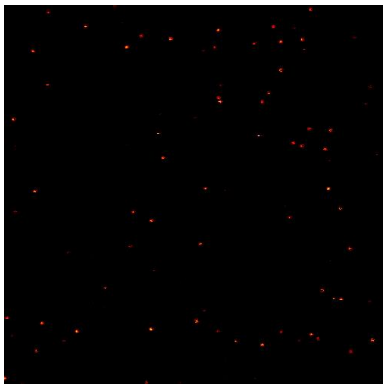

Figure 1.5: Confocal image of a control of the PLL-bt assay for immobilization of biotinylated fluorophores. Addition of biotin before the incubation of ATTO 647N-bt gave a reduced, but still significant coverage compared to the complete assay. Size: 50 µm*50 µm; Scalebar min/max: 0/50.

After having certified the enhanced fluorescent background reduction through PLL-bt, an assay for testing fluorophore behavior on a nanobody or antibody was envisioned (as illustrated in Fig. 1.6). For the assay, I coated a coverslip with PLL-bt/T20 and added neutravidin. Next, I added biotinylated primary antibody (bt-AB) to specifically bind to the binding sites in neutravidin. A secondary antibody or nanobody covalently labeled with the fluorophore of interest could then specifically attach to bt-AB. With this assay, the performance of fluorophores on antibodies, to be used for fixed cell labeling, can be evaluated *in vitro*.

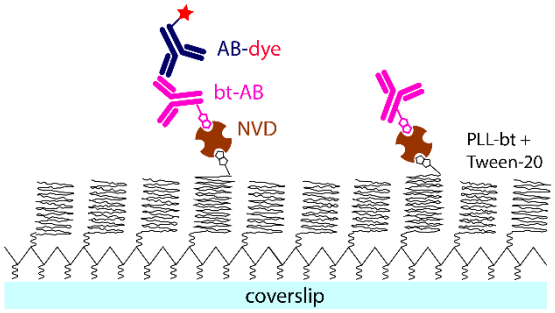

Figure 1.6: Illustration of envisioned PLL-bt assay for immobilization of fluorescently labeled antibodies/nanobodies via neutravidin (NVD) and biotinylated primary antibody (bt-AB).

I created and tested the envisioned assay, which gave single molecule coverage with ~1 nM of an antibody (AB) or nanobody (NB) labeled with Alexa Fluor 647 (Fig. 1.7a and Fig. 1.7b). I performed several controls to evaluate the specific immobilization of all components. Representative images of the samples (Fig. A1.2), where neutravidin, bt-AB or both had been omitted, showed mainly background noise and only few fluorophores of unspecifically immobilized labeled antibodies (AB-AF647) or nanobodies (NB-AF647) were observed on large fields of view (50 µm*50 µm). For another control, where I added PLL-bt/T20, neutravidin and subsequently biotin for blocking of the binding sites of neutravidin, ensuing addition of bt-AB and NB-AF647 showed nearly no fluorescent spots (Fig. A1.3a), indicating that bt-AB binds specifically to neutravidin and the nanobody binds exclusively to bt-AB. By omitting T20 in this control, some NB-AF647 immobilized unspecifically (Fig. A1.3b), indicating how effectively T20 blocks the surface where PLL-bt did not attach.

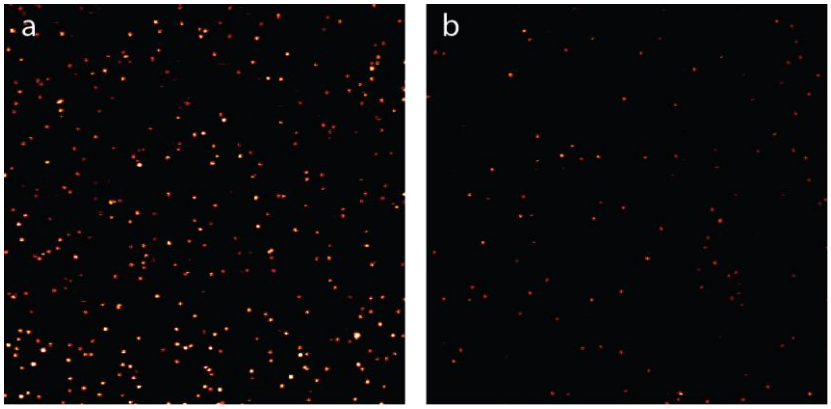

Figure 1.7: Confocal images of the complete PLL-bt assay for immobilization of fluorescently labeled (**a**) antibodies (AB-AF647) or (**b**) nanobodies (NB-AF647) via neutravidin (NVD) and biotinylated primary antibody (bt-AB). The complete assays gave single molecule coverage. Size: a/b: 50 µm*50 µm; Scalebar min/max: a/b: 0/50.

In a separate experiment, I tested the specific binding of the fluorescently labeled secondary antibody/nanobody in cells. For this, I fixed U2OS cells with methanol and incubated them with a primary antibody against tubulin. With the use of a primary mouse antibody and direct addition of a fluorescently labeled anti-mouse nanobody (NB-AF647), the microtubule structure of the cells was clearly resolved (Fig. A1.4a). In a control, where I used a primary rabbit antibody instead, subsequent addition of anti-mouse NB-AF647 did not reveal the structure of the microtubule network, but only comparably dim signal from unspecifically bound NB-AF647 or autofluorescence of the cell (Fig. A1.4b). This indicates that the anti-mouse NB-AF647 in the first experiment specifically bound to the mouse primary antibody. In the main test for the functioning of bt-AB, I incubated the fixed cells first with the primary rabbit antibody against tubulin and subsequently with the biotinylated mouse anti-rabbit antibody (bt-AB) used in the PLL-bt-antibody/nanobody assay. Addition of NB-AF647 revealed the microtubule structure (Fig. A1.4c), showing that bt-AB specifically bound to the rabbit primary antibody on the microtubules and that anti-mouse NB-AF647 specifically bound to the mouse bt-AB. Comparison with the negative control lacking the bt-AB (Fig. A1.4b) clearly shows that despite biotinylation, the antibody was still recognized by antibodies.

For direct comparison, I also created an antibody/nanobody immobilization assay based on BSA-bt (as illustrated in Fig. A1.5). For the complete assay, I coated a coverslip with BSA-bt, neutravidin, bt-AB and finally NB-AF647, which gave a strong single molecule coverage (Fig. 1.8a). For the controls, I omitted neutravidin (Fig. 1.8b) or bt-AB (Fig. 1.8c), which both showed a similar coverage of the labeled nanobody as the complete assay. This clearly confirms that the BSA-bt assay does not effectively prevent unspecific immobilization of proteins.

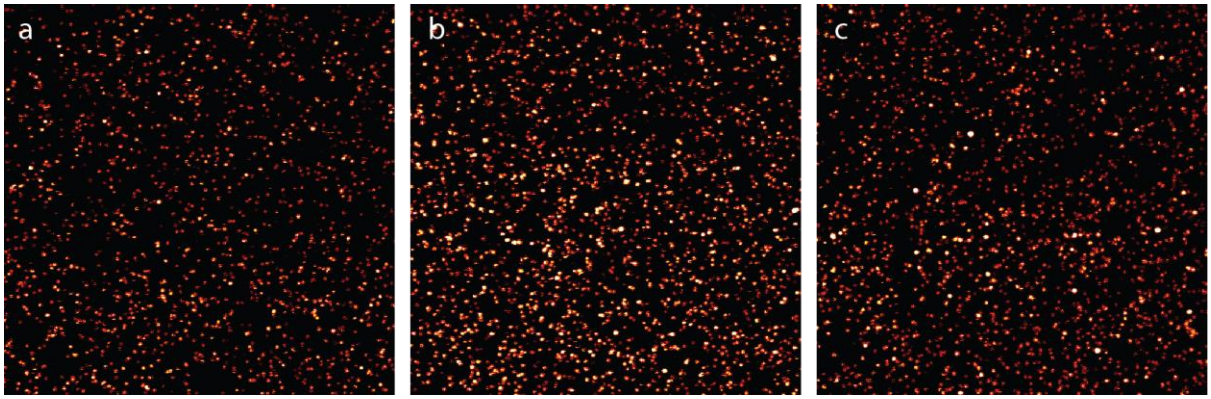

Figure 1.8: Confocal images of (**a**) the complete BSA-bt assay for immobilization of fluorescently labeled nanobodies (NB-AF647) via neutravidin (NVD) and biotinylated primary antibody (bt-AB), (**b**) the control with NVD omitted and (**c**) the control with bt-AB omitted. All assays gave strong single molecule coverage. Size: a/b/c: 50 µm*50 µm; Scalebar min/max: a/b/c: 0/50.

It therefore becomes apparent, that the PLL-bt assay specifically immobilizes antibodies/nanobodies, even if they are fluorescently labeled and reduces fluorescent background from unspecific immobilization more drastically than the BSA-bt assay, making it a superior assay for *in vitro* MINFLUX studies.

1.3 PLL-NTA assay

Additionally, I established a versatile assay for immobilizing recombinant proteins that carry a his-tag (as illustrated in Fig. 1.9). It employs the polymer Poly(L-lysine)-g-Poly(ethylene glycol)-nitrilotriacetic acid (PLL-NTA) that has a Poly-L-lysine back chain and grafted PEG chains, of which >90 % carry a terminal nitrilotriacetic acid (NTA) function[33]. As a representative protein, I chose the commonly used HaloTag expressed with an N-terminal his_6-tag (his_6-HT7), as it is heavily used in (living) cell experiments and can be labeled with synthetic fluorophores. The assay consists of PLL-NTA/T20 on the coverslip, Ni^{2+} (from $NiCl_2$) loading the NTA groups and his_6-HT7 binding to an NTA group via its his-tag. A chloroalkane-functionalized fluorophore is assumed to covalently bind to the binding pocket of the HaloTag protein in a nucleophilic attack reaction.

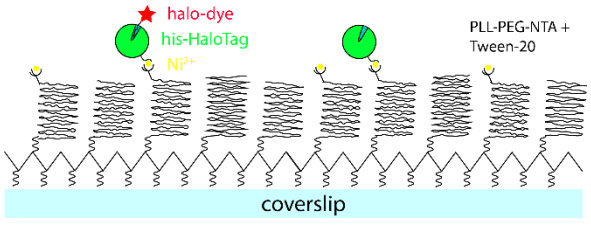

Figure 1.9: Illustration of the envisioned PLL-NTA assay for immobilization of chloroalkane-functionalized fluorophore (halo-fluorophore) via his-tagged HaloTag (his-HT) and Ni^{2+}.

For the complete assay, I achieved a high single-molecule coverage using ~1 nM of the chloroalkane-functionalized fluorophore silicon-rhodamine (halo-SiR) (Fig. 1.10a). To test, whether immobilization was specific, I incubated the sample for 10 minutes in EDTA (100 mg/ml), which

removed nearly all fluorescent spots (Fig. 1.10b). As EDTA is known to remove Ni^{2+} from the complex of NTA and his-tag, this is a clear sign that his_6-HT7 bound specifically to PLL-NTA via its his-tag. In a similar test, I added imidazole (100 mM), known to outcompete his-tags for binding to NTA-Ni^{2+} complexes, to a complete assay, which also removed most fluorescent spots (Fig. A1.6). This again indicates that the fluorophore had been immobilized specifically.

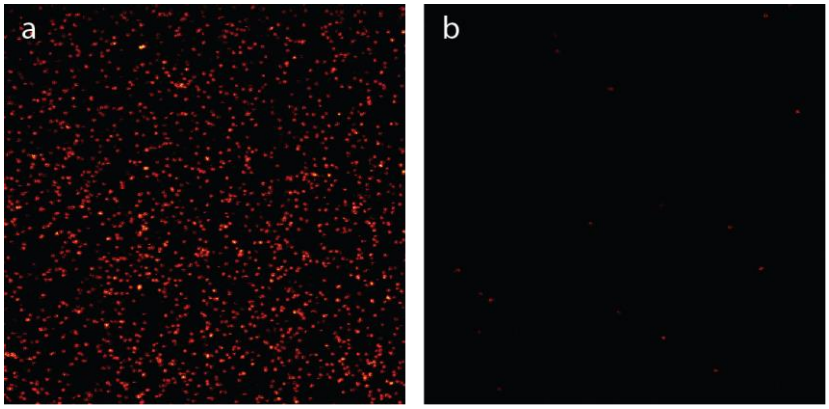

Fig. 1.10: Confocal images of (**a**) the complete PLL-NTA assay for immobilization of chloroalkane-functionalized fluorophore (halo-fluorophore) via his-tagged HaloTag (his-HT) and Ni^{2+} and (**b**) the assay after incubation with EDTA (100 mg/ml). EDTA incubation drastically reduced fluorophore coverage. Size: a/b: 50 µm*50 µm; Scalebar min/max: a/b: 0/50.

Next, I tested the affinity of halo-SiR to attach unspecifically to the glass surface or the PLL-NTA/T20 layer, respectively. Adding halo-SiR to a bare coverslip and a coverslip coated with PLL-NTA/T20, both previously incubated with $NiCl_2$, did not cause any observably immobilization of the fluorophore (Fig. A1.7) in any sample, another indication that binding in the complete assay was not unspecific.

I also established the assay for immobilization of the self-labeling protein tag SNAP-tag, which can covalently bind fluorophores functionalized with benzylguanine (BG). For this, I coated the coverslip with a PLL-NTA/T20 layer, added $NiCl_2$ and subsequently immersed the sample with recombinantly expressed his_6-SNAP-tag. Labeling with ~1 nM of the benzylguanine-functionalized fluorophore silicon-rhodamine (BG-SiR) gave a strong single molecule coverage (Fig. A1.8a). Addition of 100 mM imidazole removed most fluorescent spots (Fig. A1.8b), a clear indication that his_6-SNAP-tag had been immobilized specifically to the NTA groups via its his-tag. In a control experiment, where his_6-SNAP-tag was omitted from the complete assay, BG-SiR did not strongly immobilize (Fig. A1.8c), ruling out strong unspecific binding of the fluorophore.

With these experiments, I concluded that recombinant proteins can be immobilized via their his-tag binding to PLL-NTA loaded with Ni^{2+}. The controls show that immobilization is specific and that PLL-NTA/T20 strongly minimizes fluorescent background from unspecific binding. By immobilizing his-HT7, one can immobilize chloroalkane-functionalized fluorophores and study them when covalently bound to the HaloTag binding pocket. Beyond the immobilization of self-labeling protein tags, the assay should be extendable to all sorts of his-tagged proteins.

Conclusion

In this chapter, I investigated methods for immobilizing fluorophores for *in vitro* experiments. I demonstrated that the commonly used BSA-bt based assay, which was also the assay of choice for *in vitro* MINFLUX and MINSTED experiments, immobilized the target, i.e. the fluorophore, (partially) specifically, but significant fluorescent background resulted from the assay not completely blocking the glass surface from unspecific binding of the fluorophore. PLL-bt/T20 minimized unspecific binding and immobilized fluorescently labeled antibodies/nanobodies specifically. With this assay, fluorescence background, detrimental in MINFLUX measurements, is minimized, which in this aspect makes the assay superior to the BSA-bt assay. For more versatility, I also developed an assay with PLL-NTA/T20 that successfully immobilized his-tagged proteins and minimized fluorescent background.

Chapter 2: Spontaneously blinking fluorophores for live-cell MINFLUX imaging

Aim

This chapter describes the study of novel spontaneously blinking fluorophores with the aforementioned PLL-bt and PLL-NTA *in vitro* assays. Imaging samples on the nanometer scale with MINFLUX requires a fluorescent label that can be switched between a non-emissive off-state and a fluorescent on-state. I employed live-cell-compatible fluorophores that spontaneously switch between these states and investigated their blinking behavior when bound to an antibody or a HaloTag, respectively, laying the foundation for identifying the ideal fluorophore for MINFLUX imaging of biological structures in living cells.

Overview

Revealing the structure of organelles on the nanoscale requires a dense labeling of usually structural proteins. But the precise determination of the position of multiple emissive fluorophores within a diffraction-limited spot is prevented according to the Abbe limit. One way to reduce the number of emissive fluorophores after excitation is stimulated depletion, as it is used in the deterministic STED microscopy, where fluorophores in the periphery of the excitation spot are brought back to their non-emissive ('dark') ground state by the red-shifted depletion laser. In stochastic STORM microscopy, blinking fluorophores are employed that have a low duty cycle by mainly being in their dark state and only sometimes switching to their emissive state. The most common way to induce blinking is the use of cyanine fluorophores in a blinking buffer. A popular example is the combination of the cyanines Cy5 or Alexa Fluor 647 (AF647) and a primary thiol (R-SH) as a reducing agent. The deprotonated thiol can form an encounter complex with the fluorophore and reversibly bind to the fluorophore in a light-driven reaction, breaking the conjugated π-electron system and hence forming a non-fluorescent adduct (see Fig. 2.1)[34]. This dark state is long-lived but irradiation with low-wavelength light can reverse the reaction, giving a short-lived emitting fluorophore. With the low duty cycle due to the blinking buffer, only a small subset of fluorophores is in their bright state at a given time, allowing the precise localization of labeled fluorophores in a densely labeled sample.

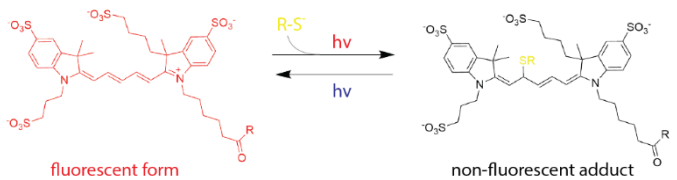

Figure 2.1: Reversible light-induced reaction of the cyanine Alexa Fluor 647 with a deprotonated primary thiol ($R\text{-}S^-$) to give a non-fluorescent adduct. The reaction can be reversed and fluorescence regained by irradiation with low-wavelength light.

As the reaction of cyanines with thiols is light-driven, bringing most fluorophores into their non-fluorescent adduct state in the beginning of the measurement requires illumination with a high excitation power, which has potentially phototoxic effects and bears the risk of bleaching a significant fraction of the fluorophores, consequently leading to artefacts in the evaluation of structures on the nanometer scale. Furthermore, for good blinking conditions, the additive concentration (e.g. of thiols) must be adjusted, which is not easily done in live-cell experiments.

For these reasons, spontaneously blinking rhodamine-based fluorophores have been developed previously[35]. They carry a nucleophile function that can attack the fluorescent core in an intramolecular spirocyclization reaction, rendering the fluorophore non-emissive (see Fig. 2.2). This reversible reaction is pH-dependent and the rhodamine-based fluorophores have been tuned to be mostly in their spirocyclic ('dark') form in thermal equilibrium and in physiological and basic pH conditions, making the blinking fluorophores suitable for live-cell STORM microscopy. Their advantages of not requiring additives and irradiation with large laser power in the beginning of the measurement were argued to potentially be beneficial to the field of live-cell imaging with MINFLUX.

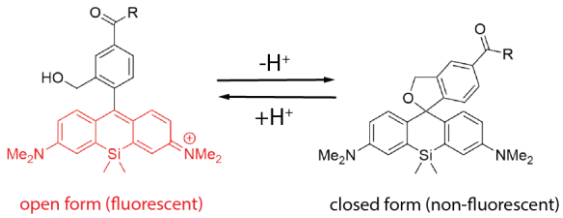

Figure 2.2: Illustration of the intramolecular spirocyclization reaction of spontaneously blinking rhodamine-based fluorophores.

Fluorophores suitable for MINFLUX imaging have to fulfil several criteria. They must have a very high on-off contrast ratio, the ratio between their brightness in the on and the off-state, as the technique is rather sensitive to background fluorescence due to it probing the fluorophore position within its excitation minimum. As the intramolecular nucleophilic attack breaks the conjugated π-electron system, fluorescence should go down drastically after the spirocyclization. Alternative fluorophores with a high on-off contrast ratio are caged fluorophores, which can be converted into their emissive form by an activation laser that cleaves of caging groups, but the latter can potentially be toxic and hence alter live-cell conditions. As MINFLUX requires much fewer photons for the same localization precision than STORM, suitable fluorophores for MINFLUX can have significantly shorter on-times of few milliseconds, which would make measurements much faster.

Therefore, novel spontaneously blinking fluorophores were identified as potentially superior for live-cell MINFLUX imaging, as they do not need to first be brought into their dark state by irradiation with high laser power, do not release caging groups upon activation and have a tunable on-state duration.

Results and Discussion

2.1 Novel spontaneous blinkers

First, a library of potential spontaneous blinkers, all built upon a silicon-rhodamine (SiR) fluorescent core with a thiophene- or benzothiophene-fused spirolactam fragment (Ar_1), was synthesized (see Fig. 2.3).

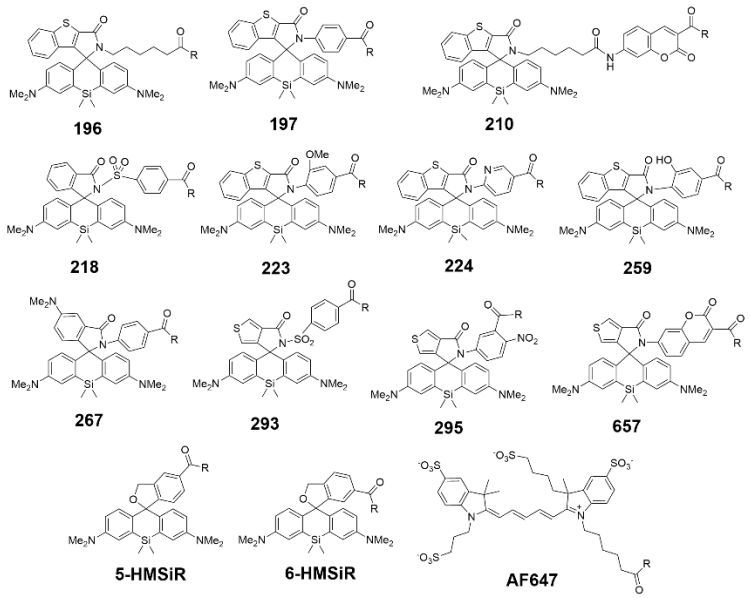

Figure 2.3: Library of potential spontaneous blinkers. The previously published spontaneous blinkers 5-HMSiR and 6-HMSiR and Alexa Fluor 647 were synthesized and used as references. R is the position of linker and functional group for labeling.

Via a nucleophilic attack of the nitrogen atom in the amide on the fluorescent core, the non-emissive spirolactam is formed, breaking the conjugated π–electron system (Fig. 2.4). For tuning of the switching properties, the fluorophores usually had aromatic residues (Ar_2), with different electrondonating or -withdrawing properties, which was also attached via a linker to the functional group for labeling.

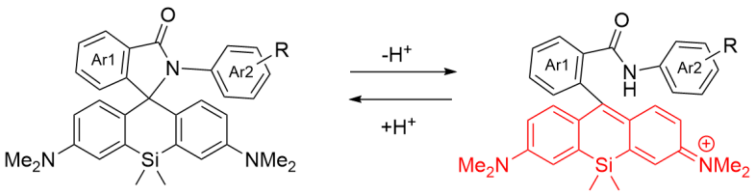

Figure 2.4: Illustration of the intramolecular spirocyclization reaction of novel spontaneously blinking silicon-rhodamine-based fluorophores with a thiophene- or benzothiophene-fused spirolactam fragment (Ar_1) and an Ar_2 fragment connecting to the functionalized group.

2.2 Performance in live and fixed cells

To identify the fluorophores that spontaneously blink in a cellular environment, I labeled fixed and live cells with them. For imaging fixed cells, I labeled polyclonal antibodies (goat, anti-rabbit IgG (H+L))

by adding a stoichiometric amount of fluorophore functionalized with an amino-reactive N-hydroxysuccinimide (NHS) ester (NHS or Sulfo-NHS) and subsequently removing unreacted fluorophores using size-exclusion chromatography to give the labeled antibody (ar-fluorophore). Due to the spirolactam formation rendering the fluorophores non-fluorescent, directly determining the degree of labeling (DOL) spectroscopically was not possible. However, labeling with Alexa Fluor 647-NHS and ATTO 647N-NHS, respectively, gave a low DOL of ~0.6 (for Alexa Fluor 647) and ~0.5 (ATTO 647N), as determined by UV-Vis spectroscopy. As Alexa Fluor 647 is a popular hydrophilic fluorophore, I estimated the DOL for the antibodies labeled with the potential spontaneous blinkers to be <0.6, which needs to be low to rule out a significant impact of interactions between fluorophores on the same antibody, which would change their photophysical properties.

I fixed human bone osteosarcoma epithelial (U2OS) cells with methanol to best retain the structure of microtubules and subsequently added a primary rabbit anti-tubulin antibody. I then added the fluorescently labeled low-DOL antibody and, after washing, mounted the sample in a mounting medium for immunofluorescence studies (Mowiol). For live cells, I added chloroalkane-functionalized fluorophores (halo-fluorophore) to U2OS cells stably expressing a fusion construct of vimentin and HaloTag protein (U2OS-Vim-Halo, created by CRISPR/Cas technology) and optimized specific labeling of the vimentin structure by varying fluorophore concentration and incubation time. I imaged the cells in a STORM microscope for more than 15 minutes and evaluated the data using ThunderSTORM (a plugin in ImageJ)[36]. More details on the labeling, staining and imaging protocols are provided in the methods section (appendix).

Out of all listed fluorophores, the cytoskeleton was only clearly revealed for 657, 197, 223, 224, 259, 295 and the previously published 5-HMSiR, as can be seen in Fig. 2.5 and Fig. A2.1. Further analysis of the super-resolution images of the fixed cells gave a lateral resolution of ~60-80 nm (full width at half maximum), which is an expected STORM resolution for the combination of the reported outer diameter of ~25 nm for microtubules and size of the primary-secondary antibody construct[37].

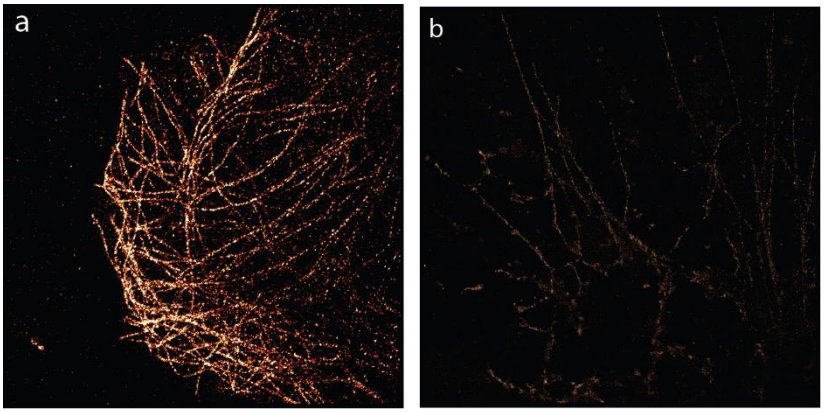

Figure 2.5: STORM images of (**a**) a U2OS cell fixed with MeOH and labeled with a primary antibody (rabbit, anti-tubulin) and ar-197 and (**b**) a living U2OS-vim-halo cell labeled with 100 nM halo-295. Imaging intensity (640 nm): 22 kW/cm^2; dwell time: 20 ms. Size: a/b: 25.6 µm*25.6 µm; Scalebar min/max: a: 0/255, b: 1/7.

2.3 In vitro assay mimicking the fluorophore's biological nanoenvironment

For establishing a method to screen fluorophores at single molecule conditions with a less complex environment compared to cells, I envisioned creating a robust *in vitro* assay, which immobilizes fluorophores in a way that does not significantly change their photophysical and blinking properties. I therefore tested the APTES and PLL-bt assays described in the previous chapter as to how they retain the switching characteristics of the different spontaneously blinking fluorophores observed in the cell experiments.

To coverlips silanized with APTES, I added the NHS-functionalized fluorophores and imaged the blinking of the single immobilized fluorophores in phosphate buffered saline (PBS, pH ~ 7.4) using a STORM microscope. No strong blinking was observed for most fluorophores studied and for 197 and 223 was significantly reduced compared to their blinking in cells. As the APTES assay did not faithfully reproduce the fluorophore blinking observed in cells, probably due to the fluorophore interactions with the surface and by it not being conjugated to a protein, I deemed it to not be suitable for further experiments.

For the PLL-bt assay, I coated an oxygen plasma-cleaned coverslip with PLL-bt/T20, neutravidin, a biotinylated rabbit antibody (bt-AB) and finally a secondary antibody conjugated with a spontaneously blinking fluorophore of interest used in the fixed cell experiments. Based on the results of the previous chapter, immobilization of the labeled antibody should be highly specific. On the PLL-bt assay, I imaged the spontaneous blinkers tested in the APTES assay. Mounted in PBS and measured on the STORM microscope with the same imaging conditions, the fluorophores which had given good STORM images in cell experiments also invariably displayed strong blinking in the PLL-bt assay. Non-blinking fluorophores in cell experiments also did not show significant spontaneous blinking in the *in vitro* assay. This clearly shows that the PLL-bt assay is much more suitable for the planned

investigations than the APTES assay and reveals, how crucial the choice of a suitable immobilization assay is.

To study the chloroalkane-functionalized fluorophores used in live cell experiments with U2OS-Vim-Halo, I used the PLL-NTA/T20 assay with his-tagged HaloTag7 protein to immobilize the fluorophore specifically in a nanoenviroment arguably similar to that of the self-labeling tag in U2OS-Vim-Halo.

Assuming that the assays mimic the fluorophore environment in cells and hence retain its properties, I analyzed STORM data of multiple promising spontaneous blinkers quantitatively in order to identify those suitable for MINFLUX imaging. Focus of the investigation was the duty cycle, which for the ideal MINFLUX fluorophore should be lower than for the ideal STORM fluorophore, as MINFLUX needs much fewer photons for the same spatial precision and is strongly slowed down if the fluorophores stay on after the precise localization has been achieved. Furthermore, the spontaneous blinker should not have a high number of blinking cycles (N_{cy}) within a short time, as a few precise localizations suffice per emitter.

2.4 Quantitative analysis of spontaneous blinking

For the quantitative analysis, I localized the fluorophores in the STORM image sequences using the ImageJ plugin ThunderSTORM. Blinking events within a distance of 300 nm were ascribed to a single fluorophore, which I justified by the sparse coverage. I also removed rare blinking events that were analyzed to come from more than one fluorophore, as determined by multiple emitter analysis, potentially from antibodies sometimes carrying multiple emitters. With a Matlab script, I created single molecule emission traces over time from the image sequences on the determined emitter positions. The traces exhibited spikes clearly distinguishable from the background signal (see Fig. A2.2, exemplary trace), indicating a high on-off contrast ratio necessary for good MINFLUX fluorophores.

By setting an appropriate threshold over which to count a spike as an on-event, I calculated the average times of an on-event (t_{on}) and the times between on-events (t_{off}). For the calculation of t_{off}, the off-time after the last on-event was omitted, as it's impossible to distinguish it from a bleached state, which could slightly underestimate the real off-time. I determined the duty cycle (DC) with the equation

$$DC = t_{on}/(t_{on} + t_{off}). \qquad \text{(eq. 6)}$$

The plotted *in vitro* data for the fluorophores on antibodies and bound to his-HaloTag, respectively, are shown in Fig. 2.6 (for the full data plots, see Fig. A2.3).

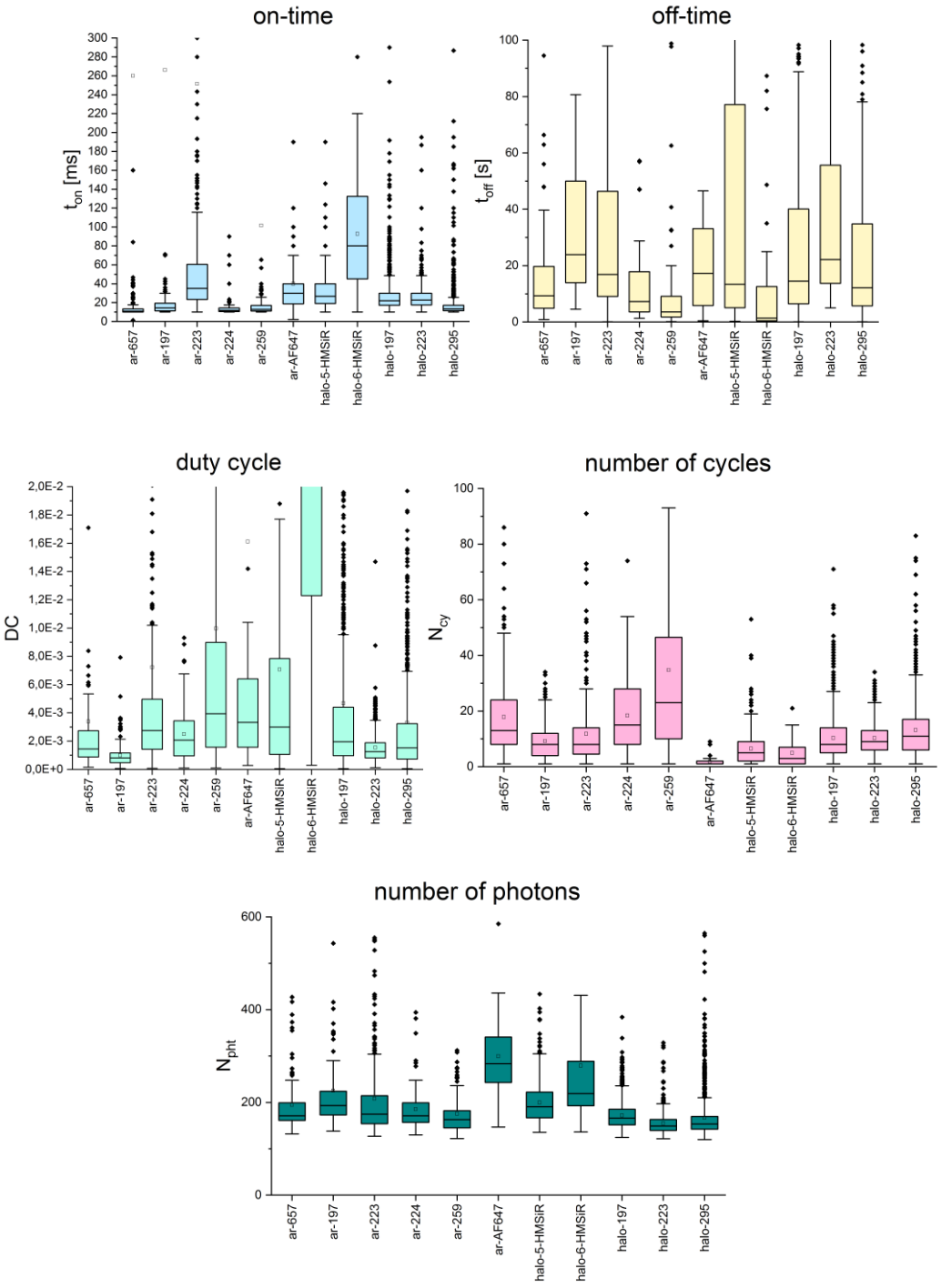

Figure 2.6: Box plots of on-times, off-times, duty cycle, number of cycles and number of photons per blinking event for the spontaneous blinkers attached to antibodies or HaloTag. The boxes represents the middle 50% of data and the horizontal line in the boxes is the median. The whiskers represent 1.5 times the interquartile range. Data points outside of the range are outliers and denoted with a ♦ symbol. The mean is denoted by the □ symbol.

As a reference, the thiol-induced blinking of Alexa Fluor 647 (AF647), a fluorophore heavily used in STORM and MINFLUX imaging, on antibodies (ar-AF647) immobilized by the PLL-bt assay in the presence of 1 M 2-mercaptoethylamine (MEA) and pyranose oxidase with catalase (POC) and glucose as oxygen scavenging system (OSS) are shown. The laser intensity in the sample plane was ~22 kW/cm^2

and the time resolution was 10 ms. For each spontaneous blinker, image sequences of 20000 frames were recorded and for AF647, image sequences of 5000 frames were recorded.

Table 2.1: Median values of on-times (t_{on}), off-times (t_{off}), duty cycle (DC), number of cycles (N_{cy}) and number of photons per blinking event (N_{pht}) for the spontaneous blinkers.

	t_on [ms]	t_off [s]	DC	N_cy	N_pht
ar-657	10.9	8.3	1.3E-03	13	171
ar-197	14.3	20.2	7.1E-04	8	193
ar-223	34.6	13.9	2.5E-03	8	175
ar-224	11.8	6.0	1.9E-03	15	171
ar-259	12.8	3.2	4.0E-03	23	163
ar-AF647	30.0	13.6	2.9E-03	1	288
halo-5-HMSiR	26.4	9.0	2.9E-03	5	191
halo-6-HMSiR	80.0	0.8	9.1E-02	3	219
halo-197	21.5	12.9	1.7E-03	7	167
halo-223	22.6	18.5	1.2E-03	9	149
halo-295	13.3	10.2	1.3E-03	11	153

The distribution of on-times and their averages show that most spontaneous blinkers have a lower on-time per on-event than AF647, even though a very high thiol concentration of 1 M MEA, compared to ~10 mM MEA in comparable experiments, was used, which should decrease the on-time of AF647 by sending it to its non-emissive form more strongly. Interestingly, their median on-times are mostly near the time resolution, with which the STORM image sequences were recorded (10 ms). As most blinking events were within a single measurement bin, it seems likely that the real on-times of the spontaneous blinkers is even lower and the evaluated times are only artificially enlarged by the limited time resolution of the camera. A more suitable method for determining the short on-times would be confocal measurements, where a time resolution of multiple microseconds is feasible. One further interesting finding is that the median on-time of the hydroxymethyl-modified silicon-rhodamine 6-HMSiR is more than three times higher than that of its regioisomer 5-HMSiR, despite the only difference between them being the position of the linker on the aryl carrying the hydroxymethyl. This might be a hint towards how strong electron-donating and -withdrawing effects or the orientation of the fluorophore in the HaloTag cavity might affect the blinking properties.

Although the median off-time of 6-HMSiR is lower than 1 s, but most spontaneous blinkers have median off-times of many seconds, giving them duty cycles of lower than 2.5×10^{-3}, which is smaller than the artificially lowered duty cycle determined for AF647 with 1 M MEA. The duty cycle of, for instance, 197 on the antibody (ar-197) is as low as 7.1×10^{-4}, and probably even smaller, as the real on-time is most likely lower than 10 ms, which suggests it to be a suitable fluorophore for MINFLUX imaging of densely labeled structures. All other spontaneous blinkers, apart from 6-HMSiR with its more than 30-times higher duty cycle compared to the other halo-fluorophores, seem to also be promising candidates due to their low duty cycle. They displayed multiple blinking events within the

measuring time. My impression of the traces was, that blinking occurrence was approximately similar throughout the whole measurement, indicating that the spontaneous blinkers were not very prone to bleaching, which would make long and repeated measurements of the same sample possible and the number of cycles could potentially allow the observation of slow structural rearrangements of a cell.

The number of detected photons per on-event did not differ strongly between spontaneous blinkers and were not much lower than for AF647, known to be a fluorophore with a very high fluorescence rate. This means that they have a competitive fluorescence rate, necessary for fast and efficient MINFLUX measurements. Estimations of ~10 kHz, calculated by dividing the median photon numbers by the median on-time, are most likely strong underestimates as the real on-times are probably significantly shorter.

An interesting feature of the *in vitro* assays is that the effect of the nanoenvironment, so the surface of the antibody or the cavity of the HaloTag, on the photophysical properties of the fluorophores can be investigated. For this, I compared the data of 197 and 223 (chemical structures in Fig. 2.7) when bound to the polyclonal antibody and the HaloTag, respectively. The only difference between these benzothiophene-functionalized SiR-based fluorophores is an additional methoxy-functionalization of the Ar_2 ring in 223.

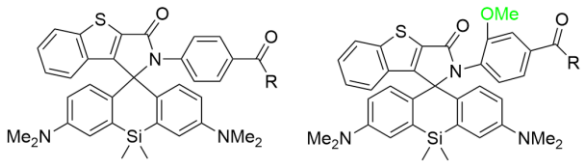

Figure 2.7: Chemical structures of the spontaneous blinkers 197 and 223.

For 197, the on-time was higher when bound to HaloTag and the distribution of duty cycles is much broader and with a higher median compared to the antibody-bound flurophore. Interestingly, the photon counts do not correlate with the on-time and are even slightly higher for the antibody-conjugation. The number of cycles seems rather unaffected by the conjugation.

For 223, which has a methoxy-group in the ortho-position that is known to have an electron-donating, positive mesomery effect (+M) and an electron-withdrawing, negative induction effect (-I), the trends are somewhat inversed. The antibody-conjugated spontaneous blinker has the second-longest on-time (after 6-HMSiR), but when bound to HaloTag, it is reduced by about a third and the photon counts are also decreased slightly. As the off-time is rather constant, the duty cycle is also significantly lower for the halo-fluorophore. The number of cycles remains also unaffected for 223.

To investigate, if the heterogeneity of the samples is a simple explanation for these differences, I compared the distributions for the subsets from different measurements of ar-197, ar-223 and the

chloroalkane-functionalized 197 (halo-197), respectively. I found that the data for the subsets (shown in Fig. A2.4) are rather consistent and their heterogeneity most probably does not fully account for e.g. the factor of two between median duty cycles of the different conjugates of 197 and 223, respectively.

My next aim was to evaluate, if the effect of different components in the fluorophore on its blinking behavior can be derived from the results of the library of SiR-based (benzo-)thiophene- and amide-functionalized fluorophores. One main finding was that by replacing the Ar_2 function with an alkyl chain, the fluorophore becomes non-blinking (196 and 210). Inserting a sulfone function between the nitrogen of the amide and Ar_2 also renders the fluorophore non-blinking (218 and 293). Having Ar_2, but replacing the (benzo-)thiophene with a dimethylamino-substituted benzene ring also gives a non-blinking fluorophore (267).

Evaluating the effect of the functionalization of Ar_2 on the blinking data was not possible, as the behavior was not consistent between antibody and HaloTag experiments and potential influences of the substituents were too small. Therefore, deducing whether the substituent primarily changed the electronic properties or simply interacted with the protein was not feasible. Introducing an electron-deficiency, either by having a pyridine group as Ar_2 (224) or by having an $-NO_2$ function in the para-position of Ar_2 (295) did not strongly increase the DC, as might be expected due to it stabilizing the emissive xanthylium form. But a main finding is that all tested (benzo-)thiophene-functionalized fluorophores with an aromatic Ar_2 function were good spontaneous blinkers. These results will be helpful in the design of new fluorophores.

Conclusion

In this chapter, I tested the potential spontaneous blinking of novel fluoreophores with a silicon-rhodamine (SiR) fluorescent core and a thiophene- or benzothiophene-fused fragment (Ar_1) modified with an amide, which, via nucleophilic attack of the nitrogen, can form a spirolactam and render the fluorophore non-emissive. With STORM imaging of fixed and live cells, I identified the spontaneous blinkers and recreated the cytoskeleton structure with a competitive spatial resolution of ~60-80 nm for the cross-section of the microtubule-primary-secondary antibody construct. Next, I found the PLL-bt and PLL-NTA assays investigated in the previous chapter to faithfully describe the blinking observed in cells, whereas I found that the APTES assay was not suitable. I used the *in vitro* assays to derive the (high-limit) on-time, off-time, (high-limit) duty cycle, number of cycles during the measurement and photon counts per on-event at single molecule conditions. The on-times of many are most likely below the measurements' temporal resolution of 10 ms, probably making the fluorophores suitable for MINFLUX imaging, which localizes with a few-nanometer precision within a few milliseconds. Most spontaneous blinkers also displayed a duty cycle likely to allow for MINFLUX imaging of densely labeled structures, for most even lower than for AF647 with an extremely high MEA concentration of 1 M to artificially decrease its duty cycle. Comparison of the data of a fluorophore in

the two *in vitro* assays indicated that the chemical environment of the protein, polyclonal antibody or HaloTag, has an observable impact on the blinking characteristics, highlighting the importance of examining fluorophores in a suitable environment. Finally, I deduced that all good blinkers had a thiophene- or benzothiophene-fused fragment (Ar_1) and an aromatic Ar_2 function attached to the nitrogen of the amide. My results laid the foundation for the application and optimization of this class of fluorophores for live-cell MINFLUX imaging.

Follow-up research successfully imaged the nuclear pore complexes of live cells with the spontaneous blinkers identified as suitable candidates in this chapter[38]. By fitting of confocal measurement data of the *in vitro* assays, on-times of a few milliseconds were calculated. This establishes the novel spontaneous blinkers as suitable fluorophores for live-cell MINFLUX imaging.

Publication and contributions

The results of chapter 2 have been published as follows:

Spontaneously blinking fluorophores for accelerated MINFLUX nanoscopy [38]

Michael Remmel, Lukas Scheiderer, Alexey N. Butkevich, Mariano L. Bossi, Stefan W. Hell

bioRxiv 2022.08.29.505670; doi: https://doi.org/10.1101/2022.08.29.505670

Submitted to 'Small' (currently under review).

Contributions for chapter 2:

Spontaneous blinker design and synthesis: Dr. Alexey Butkevich; Writing of Matlab evaluation script: Dr. Mariano Bossi.

Chapter 3: Microtubule-immobilizing *in vitro* assays for tracking of molecular motors

Aim

The next chapter describes the creation of a suitable *in vitro* microtubule assay by comparing different immobilization techniques. I envisioned using it for MINFLUX tracking measurements of fluorescently labeled kinesin and it should therefore have minimal background fluorescence by blocking unspecific binding to the surface. It furthermore must prevent significant movement of the immobilized microtubules, as this would induce measuring artefacts into the traces of, for instance, motor proteins walking on the microtubules. High stability of the microtubules over the time of the measurement, easy and reproducible construction and minimal modifications compared to microtubules in live cell conditions would also be advantageous.

Overview

The most biologically relevant system to study movement of molecular motors like kinesin are living cells, as their microtubules do not have unnatural modifications. However, growing and transfection of the cells with the plasmid of the motor is very tedious, making the system difficult to modify for screening or control experiments. Microtubules in live cells are dynamic, as they polymerize and depolymerize constantly and diffuse significantly in the cytosol, risking measuring artefacts in the traces. Furthermore, the choice of fluorophores is restricted to live-cell compatible ones and self-labeling tags need to be introduced, which can potentially alter the function of the motor.

In cellulo experiments with fixed cells minimize microtubule dynamics and, by permeabilizing the cell membrane, allow for the use of various fluorophores and recombinantly expressed molecular motors. But fixation randomly cross-links tubulins, rendering the microtubule surface unnatural. In all cell-based experiments, microtubule-associated proteins can partially block the surface, making the analysis of the motor stepping behavior difficult.

In vitro assays have the advantage to be comparably easy to modify and have no restrictions regarding the fluorophores or protein constructs used. They immobilize microtubules to the surface by binding on multiple positions along the microtubule, which makes the latter stationary and stiff. Tracked movements of the motor can hence be assigned mainly to its stepping. Microtubules for *in vitro* assays are typically polymerized from tubulin purified from animal tissue, but modifications need to often be introduced for immobilization or labeling purposes. During purification, microtubule-associated proteins can be removed to give highly pure tubulin, which can be polymerized to microtubules whose binding sites are unblocked. To keep microtubules from depolymerizing over the time span of the measurement, paclitaxel and GMPCPP can be added. As depolimerization is likely caused by hydrolysis

of GTP bound to tubulin to give GDP[39], it can be strongly delayed by using the slow-hydrolyzing GTP analogue GMPCPP. Paclitaxel specifically attaches to microtubules on the inside of the tubular structure and stabilizes them. With these additives, both the stability and stiffness of microtubules can be increased. Commonly used microtubule immobilization assays are based on aldehyde-, biotin- or antibody-modifications of the surface.

For the aldehyde modification, coverslips are reacted with APTES (as described earlier) to give a silanized, amino-functionalized surface, and subsequently treated with glutaraldehyde, so that the aldehydes react with the amines to give Schiff bases[40] (Fig. 3.1).

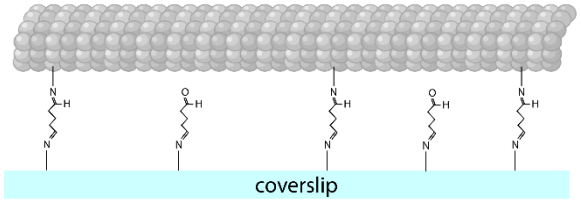

Figure 3.1: Illustration of the microtubule immobilization assay with APTES and glutaraldehyde.

If the other aldehyde does not form a Schiff base with a proximate aminosilane on the surface, it can covalently bind amino groups of microtubules, e.g. from the side chains of lysines.

Coating of the glass surface with biotin-based modifications is commonly done using BSA-bt. After streptavidin/neutravidin/avidin was specifically bound to the BSA-bt-covered surface, biotinylated microtubules can be immobilized[41]. Another common way for microtubule immobilization is via antibodies. Here, the coverslip surface is coated with antibodies that specifically bind tubulin.

Results and Discussion

3.1 Aldehyde assay

For identifying the best microtubule immobilization assay for tracking kinesin with MINFLUX, I started with testing the aldehyde assay. I treated APTES-coated coverslips with glutaraldehyde (GA). To avoid misjudgment of the assay's immobilization capability in case that microtubule polymerization failed, I used commercial, pre-formed microtubules. In a first test, I added pre-formed microtubules to the APTES-GA surface and imaged the sample with the paclitaxel-fuctionalized fluorophore germanium rhodamine (GeR-tub) added to visualize the microtubules, as it attaches to binding sites on their inside. The tests showed a deposition of the labeled microtubules onto the APTES-GA surface, but the fluorescent background was rather high (Fig. 3.2a). In the control where APTES was omitted and the coverslip was directly treated with glutaraldehyde, no deposition was observed (Fig. 3.2b). For another control of microtubule deposition directly onto APTES, fluorescent background was very high and I could not identify individual microtubules (Fig. 3.2c), which indicates that the hydrophobic surface of APTES does not effectively block unspecific binding. In a separate test, I immobilized

microtubules that were covalently labeled with fluorophores (Alexa Fluor 488) and biotins via linkers and tried blocking the surface with the amphiphilic protein casein. Microtubule immobilization was partially successful, but widefield videos indicated many microtubules to wobble, which revealed them not being strongly attached to the surface. Furthermore, background was comparably high, which would not allow for high-performing MINFLUX tracking. Hence, as microtubules were not necessarily immobilized specifically and not stable for multiple hours, I evaluated the assay to not be very useful.

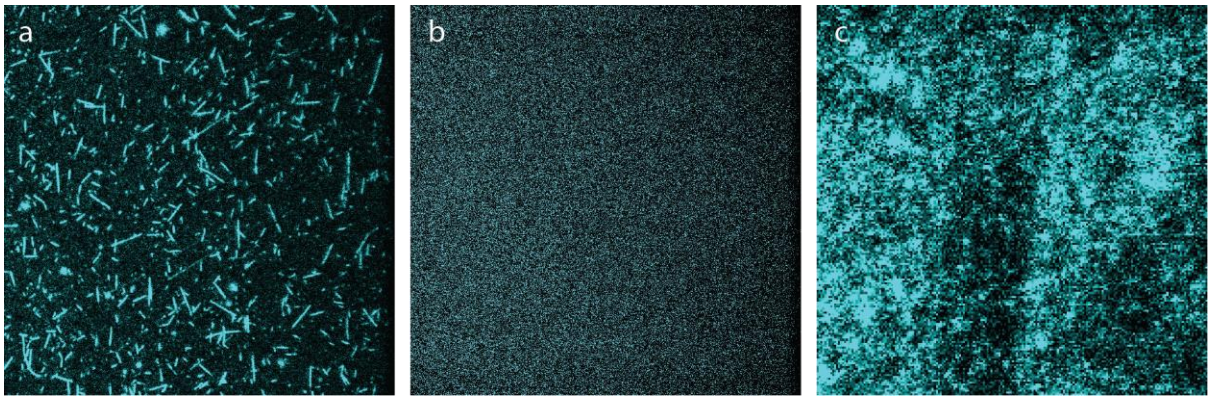

Figure 3.2: Confocal images of (**a**) the complete APTES-GA assay for immobilization of microtubules, (**b**) the control with APTES omitted and (**c**) the control with GA omitted. Size: a/b: 80 µm*80 µm, c: 20 µm*20 µm; Scalebar min/max: a/c: 0/50, b: 0/5.

3.2 Polymer-based assays

3.2.1 MAPT assay

To tackle the issue of fluorescence background, I envisioned a microtubule immobilization assay based on the PLL-NTA polymer tested in the previous chapters. The idea was to immobilize a his-tagged protein, which is known to attach to the microtubule surface, on the PLL-NTA coated surface. For this, I chose a truncated version (amino acids 1-383) of the microtubule associated protein tau (MAPT) recombinantly expressed with an N-terminal his-tag. As the four microtubule-binding repeat domains (amino acids 242 to 367) are included in this truncated version, one would expect them to bind to the microtubule parallel to the microtubule axis (as illustrated in Fig. 3.3).

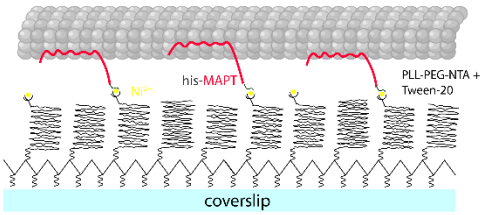

Figure 3.3: Illustration of the microtubule immobilization assay with PLL-NTA, Ni^{2+}, his-MAPT and microtubules.

I added the construct at a concentration of 1 µg/ml to the Ni^{2+}-loaded PLL-NTA coated surface and subsequently incubated the sample with microtubules. After addition of the

paclitaxel/Taxol-fuctionalized fluorophore ViaFluor 488 (VF488-tub), which visualizes microtubules, their successful immobilization became apparent (Fig. 3.4a). However, in a control experiment, where the ten-fold concentration (10 µg/ml) of his-MAPT was used, surface coverage with microtubules was not increased significantly (Fig. 3.4b). A similar coverage was also achieved, when his-MAPT was omitted and microtubules were directly added to the Ni^{2+}-loaded PLL-NTA coated coverslip (Fig. 3.4c), indicating that microtubules attached unspecifically, potentially via their histidines, arginines and glutamines, to the Ni^{2+}-NTA groups. Hence, his-MAPT did not have any observable additional immobilizing effect.

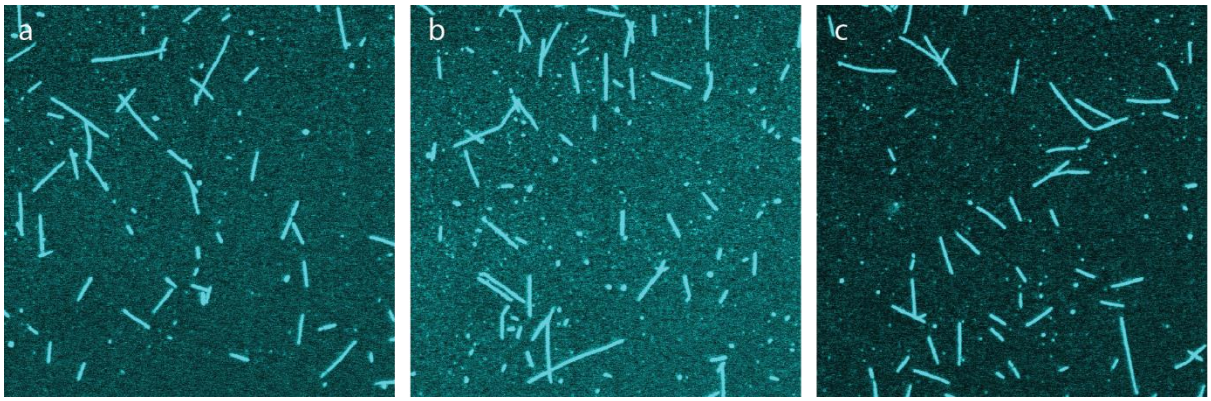

Fig. 3.4: Confocal images of (**a**) the complete MAPT assay with PLL-NTA, Ni^{2+}, his-MAPT and microtubules, (**b**) the control with increased his-MAPT concentration and (**c**) the control with his-MAPT omitted. Size: a/b/c: 60 µm*60 µm; Scalebar min/max: a/b/c: 0/50.

3.2.2 Antibody assay

As an alternative to immobilize unmodified microtubules, I created an antibody-based assay using the PLL-bt polymer. Similarly to the antibody immobilization assay, it consists of PLL-bt with Tween-20, neutravidin and a biotinylated antibody against α-tubulin (bt-DM1A). The bt-DM1A is assumed to be attached to the surface by the neutravidin bound to PLL-bt. I envisioned the α-tubulins in microtubules to attach to bt-DM1A, immobilizing them to the surface (as illustrated in Fig. 3.5).

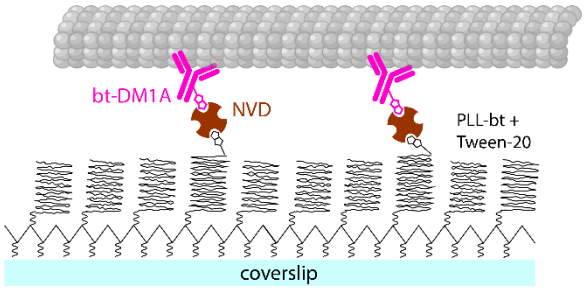

Fig. 3.5: Illustration of the microtubule immobilization assay with PLL-bt, NVD, bt-DM1A and microtubules.

The complete assay indeed immobilized unmodified microtubules visualized with VF488-tub (Fig. 3.6a). However, the control assay, in which bt-DM1A was omitted, gave a similar coverage,

indicating that the antibody did not have a significant specific immobilization enhancement effect (Fig. 3.6b). In another control, where both neutravidin and bt-DM1A were omitted, no significant immobilization took place, indicating that microtubules probably attached unspecifically to the neutravidins in the other assays (Fig. A3.1a). Reducing the concentration of the neutravidin solution by a factor of 10 in the complete assay resulted in a negligible microtubule coverage, substantiating the suspicion that microtubule attachment had primarily happened to neutravidin (Fig. A3.1b). I reached the conclusion that either bt-DM1A could not reach and immobilize microtubules in solution when attached to neutravidin in the polymer assay or that the antibodies might be blocked by α-tubulins from depolymerized microtubules, as the tubulins in a 1 µm long microtubule can potentially bind and block up to ~1500 DM1A antibodies.

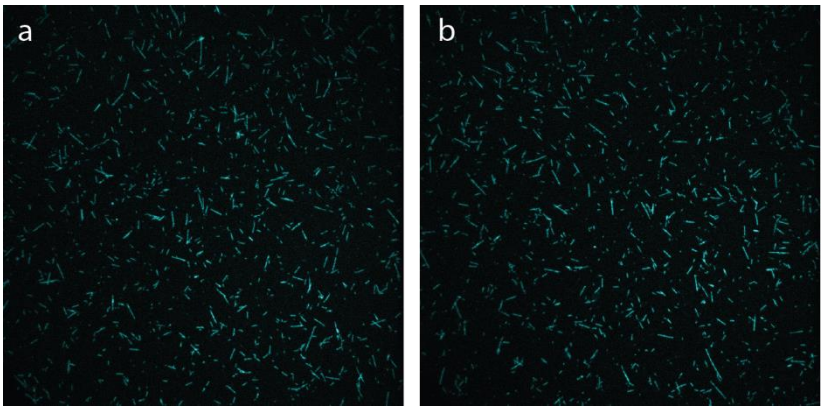

Fig. 3.6: Confocal images of (**a**) the complete antibody assay with PLL-bt, NVD, bt-DM1A and microtubules and (**b**) the control with bt-DM1A omitted. Size: a/b: 80 µm*80 µm; Scalebar min/max: a/b: 0/50.

3.2.3 Assay with biotinylated microtubules

As I had already shown that PLL-bt was suitable for MINFLUX measurements due to it effectively minimizing fluorescent background and because microtubule immobilization was not enhanced with biotinylated antibodies, I decided to create a PLL-bt-based assay with microtubules partially labeled with biotins and fluorophores (as illustrated in Fig. 3.7).

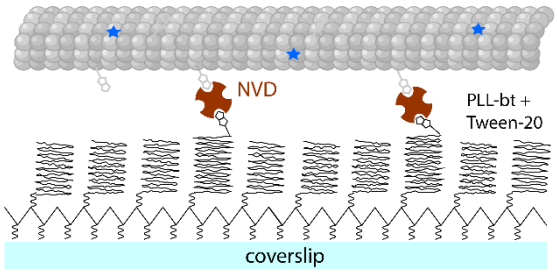

Figure 3.7: Illustration of microtubule immobilization assay with PLL-bt, NVD and biotinylated and fluorescently labeled microtubules (bt-MT-AF488).

I polymerized them from a mixture of highly pure ('cycled') tubulin (88%), biotinylated tubulin (10%) and tubulin labeled with the fluorophore Alexa Fluor 488 (2%) by adding GMPCPP. For the assay with

biotinylated and fluorescently labeled microtubules (bt-MT-AF488), I coated a coverslip with PLL-bt/T20, added neutravidin and the highly pure microtubules. For the complete assay, microtubules seemed to be immobilized strongly, as they did not show diffusive motion and were stable for many hours (Fig. 3.8a). In a control, I added a large excess of biotin before adding the microtubules, which significantly decreased the surface coverage with microtubules, as most of the binding sites of neutravidin were likely blocked with biotin (Fig. 3.8b). This clearly indicates that in the assay with PLL-bt/T20, neutravidin and bt-MT-AF488, immobilization of most microtubules happens specifically via the neutravidin-biotin bond. Another indication for specific immobilization is the enhanced stability over longer periods compared to the unspecific microtubule deposition in the antibody-based assay.

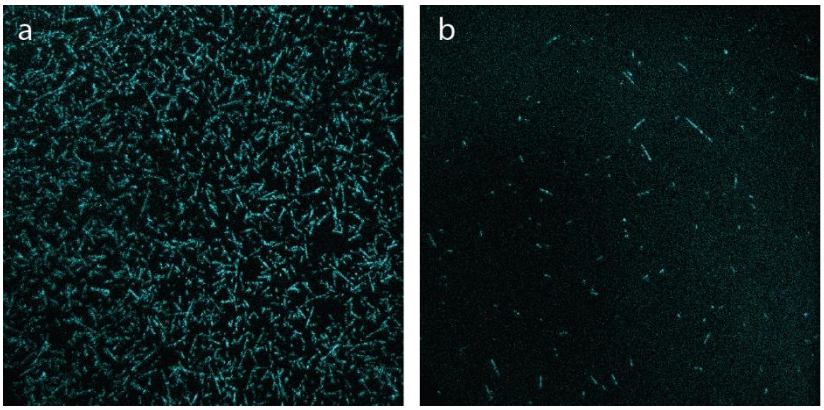

Fig. 3.8: Confocal images of (**a**) the complete biotinylated microtubule assay with PLL-bt, NVD and biotinylated and fluorescently labeled microtubules (bt-MT-AF488) and (**b**) the control with an excess of biotin added prior to the incubation of bt-MT-AF488. Size: a/b: 80 µm*80 µm; Scalebar min/max: a/b: 0/5.

To further test the functionality of immobilized bt-MT-AF488, I added a primary rabbit antibody (anti α-tubulin) and subsequently a secondary goat antibody (anti-rabbit) labeled with the fluorophore Alexa Fluor 647, which gave a strong signal in the red channel of confocal measurements, coinciding with the positions of the microtubules imaged in the channel of AF488 (Fig. 3.9). This indicates the assay's suitability to study microtubule-binding antibodies.

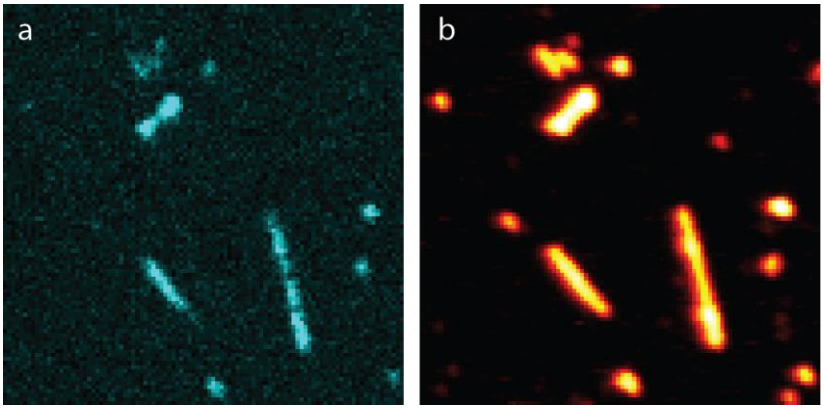

Fig. 3.9: Confocal images of two color channels of (**a**) microtubules (bt-MT-AF488) immobilized via the biotinylated microtubule assay and (**b**) the secondary (goat anti-rabbit) antibody labeled with Alexa Fluor 647 immobilized via the primary rabbit antibody (anti α-tubulin) to microtubules. Size: a/b: 20 µm*20 µm; Scalebar min/max: a: 0/50, b: 0/2000.

Omitting the primary antibody in a control experiment gave low homogeneous background signal in the red channel for the secondary antibody labeled with Alexa Fluor 647 (Fig. A3.2), indicating that the bt-MT-AF488 surface is free for anti-tubulin antibodies to bind and that the assay effectively minimizes unspecific binding of the antibodies. This highlights the assay's additional suitability to characterize fluorophores on antibodies labeling microtubules *in vitro*. In a separate experiment, I labeled the immobilized microtubules with a spontaneously blinking fluorophore (cTxl-249, chemical structure shown in Fig. 3.10).

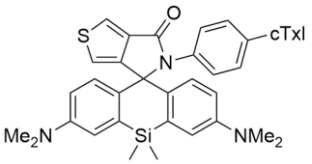

249-cTxl

Figure 3.10: Chemical structure of the spontaneous blinker 249 functionalized with cabazitaxel (cTxl), which specifically binds to the interior of microtubules.

The carbazitaxel-functionalized fluorophore in PBS was added to the microtubule assay and STORM images were recorded, which clearly show the microtubule structures and have a diffraction-unlimited spatial resolution of ~80 nm, as determined from the cross-section of the microtubules (Fig. 3.11).

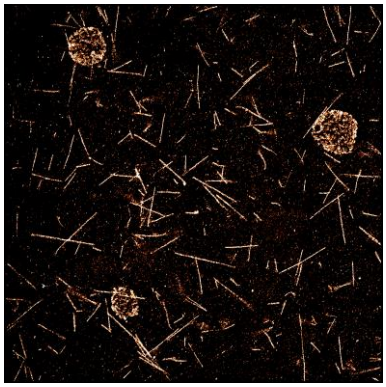

Figure 3.11: STORM images of microtubules (bt-MT-AF488) immobilized via the biotinylated microtubule assay and labeled with the cabazitaxel-functionalized spontaneous blinker cTxl-249. Imaging intensity (640 nm): 22 kW/cm^2; dwell time: 100 ms. Size: 51.2 μm*51.2 μm; Scalebar min/max: 0/5.

Conclusion

In this chapter, I compared different microtubule immobilization assays. Those based on his-MAPT or biotinylated antibodies did not have a significant and specific immobilization effect. The aldehyde-based assay with APTES and glutaraldehyde successfully immobilized microtubules, but fluorescence background, even after the addition of the blocking agent casein, was very high, binding to the surface was not necessarily specific and microtubules were not stable for very long. I found the most suitable *in vitro* assay for tracking kinesin with MINFLUX to be the one based on PLL-bt/T20, neutravidin and biotinylated and fluorescently labeled highly pure microtubules (bt-MT-AF488), where I showed microtubules to immobilize specifically and to remain stable over multiple hours.

Chapter 4: Kinesin-1 tracking with MINFLUX

Aim

The main project of this thesis is the tracking of kinesin using MINFLUX. For this objective, I created compatible *in vitro* samples based on the microtubule immobilization assay from the previous chapter with kinesin-1 constructs fluorescently labeled at different positions. For measuring the single steps of a few nanometers, we used a novel interferometric MINFLUX approach that has a steeper minimum compared to doughnut-based MINFLUX schemes, which we envisioned to be less vulnerable to background fluorescence. Tracking with MINFLUX would have several advantages over established techniques that have previously observed few-nanometer steps of kinesin. With the benefit of requiring only an ~1 nm small fluorescent label for a spatio-temporal resolution of few nanometers within ~1 ms, we aimed to observe substeps of kinesin-1 and thereby investigate controversial parts of its mechanochemical cycle. We also envisioned reconstructing the three-dimensional orientation of the unbound head during a substep by tracking different positions. With these findings, we intended to show-case MINFLUX for arguably minimally invasive tracking of protein displacements and rearrangements and to further clarify the detailed walking mechanism of kinesin-1, which in the future could be used to treat diseases linked to malfunctions of the motor protein.

Overview

The walking of kinesin-1 on microtubules has been extensively studied with various tracking techniques, making it a gold standard model system for evaluating the performance of a method. It is a homodimeric protein consisting of two identical heads that are connected by a coiled-coil stalk. The heads can bind to microtubules on tubulin dimers (α- and β-tubulin), which have a spacing of ~8 nm. By binding and hydrolyzing ATP, kinesin can walk along a protofilament of the microtubule with the rear head detaching and then re-attaching ~16 nm further in the plus-end direction of the microtubule, which displaces the center-of-mass of the motor by ~8 nm. The velocity increases with higher ATP concentrations, yielding average step times of a few milliseconds at physiological conditions.

With the fluorescence-based tracking technique Fluorescence Imaging with One-Nanometer Accuracy (FIONA), individual 16 nm steps of the kinesin-1 head labeled with a single fluorophore were identified with a spatio-temporal resolution of a few nanometers in ~330 ms by slowing the motor down drastically with sub-micromolar ATP concentrations. These 16 nm steps are a clear indication that kinesin-1 moves in a ‘hand-over-hand’ fashion and are contrary to an ‘inchworm’ mechanism, where the trailing head (TH) never overtakes the leading head (LH), resulting in 8 nm regular steps of the head (as illustrated in Fig. 4.1).

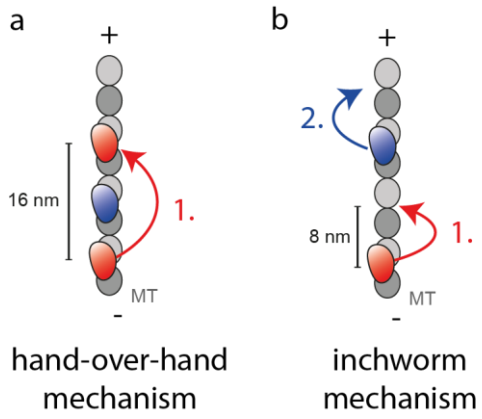

Figure 4.1: Illustration of (**a**) the hand-over-hand mechanism and (**b**) the inchworm mechanism proposed for kinesin-1. With the hand-over-hand mechanism, in which the trailing head overtakes the leading head, 16 nm steps are expected. For the inchworm mechanism, in which the trailing head never overtakes the leading head, 8 nm steps are expected.

Based on Förster-Resonance Energy Transfer (FRET) data, a few-millisecond long intermediate state, during which only one head is microtubule bound, has been hypothesized over a decade ago. This so-called one-head-bound (1HB) state, resulting from kinesin making a so-called substep, is particularly interesting, as detachment of kinesin from the microtubule, which is increased in many diseases[42], most likely happens via the 1HB state[43]. By measuring the relative distances between multiple positions on both heads, the FRET studies reconstructed possible orientations of the unbound head in the 1HB state, but due to the indirect measurement could not pin down a specific one.

Direct observation of this short-lived state was made possible by attaching a ≥30 nm diameter large gold bead to a kinesin head in scattering-based tracking (as illustrated in Fig. 4.2), which gave a spatio-temporal resolution of a few nanometers within ~1 ms. Interestingly, two independent studies came to opposing conclusions regarding the question in which states ATP is bound and hydrolyzed, respectively. The first study, which used a construct with an N-terminal AviTag to bind a biotinylated gold bead and an interferometric Scattering (iSCAT) microscope, concluded ATP to bind to the leading head when both heads are associated with the microtubule, so during the two-head-bound (2HB) state[44]. The second study tracked a cysteine-light construct, which was functionalized with a biotin on a surface-exposed cysteine to bind a biotinylated gold bead via streptavidin, using total internal reflection Dark-Field Microscopy (DFM). Contradictorily, they identified the 1HB state to be ATP-binding[45]. Some effort has been made to resolve this controversy by proposing that the bead's attachment position on the head strongly influences the traces, but this detail of the mechanochemical cycle still remains highly elusive. In general, it has been shown by simulations that tracking beads >200 times larger in volume than the kinesin head it is attached to is highly artefact-prone, probably making the previous results significantly less reliable[15].

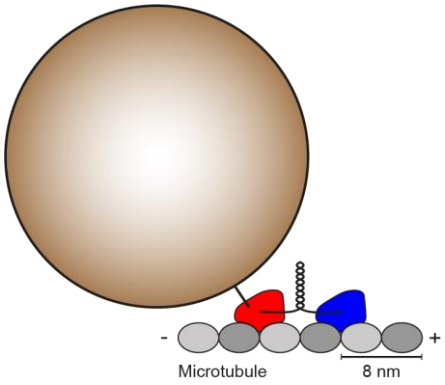

Figure 4.2: Illustration of the scattering-based bead tracking assay of kinesin. Bead, kinesin heads and tubulins are drawn to scale.

The substeps of kinesin-1 have recently also been observed by an optical trap experiment using ~70 nm diameter large germanium nanospheres with a very high refractive index attached to the stalk, yielding a spatio-temporal resolution of a few nanometers within ~1 ms (as illustrated in Fig. 4.3). Thereby, the motor's center-of-mass was tracked and 4 nm large, few-millisecond long center-of-mass substeps observed at up to physiological ATP concentrations. However, as the steps of the heads were not observed directly, an unambiguous conclusion to what state of kinesin binds ATP was not possible. Furthermore, optical traps require the application of artificial forces that could alter the motor's natural movement.

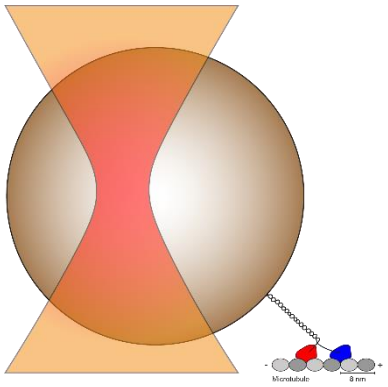

Figure 4.3: Illustration of the optical trap tracking assay of kinesin. Bead, kinesin heads and tubulins are drawn to scale. The optical trap (orange) applies an artificial force in the direction opposite to the walking direction.

Another controversial question about the detailed stepping mechanism of kinesin-1 is whether the coiled-coil stalk rotates. In a symmetric hand-over-hand mechanism, where the trailing head always passes the leading head on the same side, a unidirectional rotation is expected (Fig. 4.4a). In an asymmetric mechanism, the trailing head would pass the leading head alternatingly on both sides, leading to either a non-existing or back-and-forth rotation of the coiled-coil stalk (Fig. 4.4b). In one study, an inverted assay was studied, in which single kinesins immobilized to the surface moved individual microtubules over the sample surface[46]. Due to a lack of significant rotation of the microtubule, a symmetric rotation of the coiled-coil stalk was ruled out. A later study tracked

fluorophores attached to a bead bound to the coiled-coil stalk and deduced a mostly asymmetric mechanism with rare occurrences of symmetric movements, leading to the coiled-coil irregularly revolving by ~180°[47]. However, one optical trap study used highly birefringent microspheres attached to the stalk to measure the torque produced by kinesin and suggested that the motor rotates unidirectionally, favoring a symmetric hand-over-hand mechanism[48].

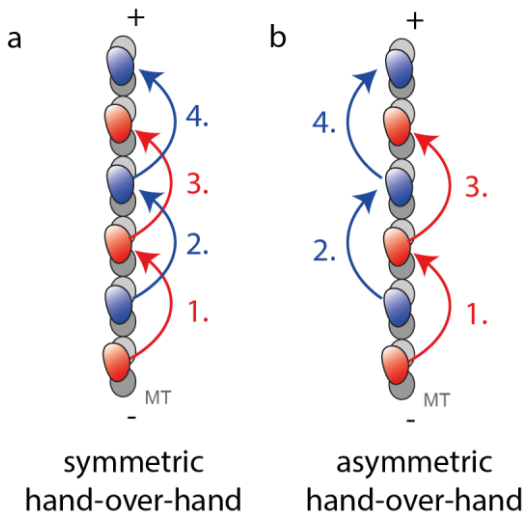

Figure 4.4: Illustrations of (**a**) a symmetric hand-over-hand mechanism and (**b**) an asymmetric hand-over-hand mechanism.

These unresolved questions motivated me to use MINFLUX for tracking of kinesin-1 and investigating the respective orientations of heads and stalk during unrestricted stepping by localizing only a small fluorescent label.

Results and Discussion

4.1 Phase-scanner

To enhance the impressive spatiotemporal resolution of MINFLUX further, a novel approach was tried in which a pair of oblique beams interfere destructively in the focal plane, giving a line-shaped minimum (LSM) of the excitation beam. By changing the phase difference (from 180°) with a phase modulator, the excitation minimum can be shifted with Ångström precision, which is suitable for performing MINFLUX iterations. As line-shaped minima provide a higher steepness and cause lower background signal, they were assumed to achieve a better spatio-temporal resolution compared to excitation doughnuts previously used for MINFLUX tracking. Two-dimensional tracking can be performed by switching between line-shaped minima oriented in x- and y-direction, respectively. Further details on the MINFLUX measurements are given in the methods section (appendix).

4.2 Kinesin labeling

For the tracking of kinesin, I used cysteine-light mutants of human kinesin-1 (KIF5B) that were truncated at the coiled-coil stalk after amino acid position 560 and had a his_6-tag added at the C-terminus

for purification purposes. All surface-exposed cysteines had been mutated to a serine or an alanine and a single cysteine was added at the desired position by QuikChange site-directed mutagenesis. I labeled this cysteine with ATTO 647N-maleimide (in DMSO) over night at 4 °C, as cysteines are known to react with maleimides in a thiol-Michael addition, covalently attaching the fluorophore via a linker to the protein. I removed unreacted fluorophore-maleimide by size-exclusion chromatography. Further details are given in the methods section (appendix).

I chose constructs with the labeling position on the stalk (construct N356C; label at amino acid 356), at the rear (construct K28C; label at amino acid 28), center right (construct T324C; label at amino acid 324) or front (construct E215C; label at amino acid 215), respectively, of the head with respect to the walking direction and the microtubule defined as bottom (as illustrated in Fig. 4.5).

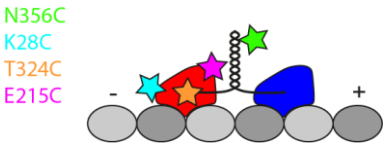

Figure 4.5: Illustration of kinesin-1 on microtubule (grey) with labeling positions for N356C (stalk, green), K28C (rear of head, cyan), K324C (center right of head, orange) and E215C (front of head, magenta).

For the head constructs, I aimed for a low DOL to decrease the chances of both heads carrying a fluorophore, which would impede tracking a single head. Using a combination of UV-Vis spectroscopy and mass spectrometry, I adjusted the amount of fluorophore-maleimide added to give a DOL smaller than 0.6, which makes the chances of a kinesin dimer to carry two fluorophores lower than 36%. The DOL was determined from the UV-Vis spectra (Fig. A4.1a) using the absorbance of the protein at 280 nm and of ATTO 647N at 650 nm using the equation

$$DOL = \frac{(A_{max}/\varepsilon_{max})}{(A_{prot}/\varepsilon_{prot})} = \frac{A_{max}*\varepsilon_{prot}}{(A_{280}-A_{max}*CF280)*\varepsilon_{max}} \qquad \text{(eq. 7)}$$

where A_{max} is the absorbance at λ_{max}, ε_{max} is the extinction coefficient of the fluorophore at λ_{max}, A_{prot} is the absorbance of the protein at 280 nm, ε_{prot} is the extinction coefficient of the protein at 280 nm, A_{280} is the absorbance at 280 nm and the correction factor $CF280$ is the ratio between the extinction coefficient of the fluorophore at 280 nm and its extinction coefficient at λ_{max}. As the constants for the fluorophore were determined for the unconjugated dye in buffer, the calculated DOL can be off slightly due to potential (quenching) interactions with the protein.

Therefore, I also determined the DOL using the peaks of the mass spectra corresponding to the unlabeled and labeled protein monomer, respectively (Fig. A4.1b). Under the assumption, that the added fluorophore changes the ionizability of the protein only insignificantly in Electrospray Ionisation (ESI), the DOL was estimated by dividing the size of the peak for the labeled protein by the sum of the

sizes of both peaks. The UV-Vis and MS data listed in Table A4.1 show comparable results for both methods.

I chose not to decrease the DOL further for getting an even lower change of a dimer having two labels, as this would also decrease the fraction of dimers with one label, reducing the chances to observe a walking kinesin. This reduction of active fluorophore-labeled kinesins could not simply be compensated by increasing the concentration of the motor, as microtubules were observed to start moving for to high kinesin-1 concentrations.

After having determined the DOL, I added sucrose (10% w/v) to the kinesin solution as stabilizing agent during freezing. The solution was aliquoted, flash-frozen in liquid nitrogen and stored at -80 °C.

4.3 Activity assays

Next, I investigated, if the fluorescent labeling and mutating of kinesin, the fluorescent labeling and biotinylation of microtubules or the flash-freezing and thawing had an effect on the activity of the motor on microtubules. For this purpose, I employed a commercial ATPase Endpoint assay based on the photometric quantification of produced phosphate as kinesin converts one ATP to one ADP and one phosphate per 8 nm step on the microtubule. For a complete sample, I added 1 µg of kinesin to a solution of microtubules in a well-plate with a final concentration of ~67 µg/ml, stabilized with 20 µM Taxol (Txl, also called paclitaxel) added in the commercial low-salt kinesin reaction buffer (KRB01). Next, I added ATP to a concentration of ~330 µM and, after 5 minutes at room temperature, stopped the reaction by adding the commercial CytoPhos reagent. After 10 minutes, I recorded the absorption spectra in a plate reader.

To determine the amount of phosphate produced by the motor, I calibrated the system by adding the CytoPhos reagent to known amounts of phosphate in MilliQ water. After 10 minutes, I recorded the absorption spectra in a plate reader and plotted a linear calibration curve of the absorptions at 650 nm versus the different amounts of phosphate (Table A4.2, Fig. A4.2).

To determine if the labeling, purification or flash-freezing of kinesin with ATTO 647N-maleimide had a detrimental effect on its activity, I measured the absorbance at 650 nm for samples with the constructs E215C and T324C, both labeled and unlabeled (Table A4.3). For comparison, I also measured a commercial recombinantly expressed human kinesin with an N-terminal GST-tag with unmutated cysteines (KR01), provided in lyophilized form. For the negative controls, I omitted ATP. The determined rates in Fig. 4.6 show clearly, that the activity is significantly higher when ATP is present and is similar for all constructs. Without ATP, the activity is near-zero. The slightly negative values can be explained by the error in the fitted calibration curve. Furthermore, no clear difference between the activities of labeled and unlabeled constructs is apparent, which are also in the same range as that of the

commercial human kinesin KR01 used as reference. This indicates that the labeling, mutating, purification or the flash-freezing did not drastically change the motor's activity.

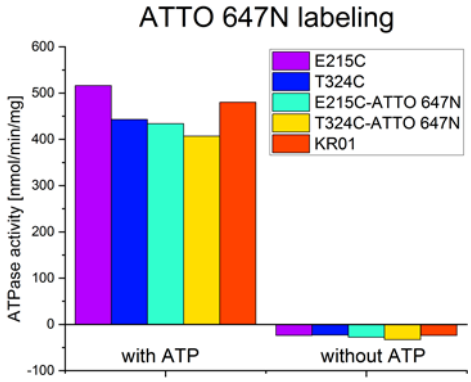

Figure 4.6: ATPase activity of unlabeled and labeled kinesin-1 constructs E215C, T324C and unmutated KR01. Negative controls were without ATP added.

Next, I investigated, whether modifications on microtubules or stabilizing agents prevented kinesin from being active on microtubules. I used both labeled constructs E215C and T324C in respective combination with different microtubules. As stabilizing agents, I chose 20 µM of cabazitaxel (cTxl), Taxol (Txl) and ViaFluor 488-Taxol (VF488-tub), respectively, in combination with pre-formed commercial microtubules (MT) freshly dissolved from their lyophilized form. To analyze, if freezing of microtubules for long-term storage purposes rendered them non-functional, I flash-froze pre-formed microtubules in liquid nitrogen, re-thawed and stabilized them with Txl. To further see if biotinylation of microtubules blocks the protofilaments, preventing long tracks and high activity for kinesin, I polymerized biotinylated microtubules (bt-MT(2%) and bt-MT(20%)) with different degrees of biotinylation from a mixture of tubulin with 2% and 20% biotinylated tubulin, respectively, by adding GMPCPP. I measured samples with bt-MT(2%) and bt-MT(20%) with 20 µM Txl to see, if the degree of biotinylation had an effect on activity. Finally, I measured a control without microtubules added. I prepared all samples in the commercial low-salt kinesin reaction buffer (KRB01). After a 5 minute incubation with ATP (~330 µM), I added the CytoPhos reagent. I recorded the absorbance at 650 nm (Table A4.4) in a plate reader 10 minutes later. The results in Fig. 4.7 show, that activity is significantly higher for all types of microtubules and stabilizing agents compared to the near-zero activity of the control without microtubules. Activities were similar between both labeled kinesin constructs. The differences in activity between bt-MT(2%) and bt-MT(20%) were within the variation between samples. All three samples with stabilizing agents (cTxl, Txl, VF488-tub) added to freshly dissolved pre-formed microtubules had slightly lower activity, possibly due to incomplete dissolving of the microtubules. In general, I concluded that neither biotinylation of the microtubules nor flash-freezing or addition of the stabilizing agents drastically impaired kinesin's activity on microtubules.

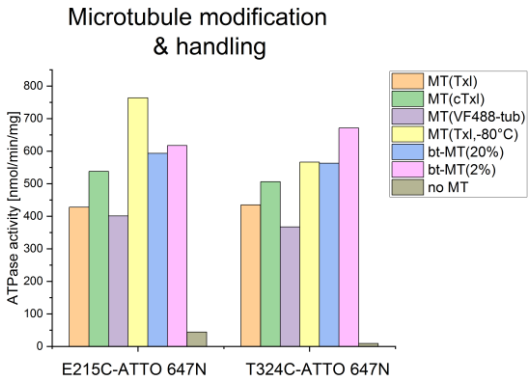

Figure 4.7: ATPase activity of pre-formed microtubules with Taxol (MT(Txl)), pre-formed microtubules with cabazitaxel (MT(cTxl)), pre-formed microtubules with VF488-tub (MT(VF488-tub)), flash-frozen pre-formed microtubules with Taxol (MT(Txl)), biotinylated microtubules with Taxol with 20% biotin-functionalized tubulin (bt-MT(20%)) and 2% biotin-functionalized tubulin (bt-MT(2%)) and control without microtubules (no MT) added.

4.4 Kinesin assays

In the field of kinesin research, two *in vitro* assays are commonly used, namely the kinesin motility assay (KMA), where single kinesins walk on immobilized microtubules, and the kinesin inverted assay (KIA), where microtubules are transported by immobilized kinesins. To visualize the motor's activity as found by the activity assay in an *in vitro* system, I created a KIA by coating a coverslip with PLL-NTA/Tween-20, loading the NTA groups with Ni^{2+} from $NiCl_2$ and immobilizing fluorescently labeled kinesins (E215C-ATTO 647N) via the C-terminal his_6-tag on their stalk to the surface. Added pre-formed microtubules, visualized by VF488-tub and stabilized with Txl, were transported along their longitudinal axis in the presence of 1 mM ATP, as shown by the two microtubules in the confocal images recorded with ~30 seconds time intervals (Fig. A4.3).

Microtubules were only transported for higher surface coverages with kinesin (see Fig. A4.4), so identifying and tracking single active labeled kinesins in an inverted assay with MINFLUX seemed to be rather difficult. In principle, one could predict the path of a microtubule on the surface and potentially bleach an area of interest until only one fluorophore is emissive, but as these measurements would not represent motors walking under physiological conditions very well and the speed of the microtubules (~100 nm/s) at an ATP concentration of 1 mM was significantly smaller than that expected for single kinesins, I set the focus of further investigations with the kinesin motility assay.

As I had found the assay consisting of PLL-bt/T20, neutravidin and biotinylated and fluorescently labeled microtubules (bt-MT-AF488; modifications: 10% biotin, 2% Alexa Fluor 488)) to best minimize unspecific binding and immobilize the microtubules strongly and specifically, I used it as the template for the kinesin motility assay. To that, labeled kinesin, ATP and additives were added. I used 1 mM dithiothreitol (DTT) to reduce formation of intermolecular disulfide bonds and 20 µM Txl to stabilize microtubules. To minimize bleaching of the fluorophore, oxygen needed to be removed from the sample. Commonly, an oxygen scavenging system (OSS) is added, consisting of an

oxygen-consuming enzyme (pyranose oxidase or glucose oxidase), a substrate (glucose) and optionally a catalase to remove produced hydrogen peroxide. However, as the OSS produced some fluorescent background, I decided to remove oxygen with a hypoxia workstation. For this, I prepared the kinesin buffer in the chamber where the oxygen level is set to ~0.3% and sealed the flow chamber before measurements.

As singlet oxygen can bring fluorophores in a long-lived triplet dark state back to the ground state, removing it leads to significant blinking. Therefore, I added 1 mM of ascorbic acid (AA) and 1 mM of methyl viologen (MV) as reducing and oxidizing system (ROXS) to recover fluorophores from their dark state, which ensures a continuous photon emission with a higher rate, both of which are essential for tracking. As buffer, PM15 was used, prepared by dissolving 15 mM piperazine-N,N'-bis(2-ethanesulfonic acid) (PIPES) and 2 mM magnesium chloride (MgCl2) in Milli-Q water and titrating it with a solution of sodium hydroxide to a physiological pH of 7.4.

With this assay, I observed clear movement of labeled kinesins on microtubules and we recorded first tracks with MINFLUX. However, the yield of traces with clear steps was low and increasing of the kinesin concentration lead to the motors unspecifically binding more the surface, probably to neutravidin, as was apparent from Total Internal Reflection Fluorescence (TIRF) measurements. Therefore, I envisioned blocking the surface between microtubules (as illustrated in Fig. 4.8). I added BSA-bt at a high concentration (100 µg/ml) after the deposition of the microtubules and incubated for 30 minutes. After this treatment and with 10 µg/ml BSA-bt added to give the final measuring buffer, unspecific binding was strongly reduced and kinesin activity on the microtubules drastically enhanced. The TIRF measurements of the channels of microtubules and kinesins showed that most kinesins attach to microtubules. Evaluation of the TIRF data revealed that most kinesins walked long paths on microtubules, on average ~2 µm, often reaching the microtubule end. With the optimized samples, a reproducible recording of many MINFLUX traces was possible.

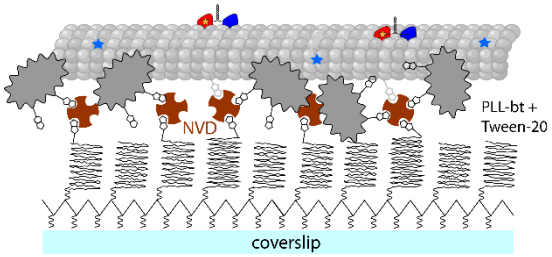

Figure 4.8: Illustration of kinesin motility assay with PLL-bt, NVD, biotinylated and fluorescently labeled microtubules (bt-MT-AF488) and BSA-bt for blocking.

4.5 MINFLUX tracking

4.5.1 Substeps and stalk rotation of kinesin

For tracking the movement of the stalk, we used construct N356C labeled with ATTO 647N-maleimide on its surface-exposed cysteine in the coiled-coil (as illustrated in Fig. 4.9a). I chose to mutate amino acid 356 to a cysteine by site-directed mutagenesis, as this position is close to the heads, but is still distant enough to make a potential interference of the fluorophore with the walking improbable. With this construct, we recorded one-dimensional (1D) traces with MINFLUX to get twice the temporal resolution compared to two-dimensional (2D) measurements and because we were most interested in best resolving the steps along the longitudinal axis of the microtubule.

We successfully recorded many traces (with up to ~180 nm length) of N356C-ATTO 647N-DOL1 carrying a single fluorophore at a sub-physiological ATP concentration of 10 μM, showing clear plateaus and steps, as can be seen in the example traces in Fig. 4.9b. For this condition, we recorded 1739 steps in total with a median step size precision of 0.63 nm (Fig. 4.9c), as determined from the plateau durations and step sizes. With ~100 photons per ~1 ms localization, we achieved a median plateau standard deviation of 1.8 nm. From the zoom-ins of the example traces, the occurrence of 8 nm steps, corresponding to a full center-of-mass step, and 4 nm steps, corresponding to a center-of-mass substep, are apparent (Fig. 4.9d). The histogram of all recorded step sizes, that were determined by a step-fit function based on an iterative change point search, features, apart from a small fraction of backsteps, mainly forward steps between 3 nm and 11 nm with two maxima around 4 nm and 8 nm (Fig. 4.9e). This indicates a variability in fitted step sizes, but shows a clear occurence of both regular steps and substeps, of which the latter have previously only been directly observed with bead-based techniques. Hence, MINFLUX is the first technique to reveal substeps of kinesin labeled with only a single fluorophore label. Contrary to the optical trap measurements using ~70 nm large germanium nanospheres, which recently observed center-of-mass substeps, our measurements did not require applying a force to the system.

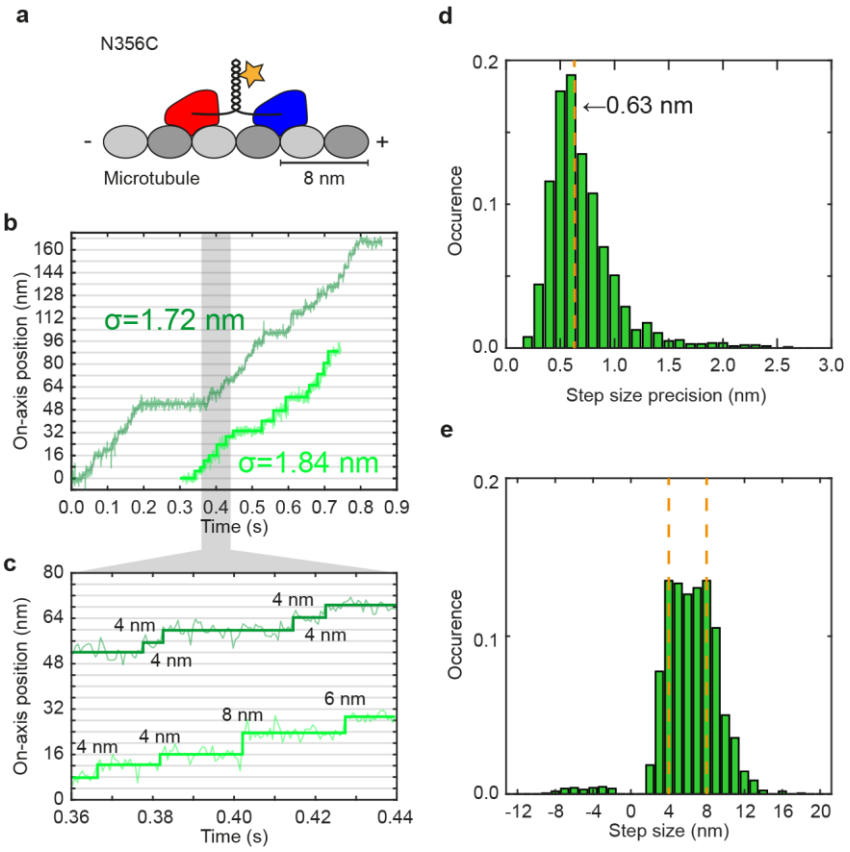

Figure 4.9: MINFLUX tracking ovserved 4 nm center-of-mass substeps of kinesin-1. (**a**) Illustration of N356C-ATTO 647N-DOL1 on a microtubule with the fluorophore on the stalk. (**b**) Exemplary traces of N356C-ATTO 647N-DOL1 at 10 µM ATP with overlaid detected step functions. (**c**) Zoom-in of the traces in (b) showing the occurrence of 4 nm substeps. (**d**) Step size precision histogram. (**e**) Step size histogram with regular 8 nm stepsize and 4 nm substep size highlighted.

Next, we recorded 1759 steps of N356C-ATTO 647N-DOL1 at a higher, physiological ATP concentration of 1 mM. The first observation of the step size histogram was that the substep peak disappeared, indicating that at higher ATP concentrations, substeps become rare. Interestingly however, the histogram does not exhibit a peak at 8 nm, as would be expected for regular steps, but looks like a superimposition of two peaks with maxima at ~6 nm and ~10 nm, respectively. Plotting the size of a step against the size of the next one in a 2D histogram shows a broad distribution of consecutive steps with a sum of ~16 nm, indicating an alternation between steps larger and smaller than 8 nm (Fig. 4.10).

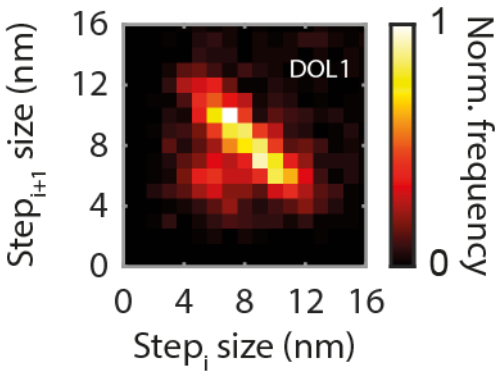

Figure 4.10: 2D step size histogram of N356C-ATTO 647N-DOL1 for 1 mM ATP for steps (i) versus next steps (i+1), displaying a broad distribution of consecutive steps totaling 16 nm step size.

I argued that this behavior is likely due to a rotation of the stalk during a step, as the fluorophore does not faithfully represent the center of the coiled-coil. The visualization in Fig. A4.5a shows, how the labeled amino acid is displaced from the longitudinal coiled-coil axis by ~1 nm and the linker (whose structure was determined by MM2 energy minimization in Chem3D Pro (Perkin Elmer)) displaces the fluorophore core by another ~1 nm from the axis.

With this idea, I could explain the occurrence of alternating ~6 nm and ~10 nm steps with a significant rotation of the stalk during a step. As illustrated in Fig. 4.11a, when the fluorophore is pointed in walking direction and the stalk moves forward by 8 nm during a full step, a stalk rotation, after which the fluorophore is pointed backwards, results in a reduced net displacement (<8 nm) of the fluorophore. After the next step and rotation of the stalk, the fluorophore will again be extended from the coiled-coil axis in walking direction, which causes a larger net displacement (>8 nm) than that of the stalk (~8 nm).

To test this hypothesis, I labeled construct N356C with an excess of ATTO 647N-maleimide, so that the cysteines on both coils of the stalk of the kinesin-1 dimer carry a fluorophore (as illustrated in Fig 4.11b).

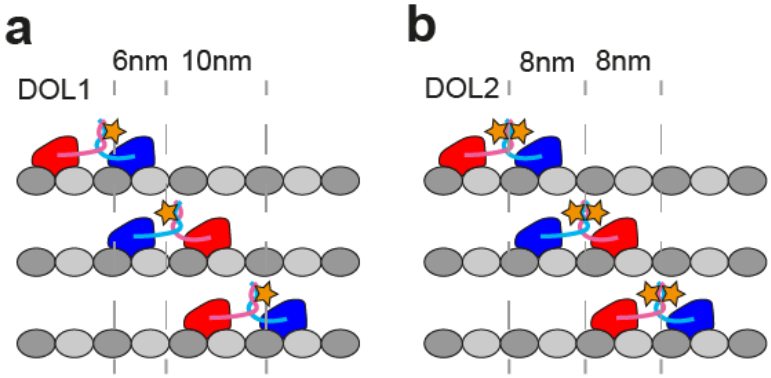

Figure 4.11: Illustration of (**a**) N356C-ATTO 647N-DOL1 and (**b**) N356C-ATTO 647N-DOL2 on microtubules predicting a smaller step size asymmetry of the construct carrying two fluorophores.

The idea behind this was, that the center-of-mass of the emission pattern of both equally emissive fluorophores would coincide with the stalk axis, which should remove the asymmetry of steps for one fluorophore (Fig. A4.5b). The complete labeling of N356 with two fluorophores per kinesin-1 dimer to give a degree of labeling of 2 (DOL2) was shown by mass spectroscopy (ESI), as only the peak of the labeled monomer was visible. We recorded traces with this construct N356-ATTO 647N-DOL2. To remove contributions of kinesins on which only one fluorophore was emissive and the other one was either bleached or in a long-lived dark state, steps corresponding to a photon rate <125 kHz, a threshold inferred from the measurements of N356-ATTO 647N-DOL1, were omitted. This procedure gave 625 steps corresponding to kinesin with two emissive fluorophores. As expected, the histogram of step sizes of N356-ATTO 647N-DOL2 shows a clear peak at 8 nm and the distribution in the 2D histogram of steps and consecutive steps is much more narrow (Fig. 4.12).

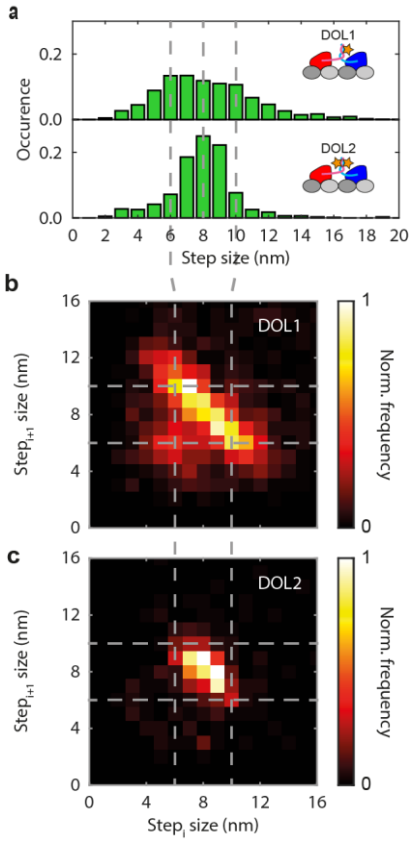

Figure 4.12: (**a**) Step size histograms of N356C-ATTO 647N-DOL1 and N356C-ATTO 647N-DOL2 at 1 mM ATP. (**b**) 2D step size histogram of N356C-ATTO 647N-DOL1 for steps (i) versus next steps (i+1) displaying a broad distribution. (**c**) 2D step size histogram of N356C-ATTO 647N-DOL2 for steps (i) versus next steps (i+1), displaying a comparably narrower distribution.

Out of the traces, I identified one with a bleaching step that nicely compares the step sizes with one and two emissive fluorophores (Fig. 4.13). Before the bleaching event, the steps are ~8 nm large and show no systematic sequence, but after one of the fluorophores bleached, as can be clearly seen by the drop of the photon counts, the step sizes alternate between ~6 nm and ~10 nm.

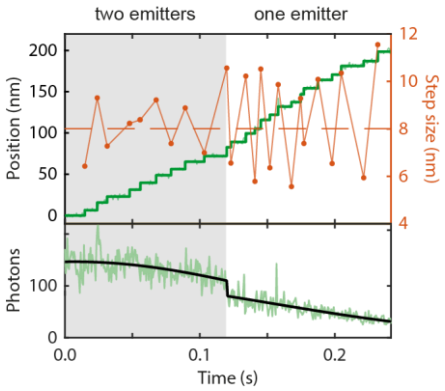

Figure 4.13: Exemplary trace of N356C-ATTO 647N-DOL2 with one emitter bleaching after ~0.12 s as evident from the photon trace (bottom), after which step sizes alternate strongly between ~10 nm and ~6 nm. The overall decrease in photons is caused by kinesin walking out of the confocal volume.

All these findings indicate, that the stalk rotates significantly during a full step. The rotation is most probably around 180°, as the difference between smaller (~6 nm) and larger (~10 nm) steps is ~4 nm, which is the maximum spacing between the fluorophore in the front compared to the fluorophore in the back with respect to the walking direction, and a smaller rotation would cause a smaller displacement along the longitudinal microtubule axis. Therefore, the assumption is that the stalk is rotated halfway around its axis during a full step. However, the controversial question whether the following step reverses the rotation (asymmetric) or continues the rotation in the same direction (symmetric) cannot be determined from this experiment alone and will be discussed further in a later section.

4.5.2 ATP binds in one-head-bound (1HB) state

Another longstanding open question in the field of kinesin research is, whether ATP binds when both heads are microtubule-bound (2HB) or when one head is detached and between binding sites (1HB) and in which of the states ATP is hydrolyzed. As it cannot be answered by tracking the stalk, I used the construct T324C-ATTO 647N, where the labeled cysteine is located on the head at the C-terminal end of the α6-helix and is adjacent to the neck linker that connects the head with the stalk. If the microtubule center is defined as down in the coordinate system of the microtubule-bound head, the labeling site is in the center of the head's right side with respect to the walking direction (Fig. 4.14).

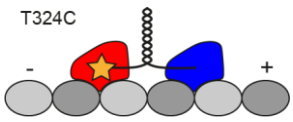

Figure 4.14: Illustration of labeled T324C on a microtubule with the fluorophore on the right center of the head (with respect to the walking direction (from – to +)).

We recorded 2D traces to determine both the on-axis displacement and the off-axis displacement of the head during a step, with respect to the longitudinal microtubule axis. The median spatiotemporal resolution was ~4 nm with ~20 photons recorded in ~0.63 ms. We measured at ATP concentrations of

10 µM, 100 µM and 1 mM to identify whether the duration of the 1HB state or 2HB state depends on the ATP concentration (exemplary traces shown in Fig 4.15).

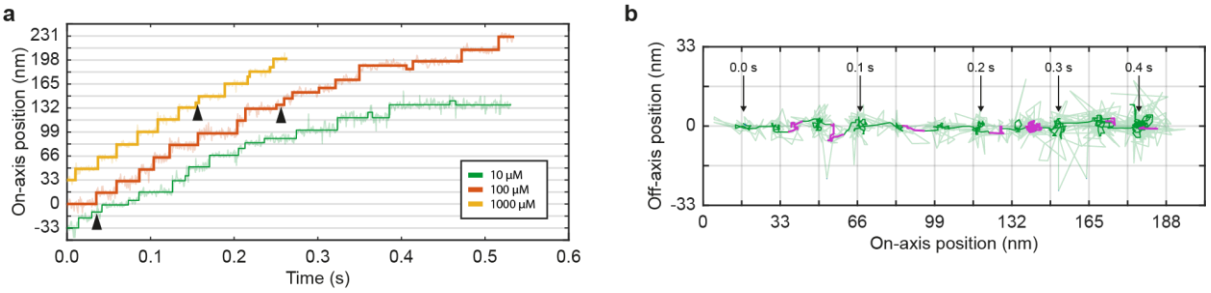

Figure 4.15: (**a**) Exemplary traces of T324C recorded at 10 µM (green), 100 µM (orange) and 1 mM (yellow) ATP with black arrows highlighting substep plateaus. (**b**) 2D visualization of the 10 µM trace in (a) showing the unbound state highlighted in magenta.

As now the head is tracked, regular steps are ~16 nm large, because the trailing head moves forward to the next but one binding site on the microtubule. The step size histograms show clear peaks at 16 nm and around 8 nm (Fig. 4.16), showing that construct T324C also regularly takes substeps. The substep peak being comparatively broad will be discussed in a later section. Similarly to N356C, substeps become more rare for higher ATP concentrations.

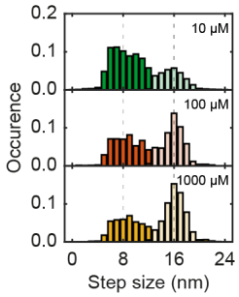

Fig 4.16: Step size histograms of T324C-ATTO 647N at 10 µM (green), 100 µM (orange) and 1 mM (yellow) ATP showing 8 nm substeps (darker filling; $N_{10\mu M}$=1160, $N_{100\mu M}$=568, N_{1mM}=892) and 16 nm regular steps (lighter filling; $N_{10\mu M}$=558, $N_{100\mu M}$=653, N_{1mM}=1299).

To determine, whether a plateau in the trace comes from the labeled head being in a bound or unbound state, we applied a Hidden Markov Model (HMM). The basic premise of the model was that a 16 nm step is about 50-times more likely to arise from a bound-to-bound (B→B) transition compared to an unbound-to-unbound (U→U) transition of the labeled head. The rational behind this is that during an apparent 16 nm step, the head moved in two 8 nm steps, but the resulting substep plateau was too short to be detected. While the B→B transition includes only one missed plateau duration τ_{1HB} of the labeled head, the U→U transition includes three (τ_{2HB} with labeled head in front, τ_{1HB} with unbound unlabeled head, τ_{2HB} with labeled head in rear), so missing the latter is much more unlikely. The HMM therefore predominantly assigned 16 nm steps to arise from a B→B transition, and with this determination was able to assign all other plateaus to a bound (B) or unbound (U) state of the labeled head.

Next, we plotted the histograms of the residence times of the labeled head in the B or U states, respectively, and fitted the distributions (Fig. 4.17). For the unbound state, we assumed a single time constant τ_{1HB}, whereas the bound state distribution of the labeled head was fitted with the sum of one τ_{1HB} and two τ_{2HB}. This was due to the reason mentioned before, that when the labeled head is bound, the unlabeled head is first in the rear of the 2HB state (with a duration of τ_{2HB}), then detaches into the 1HB state with the labeled head still microtubule-bound (with a duration of τ_{1HB}) and finally moves forward into the 2HB with the labeled head in the rear (with a duration of τ_{2HB}). The underlying premise for this fitting was that τ_{1HB} was the same for the labeled and unlabeled head.

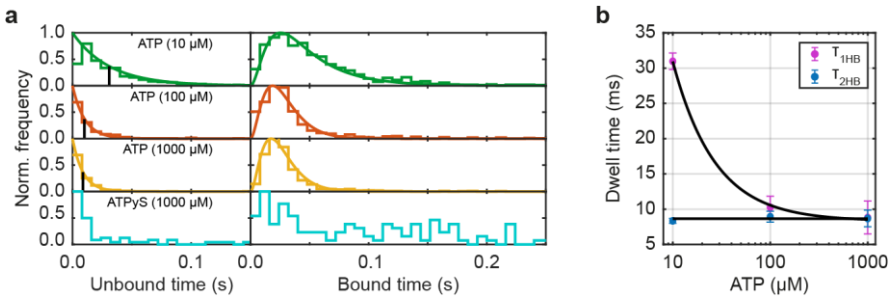

Figure 4.17: (**a**) Dwell time histograms of T324C-ATTO 647N at 10 µM (green), 100 µM (orange) and 1 mM (yellow) ATP and at 1 mM APTγS (cyan) with fits. (**b**) ATP-dependence of τ_{1HB} and τ_{2HB}. Error bars indicate the 64% confidence interval of the Michaelis-Menten kinetics fit.

The fits revealed, that the dwell time of the 1HB state is highly ATP-dependent, with τ_{1HB} increasing more than three-fold for a reduction in ATP concentration from 1 mM to 10 µM. In turn, the average dwell time of the 2HB state, τ_{2HB}, was constant at about 8.6 ms for all ATP concentrations. This clearly shows that kinesin binds ATP in the 1HB state with the unbound head between previous and next binding site on the microtubule.

This finding is very interesting, as it answers the controversial question in which state ATP binds to kinesin. One hypothesis in the field aimed to reconcile the contradicting findings of iSCAT and total internal reflection dark-field microscopy by assuming the existence of a third state between 2HB and 1HB, where the rear head is detached from but still associated with the microtubule, which was termed as 'unbound-undisplaced state'. The assumption is that ATP binds in this state, but depending on the labeling position, the bead appears either to be in-between or on the binding site due to the heads rotational flexibility. This hypothesis can be ruled out using our MINFLUX data, as we used an ~1 nm small label with an up to ~1 nm short linker and observed the unbound head to be significantly displaced from its previous binding site (about 8 nm) when ATP binds to kinesin.

4.5.3 ATP is hydrolyzed in two-head-bound (2HB) state

To also determine the state, in which ATP is hydrolyzed, we recorded traces of T324C-ATTO 647N with 1 mM adenosine-5'-(γ-thio)-triphosphate (ATPγS), a slowly hydrolysable ATP analogue. The velocity of kinesins was drastically lower (median velocity: ~43 nm/s), but the average duration of the

unbound state, determined with HMM analysis of the traces, was similar to that for experiments with 1 mM ATP that gave velocities of ~540 nm/s, as can be seen in the histogram in Fig. 4.17a. The distributions could not be fitted, but one can easily identify that dwell times in the 2HB state are much longer compared to the experiments with ATP. This can be well explained by hydrolysis taking place in the 2HB state, which significantly extends the state's duration with ATPγS.

I investigated this hypothesis further by comparing the run length of T324C-ATTO 647N for different ATP concentrations and for ATPγS determined by TIRF microscopy measurements. For this, I generated kymographs using the KymographBuilder in Fiji by plotting the fluorescent signal along the length of a microtubule over time. I determined the run lengths from the kymographs of multiple microtubules, which gave the average run lengths shown in Fig. 4.18. The data show that for the low ATP concentration of 1 µM, average run length is significantly shorter compared to for the 1 mM ATP concentration. This indicates, that the ATP-waiting state, which we found to be the 1HB state, seems to be the state most vulnerable to detachment of the motor from the microtubule, which shortens its run length, a finding in agreement with the kinesin literature[43]. The run lengths for ATPγS in turn did not decrease significantly, despite resulting in a similar kinesin velocity as 1 µM ATP. This hints towards hydrolysis not taking place in kinesin's 1HB state that is most vulnerable to detachment, as strongly increasing its duration with the slowly hydrolyzing ATPγS would be expected to drastically reduce run length. The small reduction can potentially be explained by a higher bleaching probability for the experiments with lower motor velocity despite the laser power in the focal plane after the objective being reduced (300 µW for 1 mM ATP and 10 µW for 1 µM ATP and 1 mM ATPγS).

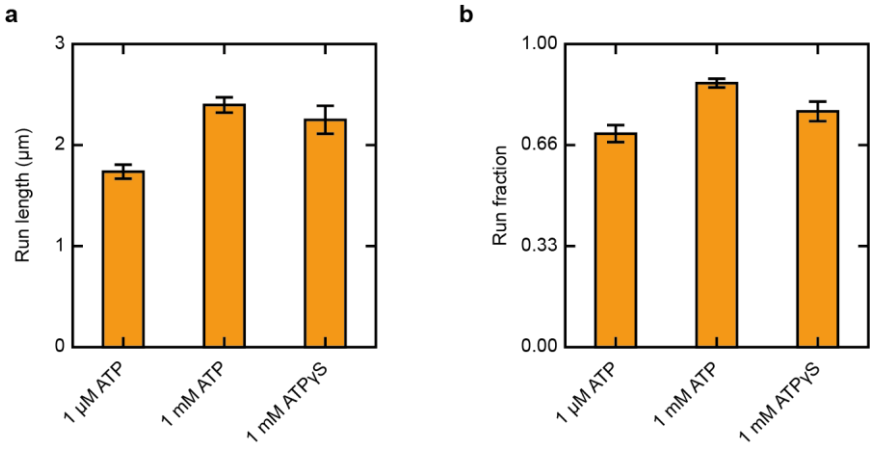

Figure 4.18: (**a**) Mean run length and (**b**) mean run fraction (run length divided by distance between starting point and plus end of microtubule) of T324C-ATTO 647N determined by kympgraph analysis of TIRF measurements ($N_{ATP,1\mu M}$=71, $N_{ATP,1mM}$=141, $N_{ATP\gamma S,1mM}$=57). Error bars represent the standard error of the mean.

Taken together, the ATPγS experiments rule out the 1HB state to hydrolyze ATP and instead show that a lower hydrolysis rate only increases the duration of the 2HB state. As the run length of kinesins in experiments with 1 µM ATP is significantly shorter than when 1 mM ATPγS is used, although the

motor velocity is similar, we concluded that ATP hydrolysis takes place when both heads are microtubule-bound (2HB). These findings allow the creation of a detailed mechanochemical cycle in a later section.

4.5.4 Reconstructing the 3D orientation of the unbound head

As we had directly observed the unbound state of the kinesin head during a substep, I envisioned determining its three-dimensional (3D) orientation in space by determining the displacement of two further amino acid positions on the head in its unbound state. To track the movement of the front of the head, I decided to use the commonly used construct E215C, where the solvent-exposed cysteine is located at the C-terminal end of the β6-sheet. For tracking of the head's rear, I designed construct K28C using site-directed mutagenesis by mutating the solvent-exposed amino acid at position 28 to a cysteine. By combining measurements of all three head-labeled constructs, unambiguous determining of the reorientation of the head should be possible by separately tracking the right center (T324C), front (E215C) and rear (K28C). The positions are referenced for microtubule-bound heads with respect to the walking direction and with the microtubule center defined as down. For this, I labeled the constructs with ATTO 647N-maleimide to give a low DOL (determined by ESI and UV-Vis spectroscopy as shown in Fig. A4.1).

4.5.4.1 On-axis displacement

Surprisingly, analysis of the E215C-ATTO 647N traces gave a comparably low fraction of substep pairs (B→U and U→B) that did not differ strongly between the ATP concentrations 10 µM, 100 µM and 1 mM, always amounting to ~10% (Fig. 4.19a).

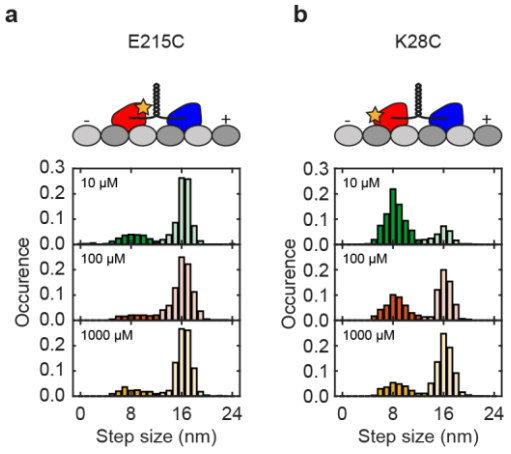

Figure 4.19: (**a**) Illustration of E215C-ATTO 647N labeled in the front of the head and step size histograms for ATP concentrations of 10 µM, 100 µM and 1 mM featuring 8 nm substeps (darker filling; $N_{10\mu M}$=216, $N_{100\mu M}$=65, N_{1mM}=81) and 16 nm regular steps (lighter filling; $N_{10\mu M}$=728, $N_{100\mu M}$=380, N_{1mM}=414). (**b**) Illustration of K28C-ATTO 647N labeled in the rear of the head and step size histograms for ATP concentrations of 10 µM, 100 µM and 1 mM featuring 8 nm substeps (darker filling; $N_{10\mu M}$=601, $N_{100\mu M}$=130, N_{1mM}=204) and 16 nm regular steps (lighter filling; $N_{10\mu M}$=186, $N_{100\mu M}$=176, N_{1mM}=601).

In comparison with T324C-ATTO 647N, the fraction of substep pairs (~50% for 10 µM ATP) was significantly smaller and the duration of the unbound state, as assigned by HMM analysis, was much shorter with >65% of fitted substep plateaus having a dwell time shorter than 8 ms (Fig. 4.20). For K28C-ATTO 647N however (Fig. 4.19b), the fraction of substep pairs (~60% for 10 µM ATP) was similar to that of T324C-ATTO 647N and the substep plateaus had a similar dwell time distribution with <15% of the substep plateaus having a duration shorter than 8 ms (Fig. 4.20).

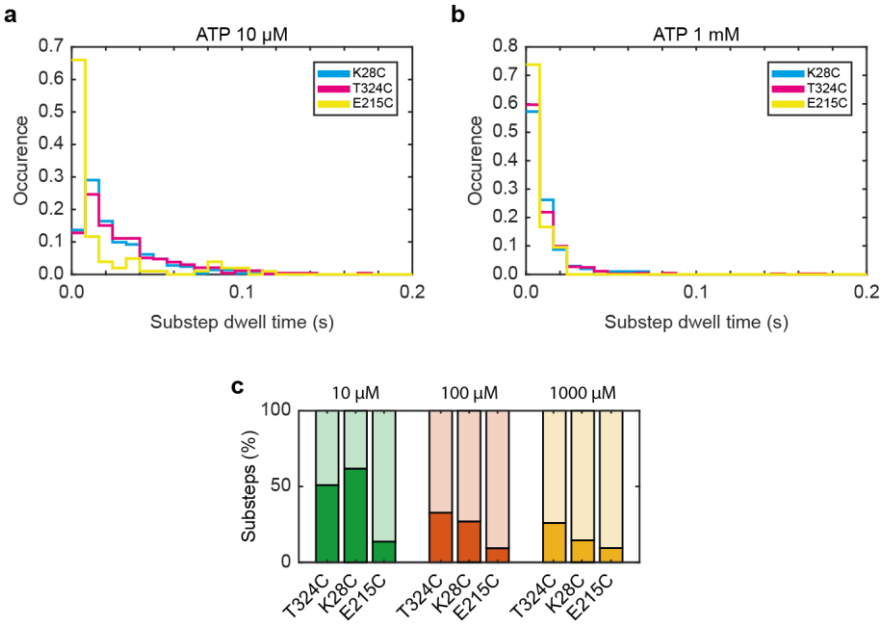

Figure 4.20: Substep dwell time histograms for (**a**) 10 µM ATP and (**b**) 1 mM ATP showing a much larger fraction of short (<8 ms) fitted substeps for E215C-ATTO 647N compared to K28C-ATTO 647N and T324C-ATTO 647N, respectively. (**c**) Fraction of detected substeps at 10 µM (green), 100 µM (orange) and 1 mM (yellow) ATP.

This comparison suggest, that the unbound state data of E215C-ATTO 647N, identified with the step-fit function and assigned with the HMM analysis, do not represent real substeps of amino acid position 215 (aa215) but are most likely artefacts from the noise of the position data, where short artificial substeps were fitted into real regular steps, or from variability of the biological system. For these findings, two explanations are possible. It could be that the labeling at aa215 prevents the labeled head from entering a detectable unbound state due to altered protein-protein interactions or steric hinderance. However, as the 1HB state of a construct fluorescently labeled at aa215 has been observed with FRET, this explanation is rather unlikely.

Instead, I advanced the illustration that when the head enters the unbound state, it rotates around its front in a way that aa215 remains (nearly) undisplaced whilst the labeled positions of K28C-ATTO 647N and T324C-ATTO 647N move significantly along the longitudinal microtubule axis. A closer inspection of the step size histogram of K28C-ATTO 647N shows a clear peak at ~8 nm, which is more narrow than that for T324C-ATTO 647N. Plotting the 2D histograms of consecutive step

sizes revealed a narrow distribution of consecutive regular step sizes (16 nm→16 nm) for both constructs (Fig. 4.21).

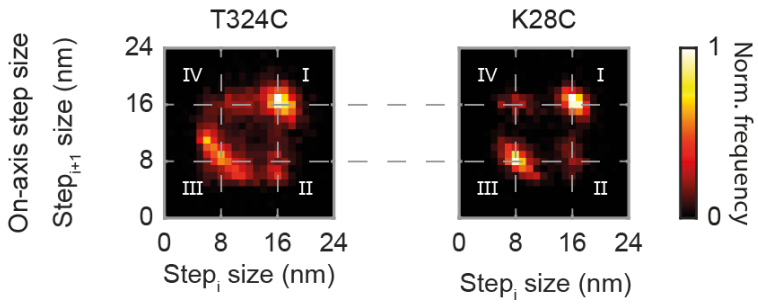

Figure 4.21: 2D histograms of consecutive step sizes for T324C-ATTO 647N and K28C-ATTO 647N.

But whereas the distribution of consecutive substeps of aa28 was also very narrow, substeps of aa324 were spread more broadly with the sum of consecutive substeps still amounting to ~16 nm. By splitting up the substep peak in the stepsize histogram into substeps entering or exiting the unbound state, respectively, one can clearly observe aa324 being displaced by ~6 nm when the labeled head rotates into the unbound state (Fig. 4.22). The narrow distribution of K28C-ATTO 647N substep sizes suggests that both substeps entering and exiting the unbound state have the same size of ~8 nm.

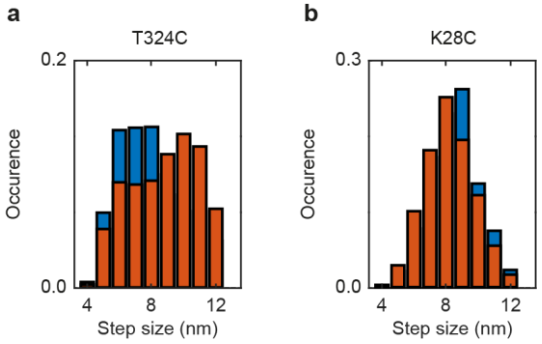

Figure 4.22: Step size histograms of (**a**) T324C-ATTO 647N and (**b**) K28C-ATTO 647N of transitions from bound state into unbound state (blue) and for transitions from unbound state into bound state (orange). For T324C-ATTO 647N, steps into unbound state peak at about 6 nm, for K28C-ATTO 647N, steps into and out of the unbound state peak at about 8 nm.

4.5.4.2 Off-axis displacement

Next, we analyzed the off-axis displacement of the traces. The previously mentioned scattering-based methods have contradictingly reported rightward and non-existent off-axis displacement of the labeled head when entering the unbound state, respectively, and due to the large bead size could not measure it [44, 45]. For construct T324C-ATTO 647N, off-axis displacement of the labeled head when unbound was small (<2 nm), but for construct K28C-ATTO 647N, significant sideward displacements of up to ~5 nm were measured (Fig. 4.23).

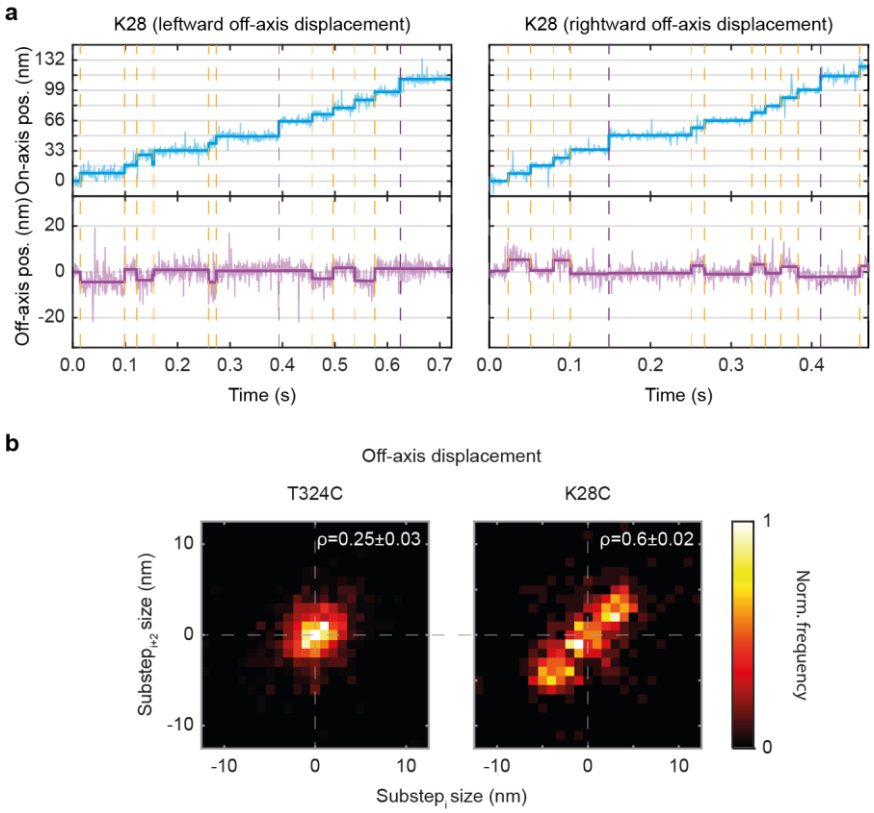

Figure 4.23: (**a**) Exemplary traces with apparent leftward off-axis displacement (left) and apparent rightward off-axis displacement (right) of the labeled unbound head of K28C-ATTO 647N. (**b**) 2D histograms of the off-axis displacement of successive substeps, indicating, that for K28C-ATTO 647N, off-axis displacement of the first substep is reversed by the next substep. For T324C-ATTO 647N, off-axis displacements are small (<2 nm).

Off-axis displacements were rightward, near-zero and leftward, but were consistent in magnitude and direction within a trace. Correlation analysis gave a high Pearson correlation coefficient (ρ=0.60±0.02), which indicates a highly consistent and defined orientation of the unbound head. I realized, that the different magnitudes and directions might arise from the fact that we measured with two-dimensional MINFLUX tracking on three-dimensional microtubules, with all off-axis displacements on different protofilaments being projected onto the imaging plane. This is illustrated in Fig. 4.24 for three cases, namely rightward, upward and leftward displacement of aa28 during the unbound state, showing that for upward displacement, significant off-axis displacement would be expected for the protofilaments on the side.

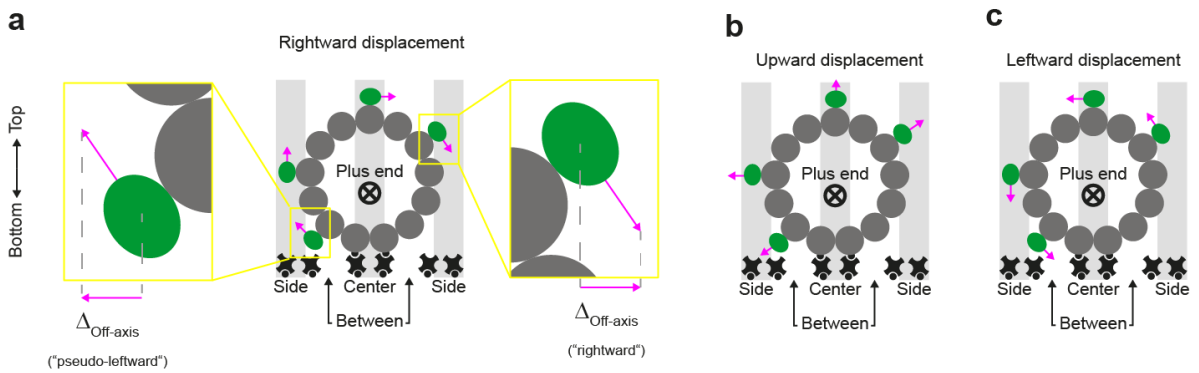

Figure 4.24: Illustration of off-axis displacements for scenarios of (**a**) rightward, (**b**) upward and (**c**) leftward displacement of the unbound head with respect to the walking direction and with the microtubule surface referenced as bottom. For sideward displacement of the unbound head, measurable off-axis displacement is maximal on the microtubule center and zero at the microtubule side. For upward displacement of the unbound head, measurable off-axis displacement is zero on the microtubule center and maximal at the microtubule side. Due to the 3D-structure of the microtubule, off-axis directions can be inversed between the microtubule top and bottom.

If the head moved sidewards into the unbound state with respect to the protofilament's outward surface and the walking direction, measured off-axis displacement would be maximal for kinesins on the center protofilaments and minimal for those on the side. I therefore initiated measurements on one position of an actively stabilized microtubule with the motivation to visualize traces on protofilaments of different categories ('center', 'side', 'between') and evaluate, if off-axis displacement was maximal for 'center' or 'side' protofilaments.

4.5.4.3 Unbound head rotates into rightward-displaced state during substep

I prepared the kinesin motility assay on ozone-cleaned coverslips that had an aluminium grating (~3 nm thin) imprinted on their objective-lens-facing side. This grating was continuously imaged using infra-red laser beams and a CMOS camera and any drift was actively corrected for. As a first test of visualizing the different protofilaments of a microtubule with the kinesin traces, we imaged K28C-ATTO 647N with 1 mM ATP, which gave parallel traces spaced by up to ~30 nm. As this distance is in good agreement with the sum of the outer diameter of a microtubule of ~25 nm and twice the ~2.5 nm distance between the microtubule surface and the position of aa28 when the labeled head is microtubule-bound (as inferred from PDB 3J8Y), the outer traces were assigned to kinesins walking on 'side' protofilaments, which allows for the referencing of 'center' and 'between' traces.

An illustration of traces revealing the protofilament structure of a microtubule is shown in Fig. 4.25.

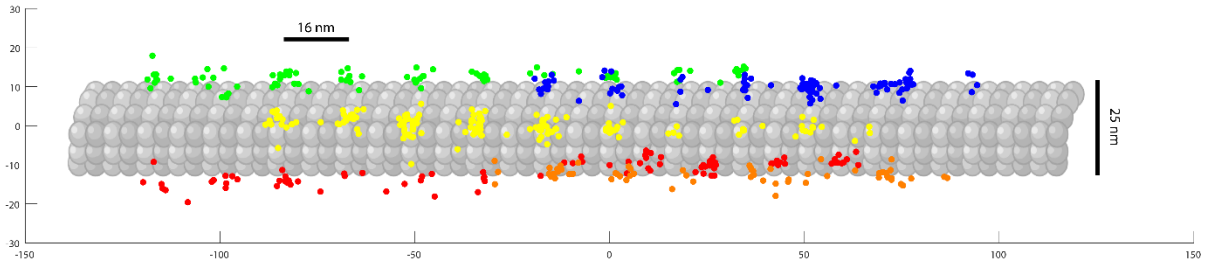

Figure 4.25: Illustration of binding sites of different protofilaments in an actively stabilized microtubule as visualized by K28C-ATTO 647N traces at 1 mM ATP.

With this proof of feasibility, we next measured K28C-ATTO 647N with 10 µM ATP to increase chances of observing 1HB states. We successfully measured trace sets on 19 different microtubules with a spacing of the outermost traces of ~30 nm. One exemplary trace set is shown in Fig. 4.26, which shows a highlighted 'center' trace with systematic, significant rightward displacement of aa28 in the labeled head's unbound state.

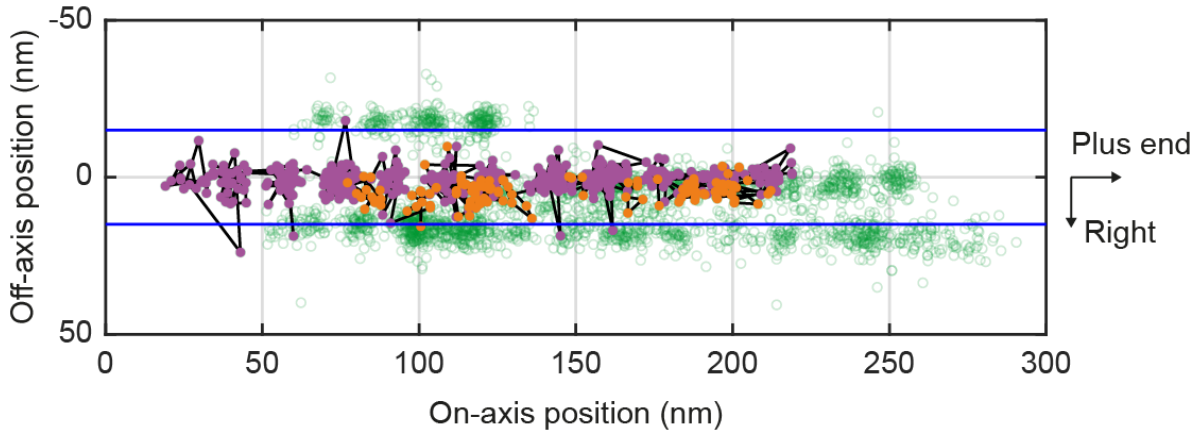

Figure 4.26: Scatter plot of four K28C-ATTO 647N traces on different protofilaments of an actively stabilized microtubule. The outer traces are used for referencing. The central trace (magenta) shows unbound states (orange) consistently displaced to the right.

The unbound states of the 'side' trace is near-zero, ruling out systematic upward displacement of the unbound head away from the outward protofilament surface. Next, I prompted the analysis of all trace sets by aligning their microtubule's central axis and overlaying the sets. Plotting the average off-axis displacement per unbound state over the lateral distance from the central axis gave Fig. 4.27, which confirms the findings that off-axis displacement is maximal for the 'center' protofilaments and decreases to near-zero for 'side' traces. Interestingly, sideward displacement of the unbound state is exclusively rightward for 'center' traces, for which only protofilaments on the top microtubule half should be accessible, because 'center' protofilaments on the bottom are most likely blocked by neutravidin and polymer used to immobilize the microtubule. Fitting of the data with an elliptic fit gave an average rightward displacement of ~4.6 nm.

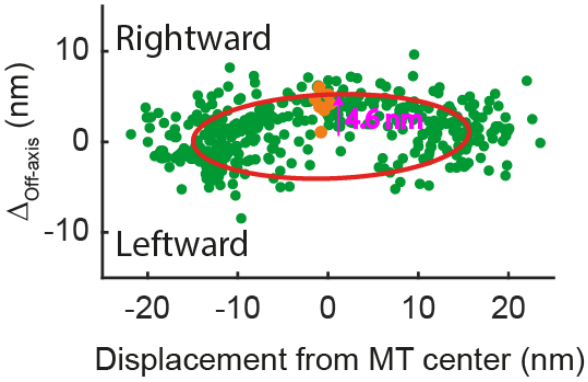

Figure 4.27: Off-axis displacement plotted against their respective displacement from the microtubule center. Off-axis displacement is mainly rightward and maximal in the microtubule center and near-zero at the microtubule sides. Rare leftward off-axis displacement probably results from kinesins walking on the microtubule bottom, but not in the bottom center, as it is likely blocked by immobilization to NVD and PLL-bt.

The leftward off-axis displacement of a few 'between' traces can be explained by kinesins walking on protofilaments on the down half of the microtubule. Due to simple geometric reasons, sideward displacement to the right (in walking direction with outward protofilament surface as down) appears as leftward displacement in the 2D measurement. By combining the exclusively rightward displacement on 'center' protofilaments and the near-zero off-axis displacement on 'side' protofilaments, we concluded that aa28 is moved ~4.6 nm to its right (with the microtubule center being downward and the walking direction forward) when the head is entering the unbound state.

By combining the on-axis substep sizes and the associated off-axis displacements of the three investigated amino acid positions, I derived an approximate average 3D orientation of the unbound kinesin head during the walking of kinesin (Fig. 4.28). Although approximate estimations of the unbound head orientation have already been made by FRET measurements, our recreation of the unbound head's orientation is less ambiguous, as it uses absolute displacements on the nanometer scale rather than relative distances determined by FRET.

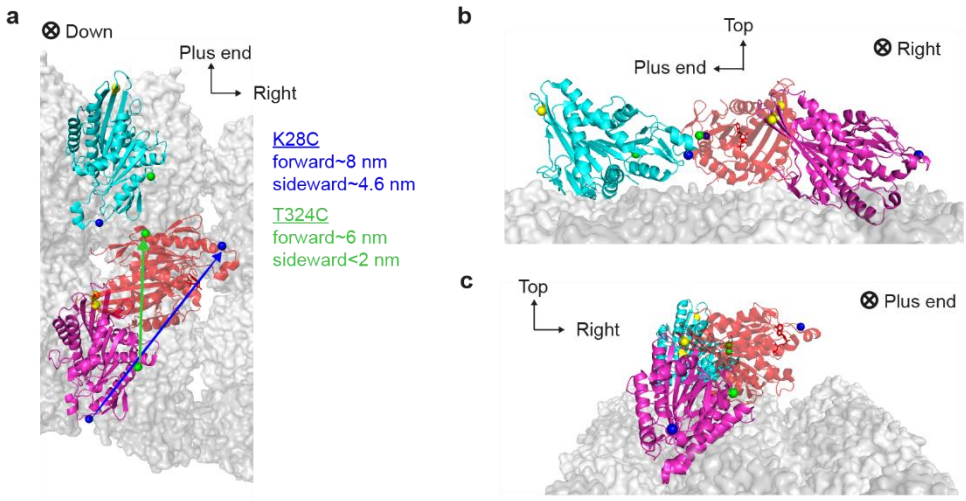

Figure 4.28: Reconstructed 3D orientation of the unbound state of the trailing head (red; PDB: 1MKJ) on the microtubule (alpha-tubulin in dark grey, beta-tubulin in light grey, PDB: 6DPU) with arrows displaying the respective displacement of the labeled amino acids. For reference, the microtubule-bound trailing head (magenta; PDB: 3J8Y) and the microtubule-bound leading head (cyan; PDB: 4ATX) are shown. Perspectives are (**a**) from the top, (**b**) from the left and (**c**) from the rear.

4.5.5 Observation of slip states

Closer inspection of the traces of K28C-ATTO 647N and T324C-ATTO 647N showed a rare occurrence of an uneven number of 8 nm substeps between 16 nm regular steps. These single substeps are surprising, as they indicate that the heads left their usually strict periodic pattern between binding sites spaced by two tubulin dimers (~16 nm). One explanation would be that kinesin switched protofilaments with the unbound head re-attaching next to the bound head. If the latter detaches, its next on-axis step will be ~8 nm in-between 16 nm steps. At least for traces on 'center' protofilaments, a simultaneous off-axis displacement would be expected for this protofilament switch, but as it was not observed, I ruled out this hypothesis.

As an alternative explanation, I brought forward a slip state, in which both kinesin heads detach from the microtubule, before reengaging after a short time. This state has been hypothesized in the optical trap paper that used germanium nanospheres, but only indirectly on the basis that when kinesin detaches from the microtubule at too high restoring forces, it seems to still interact with the binding sites on the microtubules when being retracted backwards along the microtubule. In our measurements however, we observed this phenomenon within stepping traces (see Fig. 4.29).

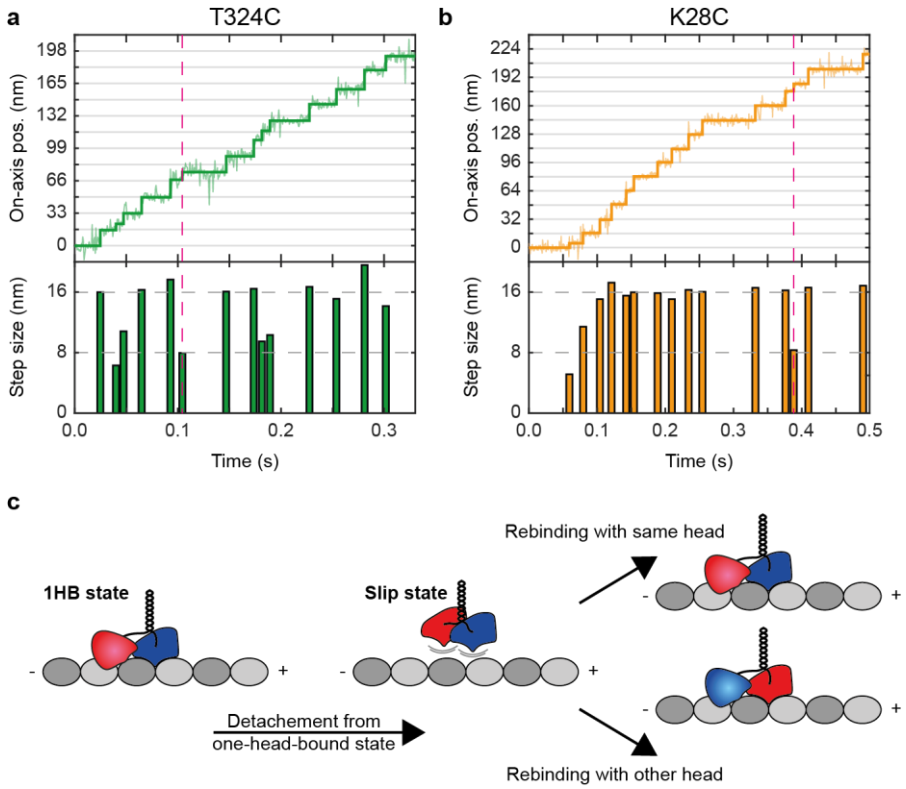

Figure 4.29: Exemplary traces of (**a**) T324C-ATTO 647N and (**b**) K28C-ATTO 647N with unpaired 8 nm steps (highlighted by magenta line) in-between regular 16 nm steps. (**c**) Illustration of slip state resulting from kinesin in the 1HB state detaching from and reattaching to the microtubule.

The HMM analysis also assigned a B→B transition for up to 2% of the steps, which can be explained by both kinesin heads detaching, after which they can either re-attach to their previous binding sites, resulting in a regular trace, or switch their respective positions. The latter would disturb the regularity of the trace by inserting an unpaired substep. As many kinesin-related diseases are thought to arise from premature detachment of the microtubule, direct observation of this rescue after motor detachment could be highly interesting for the development of therapies for those diseases.

4.5.6 Detailed mechanochemical cycle of kinesin-1

By combining the plethora of our results and only few reported observations from the literature, I was able to refine the mechanochemical cycle of kinesin-1 and to add information about the orientation of heads and stalk (Fig. 4.30). When kinesin is in its 2HB state, hydrolysis of ATP in the trailing head takes place and phosphate (P_i) is released form the catalytic center, causing the head to detach from the microtubule[49]. The trailing head rotates, roughly around its front, into a rightward-displaced unbound state. Upon binding of ATP to the nucleotide-free (apo state) microtubule-bound leading head[50], its neck linker probably docks to it[51, 52], moving the unbound head forward to its next binding site. The full step is completed by the (initially) trailing head reattaching to the microtubule with a total on-axis displacement of 16 nm and probably simultaneously releasing adenosine-5'-diphosphate (ADP). The second half-cycle can now commence by ATP hydrolysis in the new trailing head.

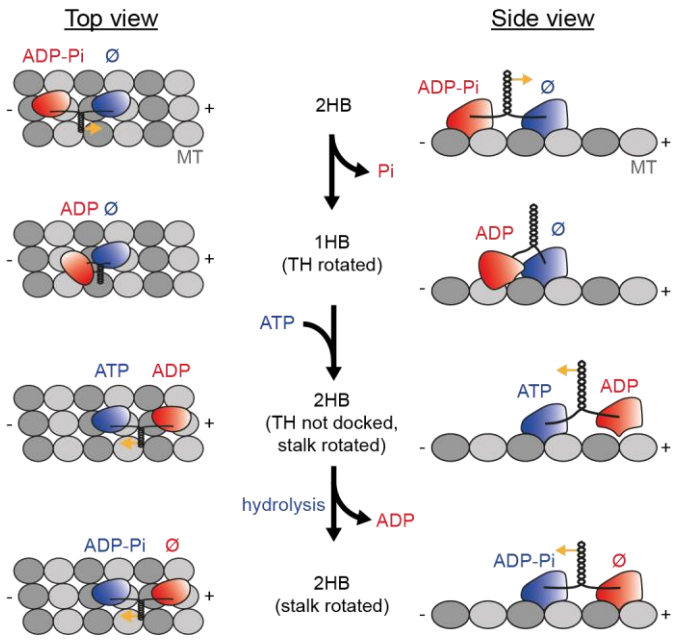

Figure 4.30: Mechanochemical cycle during semi-cycle (8 nm center-of-mass displacement) of kinesin walking on microtubules. The trailing head (TH, red) releases phosphate (P_i), detaches from the microtubuleand rotates around its front into a rightward-displaced unbound state. Upon ATP binding to the leading head (LH, blue) in the apo state (⌀), the neck linker presumably docks to the LH, moving the TH forward to its next binding site. Finally, ATP hydrolyzes in the LH and the TH binds to the microtubule, releasing ADP, completing the semi-cycle. During the semi-cycle, the stalk is rotated significantly (probably by ~180°).

To answer one further controversy whether kinesin-1 has a symmetric or asymmetric hand-over-hand walking mechanism, I combined the reconstruction of the unbound state and the stalk rotation. For an asymmetric mechanism, the side, on which the trailing head passes the leading head, should switch after every half-cycle, meaning that half of the traces show leftward and the other half would show rightward displacement of the unbound head. Within the framework of an asymmetric mechanism, the unbound head can theoretically always be displaced to the right and due to a built-up torsion in the coiled-coil of the stalk during every second step pass the leading head on its left side to resolve the tension. However, the observed ~180° rotation of the stalk most likely results from and resolves the built-up tension. This indicates, that the trailing head always passes the leading head on the right side, which builds up tension in the coiled-coil that is resolved by the stalk rotation half-way around its longitudinal axis after a full step. Hence, I deduced that kinesin-1 most likely walks with a symmetric hand-over-hand mechanism.

Conclusion

In this chapter, I demonstrated how by using MINFLUX, resolving steps and substeps of kinesin-1 is possible with an ~1 nm small fluorophore. For allowing high-performance tracking, I optimized the *in vitro* sample conditions by achieving a suitable degree of labeling and ruling out detrimental effects of the labeling of motors and microtubules or their handling on the activity. Furthermore, I reduced fluorescent background by developing the PLL-bt based kinesin motility assay and by efficiently blocking the surface with BSA-bt. With these conditions and a novel interferometric MINFLUX

approach, we resolved regular steps (~8 nm) and substeps (~4 nm) of the kinesin-1 stalk using only ~100 photons per localization within less than a millisecond to give a spatial localization precision of 1.8 nm. After observing a systematic alternation of step sizes that was resolved by reinstating labeling symmetry with the addition of a second fluorophore, I concluded the stalk to rotate by ~180° during a step.

By tracking kinesin-1 constructs labeled at one of their heads, we were able to distinguish between the one-head-bound state and the two-head-bound state. By measuring at up to a physiological ATP concentration of 1 mM, with an average motor velocity of ~540 nm/s, we determined that kinesin-1 bound ATP when in its 1HB state. By using the slow-hydrolyzing ATP analogue ATPγS, we found that hydrolysis takes place when kinesin-1 is in its 2HB state.

Tracking different regions on the motor's head showed, that it rotates around its front into the rightward-displaced unbound state. Combining this finding with the stalk rotation leads to the conclusion that kinesin-1 has a symmetric hand-over-hand walking mechanism.

We also identified a slip state in the traces, where the motor most likely momentarily detaches from the microtubule before rebinding, which could be of interest for studying diseases linked to premature kinesin detachment from the microtubule.

Finally, combining these findings allowed for the creation of a coherent mechanochemical cycle that answers several controversial questions in the field.

Publication and contributions

The results of chapter 4 have been published as follows:

MINFLUX dissects the unimpeded walking of kinesin-1

Jan O. Wolff*, Lukas Scheiderer*, Tobias Engelhardt, Johann Engelhardt, Jessica Matthias, Stefan W. Hell

*Co-First authors

bioRxiv 2022.07.25.501426; doi: https://doi.org/10.1101/2022.07.25.501426

Submitted to 'Science' (currently in first revision).

Contributions for chapter 4:

MINFLUX microscope design: Dr. Johann Engelhardt, Tobias Engelhardt, Jan Otto Wolff; building of MINFLUX microscope: Tobias Engelhardt and Jan Otto Wolff; MINFLUX measurements: mainly Jan Otto Wolff; Matlab evaluation script: Jan Otto Wolff.

Chapter 5: Kinesin tracking with MINSTED

Aim

This chapter evaluates and establishes the novel nanoscopy technique MINSTED for tracking. It has been reported to achieve subnanometer localization precision with <1000 detected photons and hence would be a great technique for tracking of, for instance, fast biological processes like protein dynamics. As MINSTED is also very robust to fluorescence background, it seems to be a promising candidate for live-cell tracking on the nanoscale. I was therefore motivated to test the tracking suitability of MINSTED on the kinesin-1 assay and compare its performance to that of MINFLUX.

Overview

The nanoscopy technique MINSTED creates a very narrow excitation beam using the STED concept to deplete fluorophores in the periphery of a pulsed excitation beam from the fluorescent state with a co-aligned pulsed doughnut-shaped depletion beam. Fluorophores are localized with the flank rather than with the beam maximum, as the information content of emitted fluorescent photons is higher when caused by the beam edges. The narrow excitation beam is continuously circled around the fluorophore. Its circle radius is reduced and simultaneously, its FWHM get decreased by increased STED power, and the circle center is shifted in the direction of the last detected photon. Hence, this principle can also be applied to a fluorescent emitter in motion, as its assumed position is updated with every detected photon, which in principle offers sub-millisecond temporal resolution.

A potential limit could be bleaching due to high STED powers necessary to achieve a narrow excitation beam and thereby best spatial precision, although the fluorophore ideally never experiences the high power of the depletion beam maximum. Fast bleaching would shorten the recorded traces, making investigations of, for instance, protein dynamics difficult. Due to it offering a promising spatial resolution with a high photon efficiency, evaluating the performance of MINSTED tracking with the alleged gold standard system for protein tracking, kinesin-1, promises to be of great benefit for the single molecule tracking field.

Results and Discussion

To test the tracking capabilities of MINSTED, I employed the kinesin-1 assay based on PLL-bt with neutravidin, biotinylated and fluorescently labeled, highly pure microtubules (bt-MT-AF488) and BSA-bt for blocking, as described in the previous chapter. It immobilized the microtubules strongly and specifically and allowed for long-range walking of the motor, as shown by TIRF and MINFLUX measurements. The final measuring buffer consisted of ATP, 1 mM DTT, 20 µM Taxol, 10 µg/ml BSA-bt, 1 mM MV, 1 mM AA in PM15 buffer. For oxygen removal, I used an oxygen scavenger system (OSS) consisting of pyranose oxidase, catalase and glucose (5% (w/v)) for an easier sample

preparation and because MINSTED should be less affected by its fluorescent background than MINFLUX. Successful oxygen reduction was confirmed by fluorophores on immobilized kinesins bleaching much later in MINSTED measurements compared to those in a buffer without the OSS added. TIRF measurements of the samples showed high kinesin activity.

For a MINSTED tracking experiment, the region of a microtubule was continually scanned with a confocal beam until the fluorescent signal crossed a set threshold and the MINSTED tracking routine was triggered. The fluorophore was then tracked by the narrow effective excitation beam encircling it and the circle center position being updated after each detected photon. I identified traces of stepping kinesins by rejecting events below a certain duration, distance and aspect ratio. More details on the tracking procedure and filtering are provided in the methods section (appendix).

5.1 Tracking ATTO 647N yields long traces

5.1.1 E215C-ATTO 647N

In a MINSTED setup with a 775 nm STED laser and a 640 nm excitation laser, we successfully recorded many traces of constructs E215C-ATTO 647N, T324C-ATTO 647N and K28C-ATTO 647N with lengths up to about 700 nm traveled within a duration of more than a second. This clearly rejects the concern that MINSTED inevitably causes fast bleaching of the fluorophore, which would result in short tracks. The longest traces were substantially longer than those from MINFLUX measurements, where tracking was limited to how far the excitation minimum could be moved by scanning the phase of the beams as the galvanometer scanner was not moved during that tracking procedure. The exemplary MINSTED trace of E215C-ATTO 647N with 1 mM ATP (Fig. 5.1) shows clearly resolved steps of mostly about 16 nm.

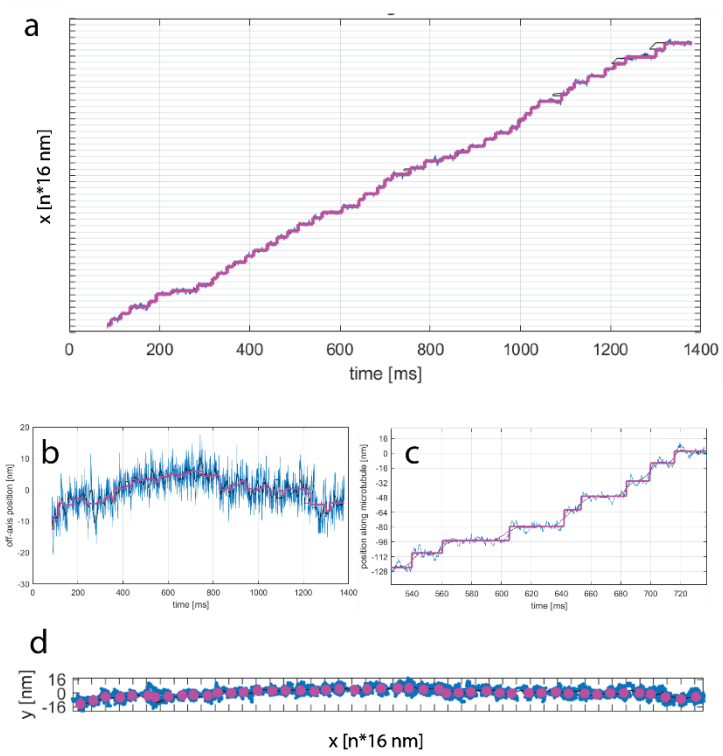

Figure 5.1: Exemplary MINSTED trace of E215C-ATTO 647N with 1 mM ATP walking a total of ~700 nm. (**a**) On-axis displacement over time; vertical ticks are spaced by 16 nm. (**b**) Off-axis displacement over time. (**c**) Zoom-in of on-axis displacement over time displaying clear 16 nm steps. (**d**) 2D-plot; ticks are spaced by 16 nm.

With a median number of 857 photons per trace at a median count rate of about 6.5 kHz, MINSTED achieved a median spatial precision of about 5 nm with a median time resolution of less than a millisecond, as determined from a fit of the step response data (Fig. A5.1). The step size histogram of all recorded traces in Fig. 5.2 shows a clear dominance of step sizes of about 16 nm.

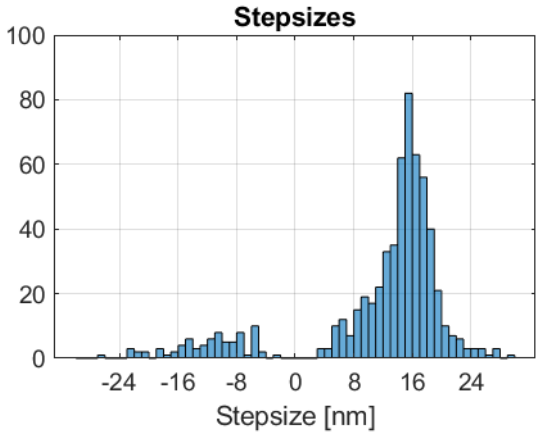

Figure 5.2: Stepsize histogram for E215C-ATTO 647N with 1 mM ATP.

Measuring at a decreased ATP concentration of 10 µM also gave a main peak in the step size histogram (Fig. A5.2) at about 16 nm, which is consistent with the finding in the previous chapter that the label at

amino acid 215 does not show substepping behaviour due to the rear head rotating around it into its rightward-displaced unbound state.

It also shows an increased fraction of backsteps with negative step sizes, which can be explained by the binding of ATP probably inducing neck linker docking, which moves the unbound head forward[51, 52]. With a higher average time in the more flexible neck-linker-undocked unbound state at lower ATP concentrations, the probability of the unbound head diffusing backwards to its previous binding site increases.

5.1.2 T324C-ATTO 647N and K28C-ATTO 647N: rightward-displaced unbound state and side-stepping

Out of the traces of K28C-ATTO 647N with 1 mM ATP, I identified a trace with a clear substep plateau that had a duration of about 50 ms and displayed a concurrent rightward off-axis displacement of about 5 nm (Fig. 5.3).

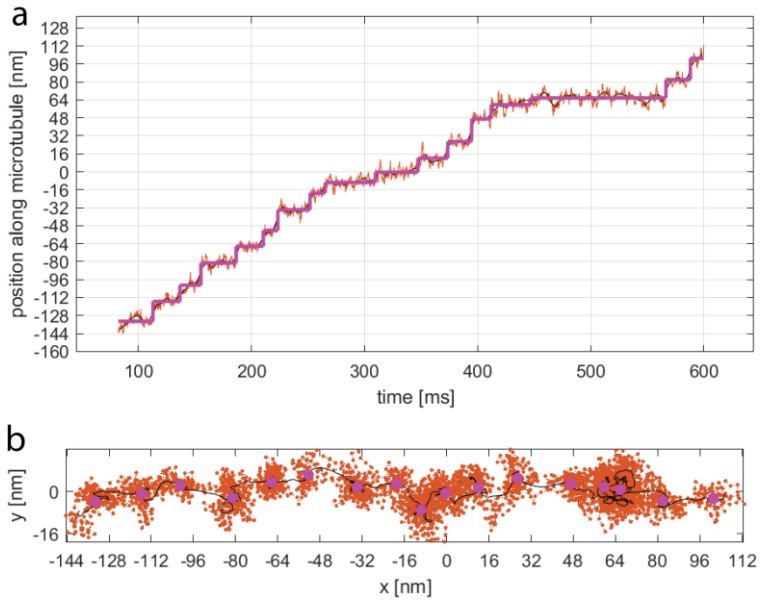

Figure 5.3: Exemplary MINSTED trace of K28C-ATTO 647N at 1 mM ATP. (**a**) On-axis displacement over time with rightward displacement of unbound state around 280 ms. (**b**) 2D-plot with rightward displacement of unbound state at about -8 nm.

This observation is in good agreement with the finding from the previous chapter that during a substep, amino acid 28 is displaced by up to 5 nm to the right. For T324C-ATTO 647N with 1 mM ATP, a trace is displayed during which the head was displaced rightward by about 6 nm for the duration of a presumable bound state after a fitted regular 16 nm step of the labeled head (Fig. 5.4a). After the next regular 16 nm step of the labeled head, its off-axis displacement returned to the initial level. As the protofilaments have a parallel spacing of about 6 nm (inferred from PDB 6DPU), the most probable explanation seems to be sidestepping, where the labeled head bound to a binding site on an adjacent

protofilament, but returned to the previous protofilament after the next full step of the unlabeled head (as illustrated in Fig. 5.4b).

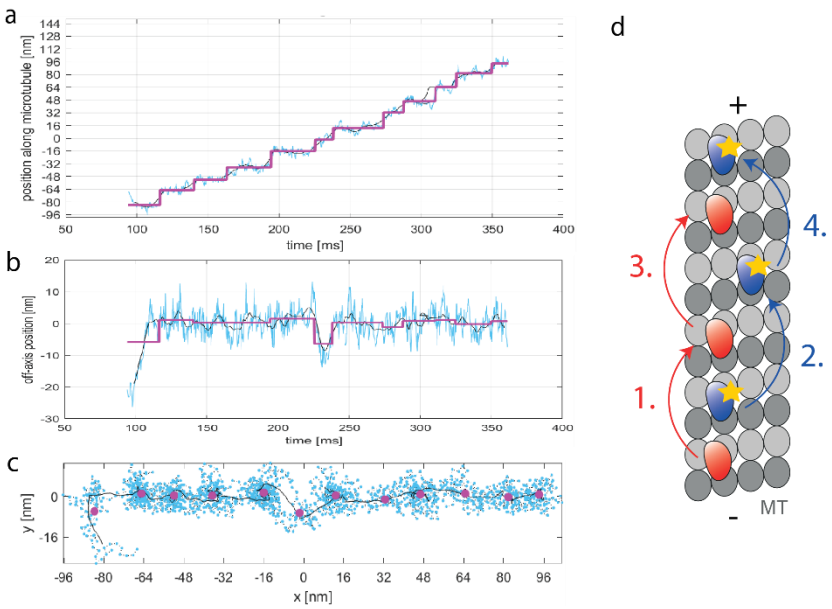

Figure 5.4: Exemplary MINSTED trace of T324C-ATTO 647N with 1 mM ATP. (**a**) On-axis displacement over time. (**b**) Off-axis displacement over time with sidestep at around t=225 ms. (**c**) 2D-plot with sidestep at about x=0 nm. (**d**) Illustration of sidestep to neighboring protofilament.

5.2 Tracking Cy3B yields increased precision

In the pursuit to improve the trace's spatial resolution, we employed a setup with a shorter laser wavelength of 560 nm for excitation and 636 nm for stimulated emission. For this purpose, I labeled the kinesin-1 constructs E215C, T324C and K28C with the bright and stable fluorophore Cy3B-maleimide for two hours at room temperature with the same respective stoichiometry used for the ATTO 647N-labeled constructs. After removal of unreacted fluorophores by size-exclusion chromatography, I determined the degrees of labeling to be low (<0.55 per kinesin-1 dimer) using UV-Vis spectroscopy. With TIRF measurements, I confirmed the activity and motility of E215C-Cy3B, T324C-Cy3B and K28C-Cy3B on microtubules in the measuring buffer.

5.2.1 E215C-Cy3B - Protofilament switching

With the Cy3B-labeled constructs, we achieved improved median spatial precisions between 3.1 nm and 3.6 nm within less than 1.7 ms at median count rates up to 11 kHz. Traces had a median duration about one third of that from constructs labeled with ATTO 647N. In Fig. 5.5, exemplary traces of E215C-Cy3B with 1 mM ATP are shown that show clearly resolved binding positions on the microtubule. Interestingly, the trace in Fig. 5.5b seems to feature a motor switching between protofilaments spaced by over 10 nm, which would indicate that the kinesin-1 protein completely detached from its previous protofilament and presumably diffused across the microtubule before

continuing its stepping on another protofilament. This observation is very interesting, as it displays how transport of cargo can be rescued, even after a motor detached from its track.

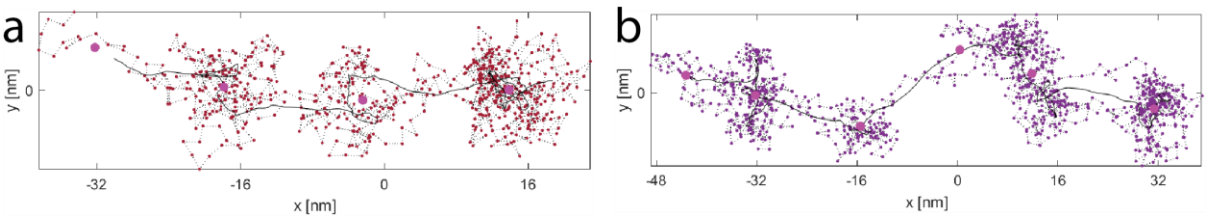

Figure 5.5: Exemplary MINSTED traces of E215C-Cy3B with 1 mM ATP. (**a**) 2D-plot with clear 16 nm spacing. (**b**) 2D-plot with protofilament switch.

The step size histogram of E215C-Cy3B with 1 mM ATP (Fig. A5.3) shows a main peak at around 16 nm and rarely occurring backsteps, which is consistent with the previous findings for E215C-ATTO 647N.

5.2.2 T324C-Cy3B

T324C-Cy3B with 1 mM ATP gave short traces with only a few steps (exemplary trace in Fig. A5.4). The step size histogram (Fig. A5.5) displays the occurrence of steps of between 8 nm and 16 nm, which agrees with the observation made with MINFLUX, that substeps can be detected for this construct.

5.2.3 K28C-Cy3B

5.2.3.1 Protofilament switching

The longest traces with Cy3B were recorded with K28C-Cy3B at 1 mM ATP. An exemplary trace (Fig. 5.6) displays clear regular 16 nm steps and an apparent lateral switch between protofilaments spaced by of over 10 nm. This finding substantiates the hypothesis that kinesin-1 sometimes detaches from the microtubule and resumes its transport on a different protofilament.

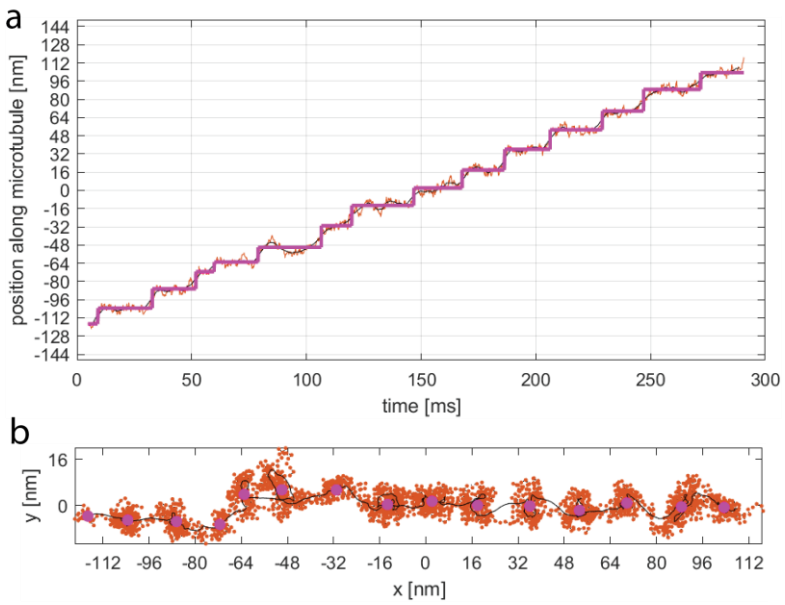

Figure 5.6: Exemplary MINSTED trace of K28C-Cy3B with 1 mM ATP. (**a**) On-axis displacement over time. (**b**) 2D-plot with protofilament stiwch at about x= -70 nm.

For 1 mM ATP, mainly 16 nm steps are determined for K28C-Cy3B, but also 8 nm substeps, as can be seen in the step size histogram, which agrees with the observation with MINFLUX that substeps can be resolved to construct K28C (Fig. A5.6).

To visualize the protofilaments of a microtubule, I initiated stabilized measurements of K28C-Cy3B at an ATP concentration of 1 mM. For the stabilization, I incubated oxygen plasma-cleaned coverslips with a solution of gold nanorods as fiducial markers. After blow-drying the coverslips, I built them into a flow-chamber with the nanorods on the inside and subsequently added the previously described assay components. Before the measurement, the fiducial markers were selected and locked for active stabilization by the piezo stage.

5.2.3.2 Microtubule visualization

A reconstruction of a microtubule from the traces of labeled kinesins is shown in Fig. 5.7. It clearly shows parallel tracks on different protofilaments. The median spatial precision of about 3.6 nm allows for the visualization of the binding sites of kinesin on the microtubule and thereby the periodic microtubule structure.

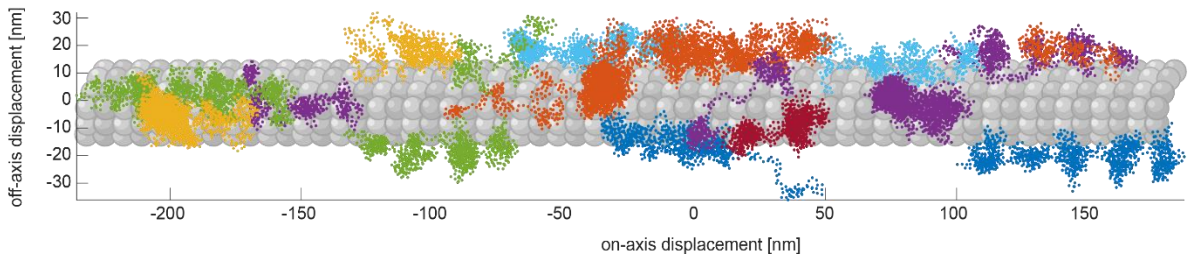

Figure 5.7: Visualization of protofilaments of stabilized microtubule with tracks of K28C-Cy3B at 1 mM ATP.

With this image, I envision directly visualizing the impact of roadblocks, like aggregates of tau protein that are deemed responsible for Alzheimer's disease, on the processivity of molecular motors, including kinesin-1[53, 54]. The capability of the motor to circumvent obstacles is still debated[55, 56]. With MINSTED of MINFLUX, roadblocks could be precisely localized and the behavior of motors encountering it, like detachment or the previously observed sidestepping, could be studied.

Conclusion

In this chapter, I demonstrated the first successful tracking experiments of kinesin-1 with MINSTED. For ATTO 647N-labeled constructs, the spatial precision was about 5 nm. We recorded traces that were up to about 700 nm long with steps clearly resolved. I found that the occurrence of 8 nm substeps for construct E215C-ATTO 647N is small even for a low ATP concentration of 10 µM, which complies with the observations from the previous MINFLUX experiments. Interestingly, the backstep fraction was higher for 10 µM ATP, probably because ATP triggers the neck linker to dock to the microtubule-bound head that moves the labeled unbound head forward. In individual traces, I observed rightward off-axis displacement of the unbound head, as described in the previous chapter, and presumable sidestepping to adjacent protofilaments.

By tracking kinesin-1 constructs labeled with Cy3B, the spatial precision was improved to ≤3.6 nm. Some traces featured protofilament switches, where the motor probably detached from the microtubule and resumed its stepping on a different protofilament, a rescue mechanism that could be interesting in the study of diseases caused by premature motor detachment. By tracking multiple kinesins on actively stabilized microtubules, I was able to visualize the binding sites of their different protofilaments, as had also been possible with MINFLUX. These methods could thus be useful in directly probing the interaction of molecular motors with roadblocks, which are prime suspects for causing various (neurodegenerative) diseases.

Contributions

Contributions for chapter 5:

Building MINSTED microscopes: Henrik von der Emde, Dr. Michael Weber; MINSTED measurements: mainly Henrik von der Emde, Dr. Michael Weber; Matlab evaluation script: Henrik von der Emde.

Conclusion and Outlook

In this thesis, I first developed polymer-based *in vitro* assays for the study of single molecules. They displayed specific immobilization of the targets and a reduced fluorescence background compared to established assays, which makes them the superior choice for future *in vitro* studies with the fluorescence nanoscopy technique MINFLUX.

I successfully applied them in the development of novel spontaneously blinking fluorophores, as they faithfully reproduce the blinking characteristics in cells. By performing a quantitative analysis of their blinking behavior, I found the spontaneous blinkers to have on-times of a few milliseconds per event and low duty cycles, making them suitable candidates for accelerated MINFLUX imaging. The analysis also showed a significant impact of the fluorophore conjugation, to either an antibody or a HaloTag protein, on the blinking characteristics, highlighting the importance to use a suitable *in vitro* assay for the future screening of fluorophores. Furthermore, I identified the commonalities between good blinkers, which will help in improving them further.

As they are live-cell compatible and do not require a blinking buffer, they are likely to propel the MINFLUX imaging field by strongly decreasing measurement times.

For establishing MINFLUX tracking as a method for the study of (protein) dynamics on the nanoscale, I created a specific and robust microtubule-immobilizing polymer-based *in vitro* assay to study the stepping mechanism of kinesin-1 with a spatio-temporal resolution of a few nanometers within <1 ms. By tracking a small fluorophore label on the motor, we concluded it to bind ATP in the one-head-bound state and hydrolyze it in the two-head-bound state, answering a controversial question in the field. We also reconstructed the three-dimensional structure of the unbound head during a substep and found it to be displaced rightward and rotated around its front. In conjunction with an observed rotation of the stalk, I concluded kinesin-1 to walk in a symmetric hand-over-hand fashion. Furthermore, I spotted kinesin-1 in a previously hypothesized slip state.

Thus, with the power of MINFLUX, I could dissect the mechanochemical cycle of kinesin-1 and capture the unbound state, answering details that could assist in the development of treatments for diseases caused by a malfunction of the motor.

I also evaluated the applicability of the novel MINSTED nanoscopy for single molecule tracking. Traces up to a length of 700 nm were successfully measured and steps clearly resolved with a median spatial precision of 3-5 nm and a down to sub-millisecond temporal resolution. I was able to confirm many findings from the MINFLUX experiments, but furthermore observed motors switching from one protofilament to another. Like the slip state, this detaching and rescue mechanism is highly interesting for investigating how kinesin-1 (prematurely) detaches from the microtubule.

As MINFLUX and MINSTED resolved the binding sites of protofilament tracks, future work could directly visualize the behavior of molecular motors when encountering an obstacle, which would be highly advantageous in the study of (neurodegenerative) diseases caused by blockades on the microtubules, like Alzheimer's disease.

In general, this thesis opens the door for the future investigation of various biological dynamic processes with MINFLUX and MINSTED. By requiring only a small fluorophore label, they are significantly less artefact-prone than established bead-tracking techniques while offering a competitive spatio-temporal resolution, so re-visiting (biological) systems previously investigated with established methods might lead to unexpected new findings. The performance of the nanoscopy tracking techniques can be enhanced further by synthesizing and using new fluorophores with higher photon emission rates and increased resistance to photobleaching.

Live-cell tracking has been shown to work with MINFLUX[20, 57]. Due to the robustness of MINSTED against fluorescent background, it would be a great tracking technique even in crowded enviromnents of living cells.

Another advantage of the fluorescence-based nanoscopy techniques is its capability of performing multi-color measurements, which would allow for simultaneously tracking different (protein) positions and determine their relative distances, challenging FRET as the most prominent nanoruler technique.

By pushing the development of MINFLUX and MINSTED further, following the intramolecular dynamics of proteins, for instance during their folding process, might one day be possible. However, as labeling arguably always (slightly) changes the behavior of the target, future innovations ideally make the necessity to label it directly obsolete.

References

1. Vale, R.D., T.S. Reese, and M.P. Sheetz, *Identification of a novel force-generating protein, kinesin, involved in microtubule-based motility.* Cell, 1985. **42**(1): p. 39-50.
2. Vale, R.D. and R.A. Milligan, *The way things move: Looking under the hood of molecular motor proteins.* Science, 2000. **288**(5463): p. 88-95.
3. Wang, Q., et al., *Amyloid beta-mediated KIF5A deficiency disrupts anterograde axonal mitochondrial movement.* Neurobiol Dis, 2019. **127**: p. 410-418.
4. Baron, D.M., et al., *ALS-associated KIF5A mutations abolish autoinhibition resulting in a toxic gain of function.* Cell Rep, 2022. **39**(1): p. 110598.
5. Michels, S., et al., *Mutations of KIF5C cause a neurodevelopmental disorder of infantile-onset epilepsy, absent language, and distinctive malformations of cortical development.* Am J Med Genet A, 2017. **173**(12): p. 3127-3131.
6. Yuen, E.Y., et al., *Disrupted GABAAR trafficking and synaptic inhibition in a mouse model of Huntington's disease.* Neurobiol Dis, 2012. **46**(2): p. 497-502.
7. Fichera, M., et al., *Evidence of kinesin heavy chain (KIF5A) involvement in pure hereditary spastic paraplegia.* Neurology, 2004. **63**(6): p. 1108-10.
8. Chandrasekaran, G., P. Tatrai, and F. Gergely, *Hitting the brakes: targeting microtubule motors in cancer.* Br J Cancer, 2015. **113**(5): p. 693-8.
9. Cross, R.A., *The kinetic mechanism of kinesin.* Trends in Biochemical Sciences, 2004. **29**(6): p. 301-309.
10. Coy, D.L., M. Wagenbach, and J. Howard, *Kinesin takes one 8-nm step for each ATP that it hydrolyzes.* Journal of Biological Chemistry, 1999. **274**(6): p. 3667-3671.
11. Schnitzer, M.J. and S.M. Block, *Kinesin hydrolyses one ATP per 8-nm step.* Nature, 1997. **388**(6640): p. 386-390.
12. Mori, T., R.D. Vale, and M. Tomishige, *How kinesin waits between steps.* Nature, 2007. **450**(7170): p. 750-U15.
13. Verbrugge, S., Z. Lansky, and E.J. Peterman, *Kinesin's step dissected with single-motor FRET.* Proc Natl Acad Sci U S A, 2009. **106**(42): p. 17741-6.
14. Mickolajczyk, K.J., et al., *Insights into Kinesin-1 Stepping from Simulations and Tracking of Gold Nanoparticle-Labeled Motors.* Biophysical Journal, 2019. **117**(2): p. 331-345.
15. Hasnain, S., M.L. Mugnai, and D. Thirumalai, *Effects of Gold Nanoparticles on the Stepping Trajectories of Kinesin.* Journal of Physical Chemistry B, 2021. **125**(37): p. 10432-10444.
16. Yildiz, A., et al., *Kinesin walks hand over hand.* Biophysical Journal, 2004. **86**(1): p. 527a-527a.
17. Toomre, D. and J. Bewersdorf, *A New Wave of Cellular Imaging.* Annual Review of Cell and Developmental Biology, Vol 26, 2010. **26**: p. 285-314.
18. Fernandez-Suarez, M. and A.Y. Ting, *Fluorescent probes for super-resolution imaging in living cells.* Nature Reviews Molecular Cell Biology, 2008. **9**(12): p. 929-943.
19. Schneider, J., et al., *Ultrafast, temporally stochastic STED nanoscopy of millisecond dynamics.* Nature Methods, 2015. **12**(9): p. 827-+.

20. Balzarotti, F., et al., *Nanometer resolution imaging and tracking of fluorescent molecules with minimal photon fluxes.* Science, 2017. **355**(6325): p. 606-612.

21. Schmidt, R., et al., *MINFLUX nanometer-scale 3D imaging and microsecond-range tracking on a common fluorescence microscope.* Nature Communications, 2021. **12**(1).

22. Eilers, Y., et al., *MINFLUX monitors rapid molecular jumps with superior spatiotemporal resolution.* Proceedings of the National Academy of Sciences of the United States of America, 2018. **115**(24): p. 6117-6122.

23. Gwosch, K.C., et al., *MINFLUX nanoscopy delivers 3D multicolor nanometer resolution in cells.* Nature Methods, 2020. **17**(2): p. 217-+.

24. Weber, M., et al., *MINSTED nanoscopy enters the Ångström localization range.* bioRxiv, 2022: p. 2022.03.18.484906.

25. Mathe, C., et al., *Structural Determinants for Protein adsorption/non-adsorption to Silica Surface.* Plos One, 2013. **8**(11).

26. Magyari, K., et al., *The anchoring of fibrinogen to a bioactive glass investigated by FT-IR spectroscopy.* Vibrational Spectroscopy, 2012. **62**: p. 172-179.

27. Gruian, C.M., et al., *Conformational Changes and Competitive Adsorption between Serum Albumin and Hemoglobin on Bioceramic Substrates.* Chemphyschem, 2017. **18**(6): p. 634-642.

28. Zheng, K., M. Kapp, and A.R. Boccaccini, *Protein interactions with bioactive glass surfaces: A review.* Applied Materials Today, 2019. **15**: p. 350-371.

29. Qin, M., et al., *Two methods for glass surface modification and their application in protein immobilization.* Colloids and Surfaces B-Biointerfaces, 2007. **60**(2): p. 243-249.

30. Holmberg, A., et al., *The biotin-streptavidin interaction can be reversibly broken using water at elevated temperatures.* Electrophoresis, 2005. **26**(3): p. 501-510.

31. Davis, J.L., et al., *Method to identify and minimize artifacts induced by fluorescent impurities in single-molecule localization microscopy.* Journal of Biomedical Optics, 2018. **23**(10).

32. Zhao, M.C., et al., *Ultralow- and Low-Background Surfaces for Single-Molecule Localization Microscopy of Multistep Biointerfaces for Single-Molecule Sensing.* Langmuir, 2018. **34**(34): p. 10012-10018.

33. Zhen, G.L., et al., *NTA-functionalized poly(L-lysine)-g-poly(ethylene glycol): A polymeric interface for binding and studying 6xHis-tagged proteins.* 2005 27th Annual International Conference of the Ieee Engineering in Medicine and Biology Society, Vols 1-7, 2005: p. 1036-1038.

34. Dempsey, G.T., et al., *Photoswitching Mechanism of Cyanine Dyes.* Journal of the American Chemical Society, 2009. **131**(51): p. 18192-+.

35. Uno, S.N., et al., *A spontaneously blinking fluorophore based on intramolecular spirocyclization for live-cell super-resolution imaging.* Nature Chemistry, 2014. **6**(8): p. 681-689.

36. Ovesny, M., et al., *ThunderSTORM: a comprehensive ImageJ plug-in for PALM and STORM data analysis and super-resolution imaging.* Bioinformatics, 2014. **30**(16): p. 2389-2390.

37. Weber, K., P.C. Rathke, and M. Osborn, *Cytoplasmic Microtubular Images in Glutaraldehyde-Fixed Tissue-Culture Cells by Electron-Microscopy and by Immunofluorescence Microscopy.* Proceedings of the National Academy of Sciences of the United States of America, 1978. **75**(4): p. 1820-1824.

38. Remmel, M., et al., *Spontaneously blinking fluorophores for accelerated MINFLUX nanoscopy*. bioRxiv, 2022: p. 2022.08.29.505670.

39. Muller-Reichert, T., et al., *Structural changes at microtubule ends accompanying GTP hydrolysis: Information from a slowly hydrolyzable analogue of GTP, guanylyl (alpha,beta)methylenediphosphonate.* Proceedings of the National Academy of Sciences of the United States of America, 1998. **95**(7): p. 3661-3666.

40. Nicholas, M.P., L. Rao, and A. Gennerich, *Covalent Immobilization of Microtubules on Glass Surfaces for Molecular Motor Force Measurements and Other Single-Molecule Assays.* Mitosis: Methods and Protocols, 2014. **1136**: p. 137-169.

41. Kuo, Y.W., et al., *The force required to remove tubulin from the microtubule lattice by pulling on its alpha-tubulin C-terminal tail.* Nature Communications, 2022. **13**(1).

42. Mandelkow, E. and E.M. Mandelkow, *Kinesin motors and disease.* Trends in Cell Biology, 2002. **12**(12): p. 585-591.

43. Mickolajczyk, K.J. and W.O. Hancock, *Kinesin Processivity Is Determined by a Kinetic Race from a Vulnerable One-Head-Bound State.* Biophysical Journal, 2017. **112**(12): p. 2615-2623.

44. Mickolajczyk, K.J., et al., *Kinetics of nucleotide-dependent structural transitions in the kinesin-1 hydrolysis cycle.* Proceedings of the National Academy of Sciences of the United States of America, 2015. **112**(52): p. E7186-E7193.

45. Isojima, H., et al., *Direct observation of intermediate states during the stepping motion of kinesin-1*. Nature Chemical Biology, 2016. **12**(4): p. 290-+.

46. Hua, W., J. Chung, and J. Gelles, *Distinguishing inchworm and hand-over-hand processive kinesin movement by neck rotation measurements.* Science, 2002. **295**(5556): p. 844-848.

47. Gutierrez-Medina, B., A.N. Fehr, and S.M. Block, *Direct measurements of kinesin torsional properties reveal flexible domains and occasional stalk reversals during stepping.* Proceedings of the National Academy of Sciences of the United States of America, 2009. **106**(40): p. 17007-17012.

48. Ramaiya, A., et al., *Kinesin rotates unidirectionally and generates torque while walking on microtubules.* Proceedings of the National Academy of Sciences of the United States of America, 2017. **114**(41): p. 10894-10899.

49. Milic, B., et al., *Kinesin processivity is gated by phosphate release.* Proceedings of the National Academy of Sciences of the United States of America, 2014. **111**(39): p. 14136-14140.

50. Takaki, R., et al., *How kinesin waits for ATP affects the nucleotide and load dependence of the stepping kinetics.* Proceedings of the National Academy of Sciences of the United States of America, 2019. **116**(46): p. 23091-23099.

51. Rosenfeld, S.S., G.M. Jefferson, and P.H. King, *ATP reorients the neck linker of kinesin in two sequential steps.* Journal of Biological Chemistry, 2001. **276**(43): p. 40167-40174.

52. Cross, R.A., *Review: Mechanochemistry of the kinesin-1 ATPase.* Biopolymers, 2016. **105**(8): p. 476-82.

53. Ebneth, A., et al., *Overexpression of tau protein inhibits kinesin-dependent trafficking of vesicles, mitochondria, and endoplasmic reticulum: Implications for Alzheimer's disease.* Journal of Cell Biology, 1998. **143**(3): p. 777-794.

54. Dixit, R., et al., *Differential regulation of dynein and kinesin motor proteins by tau.* Science, 2008. **319**(5866): p. 1086-1089.

55. Schneider, R., et al., *Kinesin-1 Motors Can Circumvent Permanent Roadblocks by Side-Shifting to Neighboring Protofilaments.* Biophysical Journal, 2015. **108**(9): p. 2249-2257.

56. Ferro, L.S., et al., *Kinesin and dynein use distinct mechanisms to bypass obstacles.* Elife, 2019. **8**.

57. Deguchi, T., et al., *Direct observation of motor protein stepping in living cells using MINFLUX*. bioRxiv, 2022: p. 2022.07.25.500391.

58. Wolff, J.O., et al., *MINFLUX dissects the unimpeded walking of kinesin-1*. bioRxiv, 2022: p. 2022.07.25.501426.

Appendix

Methods

Construction of *in vitro* assays

Flow chambers were constructed by taping an oxygen plasma-cleaned coverslip with two double-sided adhesive tapes to an objective slide. In vitro assays were created by incubating a flow chamber with PLL-bt (0.2 mg/ml in ddH2O, PLL-PEG-biotin (PLL(20)-g[3.5]- PEG(2)/PEG(3.4)- biotin(20%), Susos AG Inc.) or PLL-NTA (0.2 mg/ml in ddH2O, PLL-PEG-biotin (PLL(20)-g[3.5]- PEG(3.4)-NTA , Susos AG Inc.) or bovine serum albumin (BSA or BSA-bt, 1mg/ml, Sigma) for 15 minutes. The flow chamber was rinsed with buffer and incubated with NVD (30 µg/ml) or NiCl2 (10 µg/ml) for 5 minutes. The flow chamber was rinsed with buffer and incubated with bt-AB (Biotin-SP (long spacer) AffiniPure Rabbit Anti-Mouse IgG (H+L), Jackson immunoresearch) or his-HaloTag7 (produced by the protein expression facility of the MPIMF). The assay was completed by finally adding the conjugated fluorophore.

Live/fixed cell labeling

Live cells were grown in Lab-Tek chambers and labeled over night with (usually) 100 nM dye in cell medium. Subsequently, cells were washed with cell medium and imaged. Fixed cells were prepared by methanol (MeOH, -20 °C, 10 min) fixation and washed with PBS. Primary antibody was added and, after washing, the polyclonal antibody labeled with the (spontaneously blinking) fluorophore was added. After a final washing step, cells were imaged.

Kinesin expression and purification

Cysteine-light human kinesin-1 constructs (truncated at amino acid position 560) were expressed in E. Coli. The plasmids used were K560CLM T324C (#24460, Addgene), K560CLM E215C (provided by the Yildiz Lab, University of California, Berkeley), and K560CLM K28C and K560CLM N356C both produced by QuikChange site-directed mutagenesis of CLM RP HTR (#24430, Addgene) (using PfuUltra HF polymerase (600380-51), Agilent) as described by Tomishige et al.. The plasmid sequences were verified by DNA sequencing. Constructs were purified via their C-terminal His_6-Tag using a 5 ml HisTrap FF (GE17-5255-01, Cytiva). Aliquots of the purified protein (in 25 mM piperazine-N,N′-bis(2-ethanesulfonic acid) (PIPES, P-1851, Sigma-Aldrich) pH 6.8, 2 mM $MgCl_2$ (1.05833.0250, Merck), 1 mM ethylene glycol-bis(2-aminoethylether)-N,N,N′,N′-tetraacetic acid (EGTA, E3889, Sigma-Aldrich), 0.1 mM ATP (BP413-25, Fisher Scientific), 0.2 mM TCEP (J60316, Alfa Aesar), around 300 mM NaCl (1.06404.1000, Sigma-Aldrich), 10% (m/v) sucrose (S1888, Sigma-Aldrich) were flash frozen with liquid nitrogen and stored at -80°C.

Kinesin labeling

Kinesin was labeled with ATTO 647N-maleimide (in DMSO, AD 647N-41, ATTO-TEC) added to the thawed solution of kinesin over night at 4°C. Labeled protein was purified using size-exclusion chromatography (PD MiniTrap G-25, 28-9180-07, Cytiva) according to the manufacturer's protocol with PEM80 buffer (80 mM PIPES, 0.5 mM EGTA, 2 mM $MgCl_2$, pH 7.4). The degree of labeling (DOL) was determined by mass spectrometry (ESI, maXis II ETD, Bruker) and confirmed by UV-Vis spectroscopy (DS-11+ Spectrophotometer, DeNovix). Sucrose was added to the labeled protein to a concentration of 10% (w/v). The aliquots of labeled kinesin were flash-frozen with liquid nitrogen and stored at -80°C.

For labeling kinesin constructs with Cy3B (for MINSTED tracking experiments), kinesin was labeled with Cy3B-maleimide (in DMSO) added to the thawed solution of kinesin for 2 h at room temperature and subsequently purified and treated according to the aforementioned procedure.

Microtubule polymerization

Biotinylated and fluorescently labeled microtubules (bt-MT-AF488) were polymerized from a mixture of 88% (highly pure) Cycled Tubulin (032005, PurSolutions, LLC), 10% labeled Tubulin-Biotin-XX (033305, PurSolutions, LLC) and 2% labeled Tubulin-Alexa Fluor 488 (048805, PurSolutions, LLC). For polymerization, the lyophilized tubulin components were suspended in PEM80 buffer with 1 mM guanosine-5'-[(α,β)-methyleno]triphosphate (GMPCPP; NU-405S, Jena Bioscience) and the solution was incubated on ice for 5 min to enhance GMPCPP binding to tubulin. To remove protein aggregates, the solution was centrifuged for 5 min at 21,000 × g in a bench-top microcentrifuge (Fresco 21, Thermo Scientific). The supernatant was incubated for 1 h at 37°C to trigger polymerization. The polymerized microtubules were centrifuged down at 21,000x g for 15 min, washed with PEM80 and centrifuged at 21,000 × g for 15 min. Subsequently, the microtubule pellet was resuspended in PEM80, aliquoted, flash-frozen in liquid nitrogen and stored at -80°C.

Construction of kinesin motility assays

The kinesin motility assay was created in a flow chamber. incubated with microtubules diluted in PEM80 with 10 ug/ml cabazitaxel (FC19621, Biosynth Carbosynth) for 5 min, rinsed with PEM80, incubated with 100 µg/ml biotinylated bovine serum albumin (BSA-bt; A8549-10MG, Sigma-Aldrich) in PEM80 for blocking for 30 min, and subsequently rinsed with PM15 buffer (15 mM PIPES, 2 mM $MgCl_2$, pH 7.4). Labeled kinesin solution was added to measuring buffer (1 mM 1,4-dithiothreitol (DTT, 6908.1, Carl Roth), 1 mM paclitaxel (10-2095, Focus Biomolecules), 10 µg/ml BSA-bt, 1 mM methyl viologen (AC227320010, Acros Organics), 1 mM ascorbic acid (255564, Sigma-Aldrich), 10 µM/100 µM/1 mM adenosine 5′-triphosphate (ATP; A3377-1G, Sigma-Aldrich) or 1 mM ATPγS (NU-406-5, Jena Bioscience) in PM15 buffer) and added to a kinesin motility assay in an Invivo2 Plus Hypoxia Workstation (0.3% O_2, 0.1% CO_2, 99.6% N_2; Baker Ruskinn). The flow chamber was sealed with picodent twinsil speed 22 or nail polish and subsequently measured.

MINFLUX tracking routine

MINFLUX traces were recorded by scanning a region of interest (ROI) or a single pixel on a microtubule with a confocal beam. The MINFLUX tracking routine was triggered when fluorescent signal crossed a set threshold. During the routine, L was decreased in up to five iterations and for the rest of the measurement, the smallest L was used. Per cycle, three positions [-L/2, 0, L/2] were addressed with the excitation minimum by the phase-scanner. Evaluation of the detected photons per position allowed updating the position estimate of the fluorophore. A single 2D-localization (with three iterations per dimension) took (for most measurement routines) a total of 631 µs.

More details are provided in the publication[58].

MINSTED tracking routine

Kinesins were tracked with 100 mW depletion power for ATTO 647N experiments and with 40 mW depletion power for Cy3B experiments. A region of interest around a microtubule was continuously scanned with a confocal excitation beam and the MINSTED routine triggered when a set threshold of detected fluorescence photons was reached.
Traces were filtered (for Cy3B data: net displacement > 20 nm; aspect ratio > 2, spatial sigma < 2 nm; for ATTO 647N data: trace duration > 60 ms, net displacement > 80 nm; aspect ratio > 2, spatial sigma < 2 nm) and plotted in a Matlab script. Steps were fitted with a step-finding algorithm in Matlab.

TIRF imaging conditions and kymograph analysis

For kinesin tracking at 1 µM ATP and at 1 mM ATPγS, the exposure time per frame and the 642 nm laser power were set to 10 s and 10 µW, and for measurements at 1 mM ATP to 100 ms and 300 µW. Imaged with these parameters, single kinesins (construct T324C) labeled with ATTO 647N immobilized on microtubules using the non-hydrolyzing ATP analogue adenylyl-imidodiphosphate (AMP-PNP, A2647-5MG, Sigma Aldrich) did not significantly bleach over average run times. Microtubules were recorded at 2 µW 473 nm laser power. All laser powers were measured in the back focal plane of the objective. Frame series were analyzed with the KymographBuilder in Fiji to determine the run length along microtubules.

Supplementary Tables

Table A4.1: Degree of labeling (DOL) determined from UV-Vis and Mass spectrometry (MS) data.

Construct	UV-Vis				MS			
	A(280 nm)	A(650 nm)	DOL (monomer)	DOL (dimer)	Intensity (labeled) x 10E6	Intensity (unlabeled) x 10E6	DOL (monomer)	DOL (dimer)
K28C	0.9618	0.486	0.3	0.60	2.8	5.4	0.34	0.68
E215C	0.7468	0.1752	0.14	0.28	0.2	1	0.17	0.33
T324C	0.5809	0.2495	0.25	0.50	0.7	2.7	0.21	0.41
N356C	0.8487	0.3176	0.22	0.44	2.3	7	0.25	0.49
N356C-dol2	0.7445	0.9701	0.79	1.58	8.2	0	1.00	2.00

Table A4.2: Absorbance at 650 nm from different amounts of phosphate (Pi) for the calibration curve.

n(Pi) [nmol]	Absorbance at 650 nm
0	0.173
0.3	0.366
0.5	0.525
1	0.819
2	1.157

Table A4.3: Absorbance values for unlabeled and labeled kinesin-1 constructs.

	Absorbance at 650 nm with ATP	Absorbance at 650 nm without ATP
K215C	1.494	0.180
K324C	1.318	0.182
E215C-ATTO 647N	1.295	0.169
T324C-ATTO 647N	1.230	0.158
KR01	1.406	0.180

Table A4.4: Absorbance values for microtubules (MT) with stabilizing additives (Txl, cTxl, VF488-tub), snap-freezing treatment (-80°C) and biotin modification (bt-MT) for labeled kinesin-1 constructs.

	Absorbance at 650 nm	Absorbance at 650 nm
	E215C-ATTO 647N	T324C-ATTO 647N
MT(Txl)	1.280	1.298
MT(cTxl)	1.548	1.470
MT(VF488-tub)	1.214	1.131
MT(Txl,-80°C)	2.098	1.617
bt-MT (20%)	1.682	1.610
bt-MT (2%)	1.742	1.873
no MT	0.346	0.259

Supplementary Figures

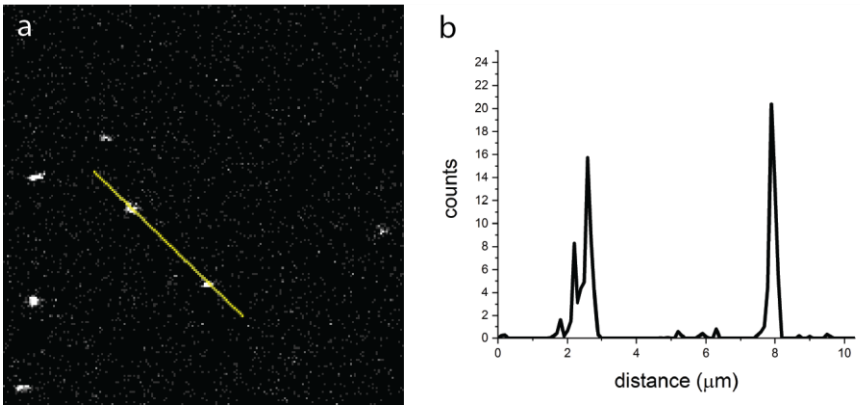

Figure A1.1: (**a**) Confocal image of a control of the PLL-bt assay for immobilization of biotinylated fluorophores with profile (yellow) over two fluorescent spots. Size: 20 μm*20 μm; Scalebar min/max: 0/27. (**b**) Detected photon counts over profile in (a).

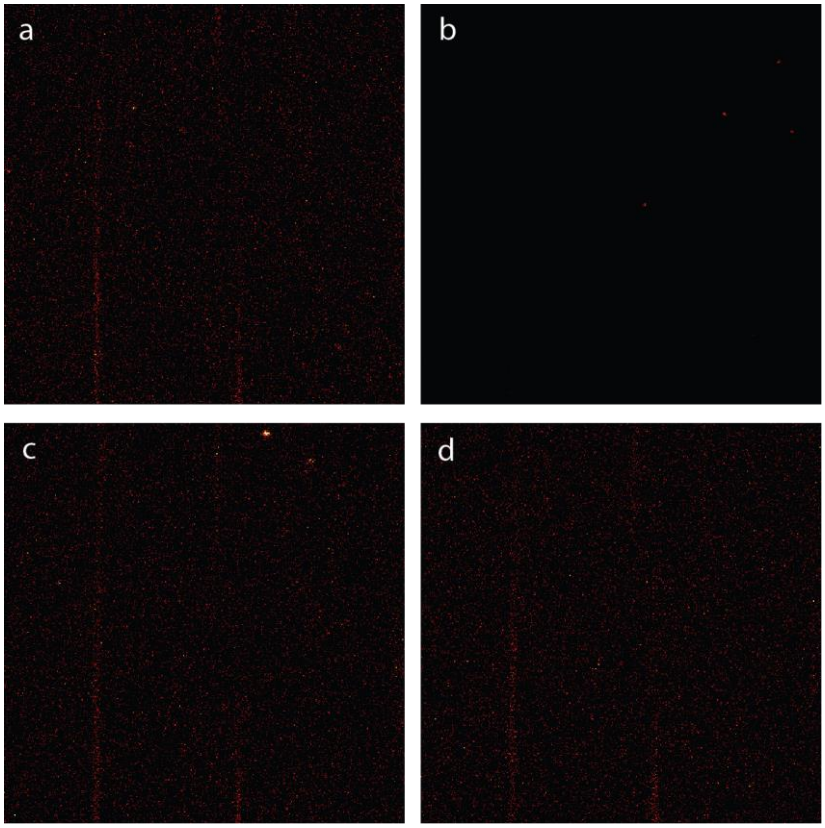

Figure A1.2: Confocal images of the controls for the PLL-bt assay for immobilization of fluorescently labeled antibodies (AB-AF647)/nanobodies (NB-AF647). (**a**) Control for AB-AF647 immobilization with NVD omitted. (**b**) Control for NB-AF647 immobilization with NVD omitted. (**c**) Control for NB-AF647 immobilization with bt-AB omitted. (**d**) Control for NB-AF647 immobilization with NVD and bt-AB omitted. Size: a/b/c/d: 50 μm*50 μm; Scalebar min/max: a/b/c/d: 0/5.

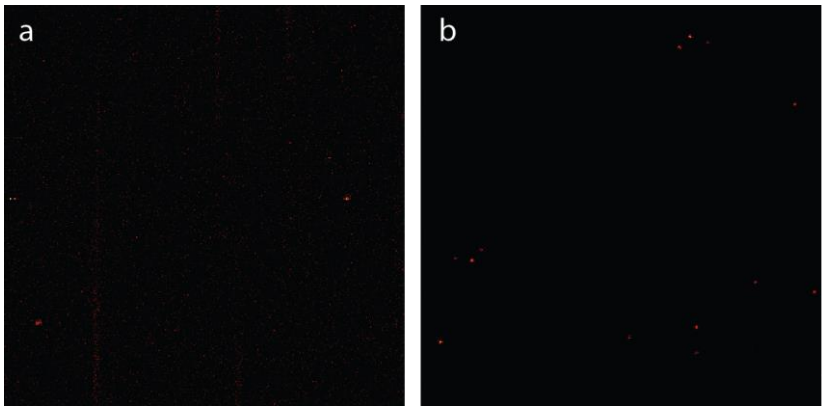

Figure A1.3: Confocal images of the biotin and T20 controls for the PLL-bt assay for immobilization of fluorescently labeled antibodies nanobodies (NB-AF647). (**a**) Control with biotin added prior to bt-AB incubation shows reduced surface coverage of NB-AF647. (**b**) Control with T20 omitted from PLL-bt/T20 and biotin added prior to bt-AB incubation shows higher surface coverage of NB-AF647 compared to (a), highlighting the surface blocking function of Tween-20. Size: a/b: 50 μm*50 μm; Scalebar min/max: a/b: 0/50.

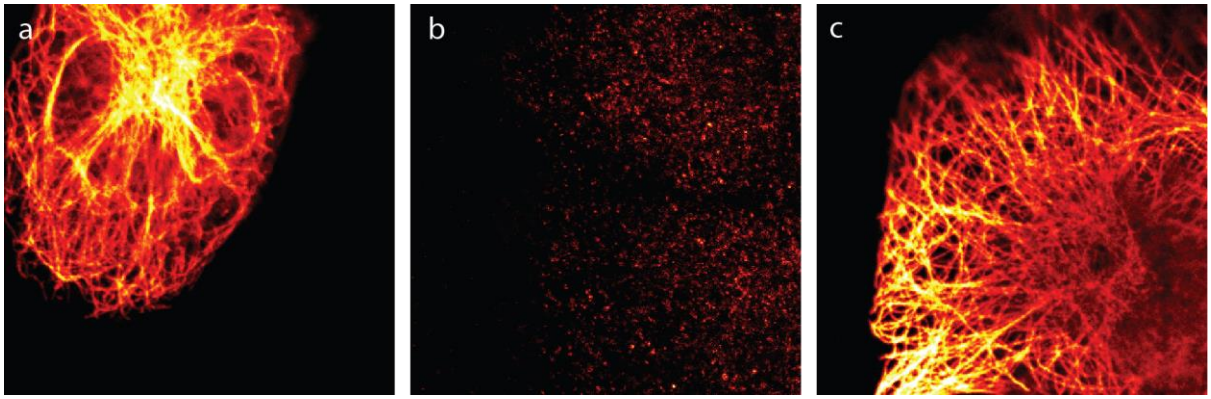

Figure A1.4: Confocal images the U2OS fixed (MeOH) cell controls for bt-AB functionality. (**a**) Control with primary anti-tubulin mouse antibody and anti-mouse nanobody (NB-AF647). (**b**) Control with primary rabbit anti-tubulin antibody and anti-mouse nanobody (NB-AF647). (**c**) Control with primary rabbit anti-tubulin antibody, bt-AB (mouse, anti-rabbit) and anti-mouse nanobody (NB-AF647). Size: a/b/c: 40 µm*40 µm; Scalebar min/max: a/c: 0/1000, b: 0/50.

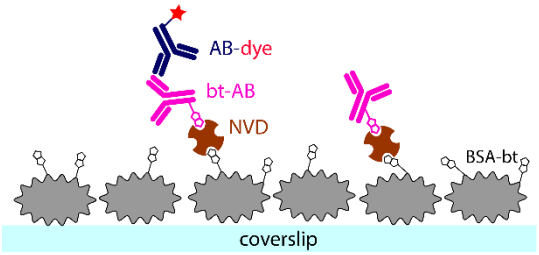

Figure A1.5: Illustration of the BSA-bt assay for immobilization of fluorescently labeled antibodies/nanobodies via neutravidin (NVD) and biotinylated primary antibody (bt-AB).

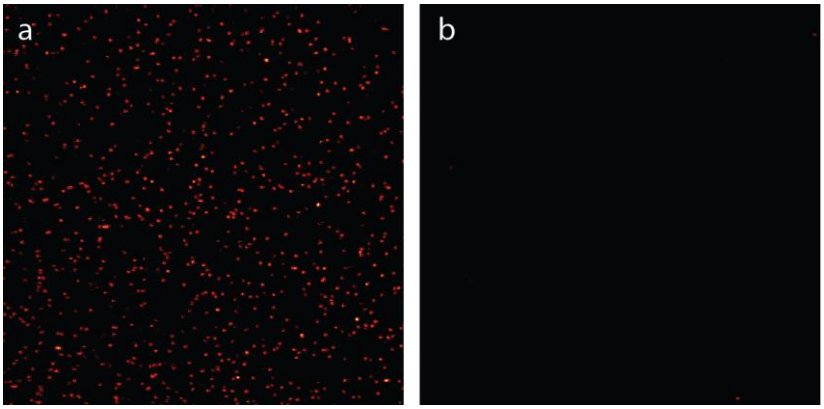

Figure A1.6: Confocal images of (**a**) the complete PLL-NTA assay for immobilization of chloroalkane-functionalized fluorophore (halo-fluorophore) via his-tagged HaloTag (his-HT) and Ni^{2+} and (**b**) the assay after incubation of imidazole (100 mM). Imidazole incubation drastically reduced fluorophore coverage. Size: a/b: 50 µm*50 µm; Scalebar min/max: a/b: 0/50.

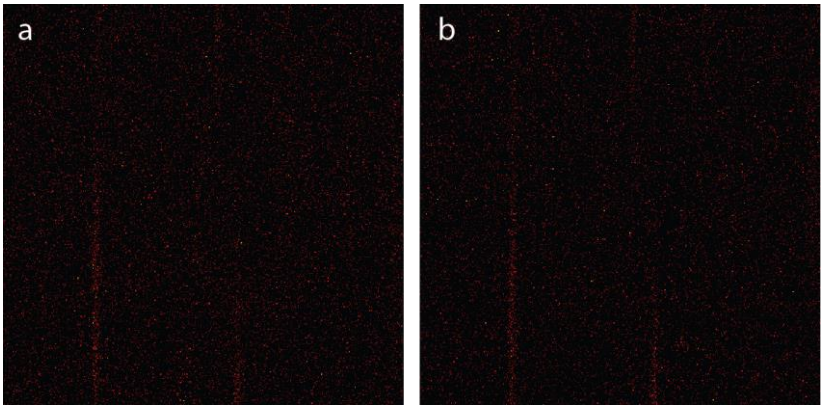

Figure A1.7: Confocal images of control samples for the PLL-NTA assay for immobilization of chloroalkane-functionalized fluorophore (halo-fluorophore) via his-tagged HaloTag (his-HT) and Ni^{2+}. (**a**) Control sample with halo-SiR added to the glass coverslip previously incubated with $NiCl_2$. (**b**) Control sample with his-HT omitted from the complete PLL-NTA assay. Size: a/b: 50 µm*50 µm; Scalebar min/max: a/b: 0/5.

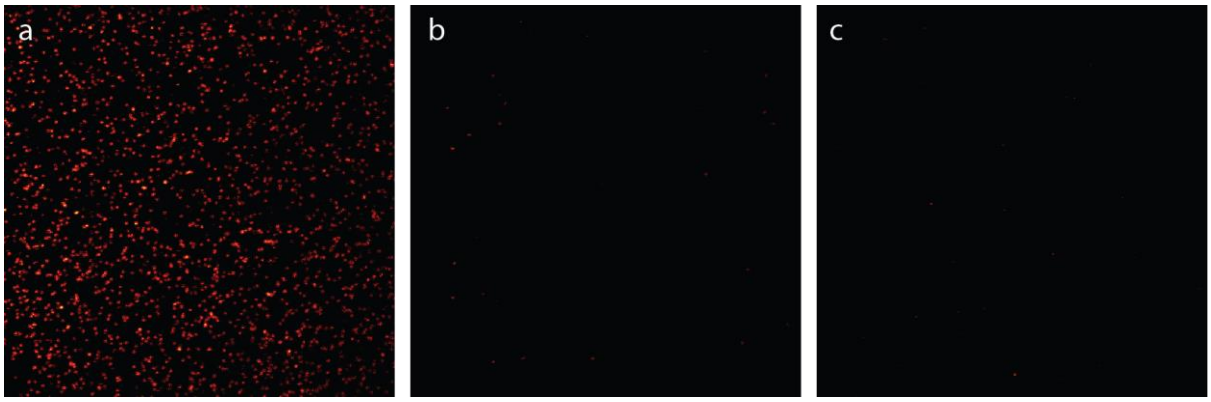

Figure A1.8: Confocal images of (**a**) the complete PLL-NTA assay for immobilization of benzylguanine-functionalized fluorophore (BG-fluorophore) via his-tagged SNAP-tag (his-SNAP) and Ni^{2+} and (**b**) the assay after incubation of imidazole (100 mM). Imidazole incubation drastically reduced fluorophore coverage. (**c**) Control sample with his-SNAP omitted from the complete PLL-NTA assay. Size: a/b/c: 50 µm*50 µm; Scalebar min/max: a/b/c: 0/50.

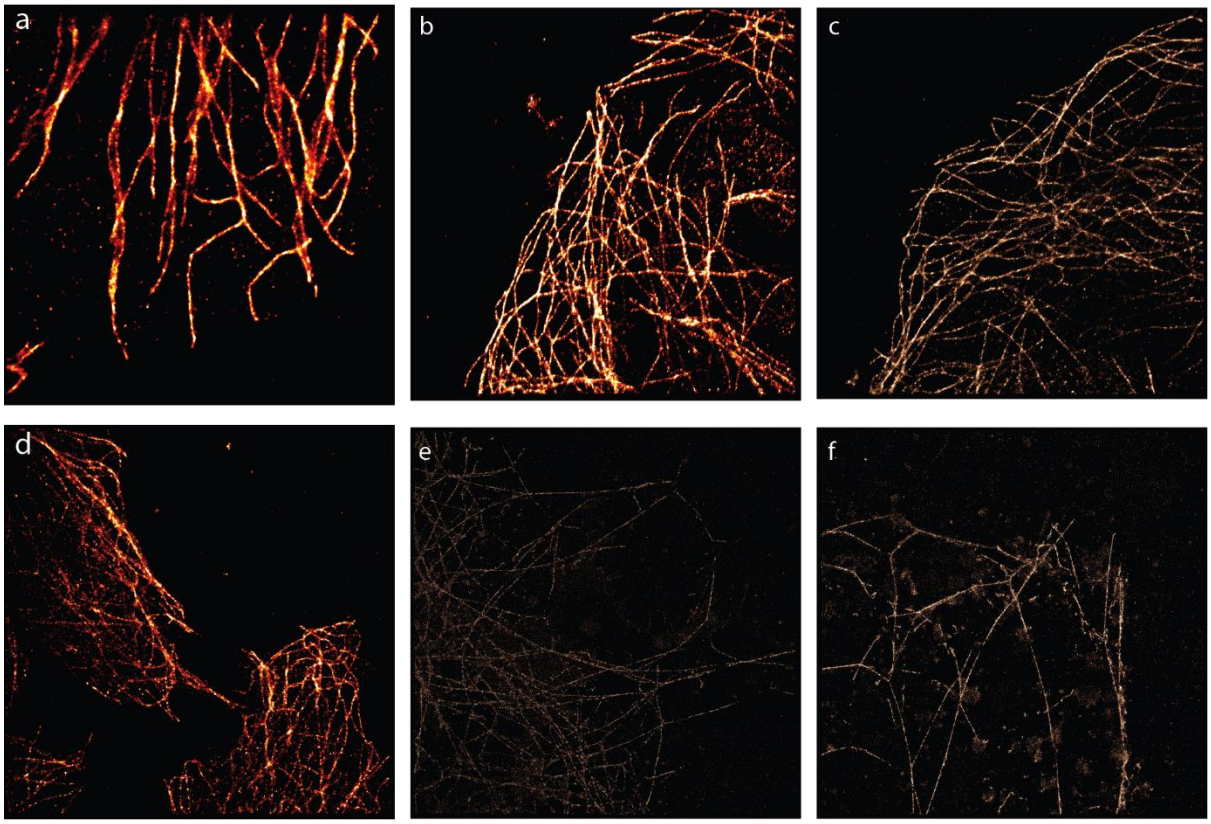

Figure A2.1: STORM images of U2OS cells fixed with MeOH and labeled with a primary antibody (rabbit, anti-tubulin) and (**a**) ar-223, (**b**) ar-224, (**c**) ar-259 and (**d**) ar-657. STORM images of living U2OS-vim-halo cells labeled with 100 nM (**e**) halo-657 and (**f**) halo-5-HMSiR. Imaging intensity (640 nm): 22 kW/cm^2; dwell time: 20 ms. Size: a: 12.8 µm*13.1 µm, b: 25.6 µm*25.7 µm, c: 25.6 µm*25.6 µm, d: 25.5 µm*25.7 µm, e: 25.6 µm*25.6 µm, f: 25.6 µm*25.6 µm; Scalebar min/max: a: 0/255, b: 0/50, c: 0/8, d: 50, e: 1/5, f: 0/4.

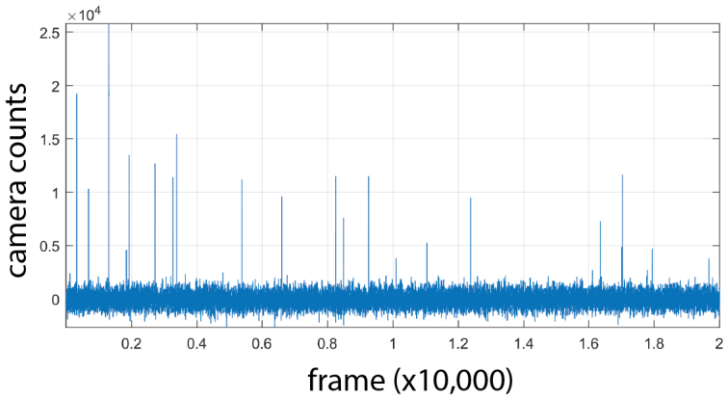

Figure A2.2: Exemplary single molecule trace (camera counts over time with 10 ms per frame) extracted from a STORM image sequence using ThunderSTORM and Matlab analysis. Sample: ar-657 immobilized on PLL-bt/T20 via NVD and bt-AB. The laser intensity of in the sample plane was ~22 kW/cm^2 and the time resolution was 10 ms. The on-events are clearly distinguishable from the comparably low background.

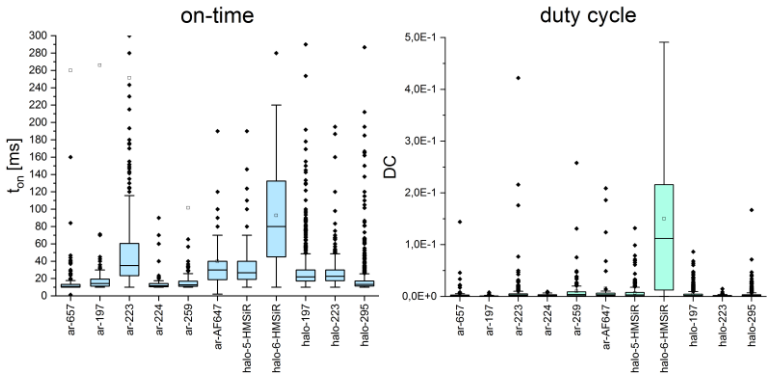

Figure A2.3: Zoomed-out, full data box plots of on-times and duty cycle for the spontaneous blinkers attached to antibodies or HaloTag. The boxes represents the middle 50% of data and the horizontal line in the boxes is the median. The whiskers represent 1.5 times the interquartile range. Data points outside of the range are outliers and denoted with a ♦ symbol. The mean is denoted by the □ symbol.

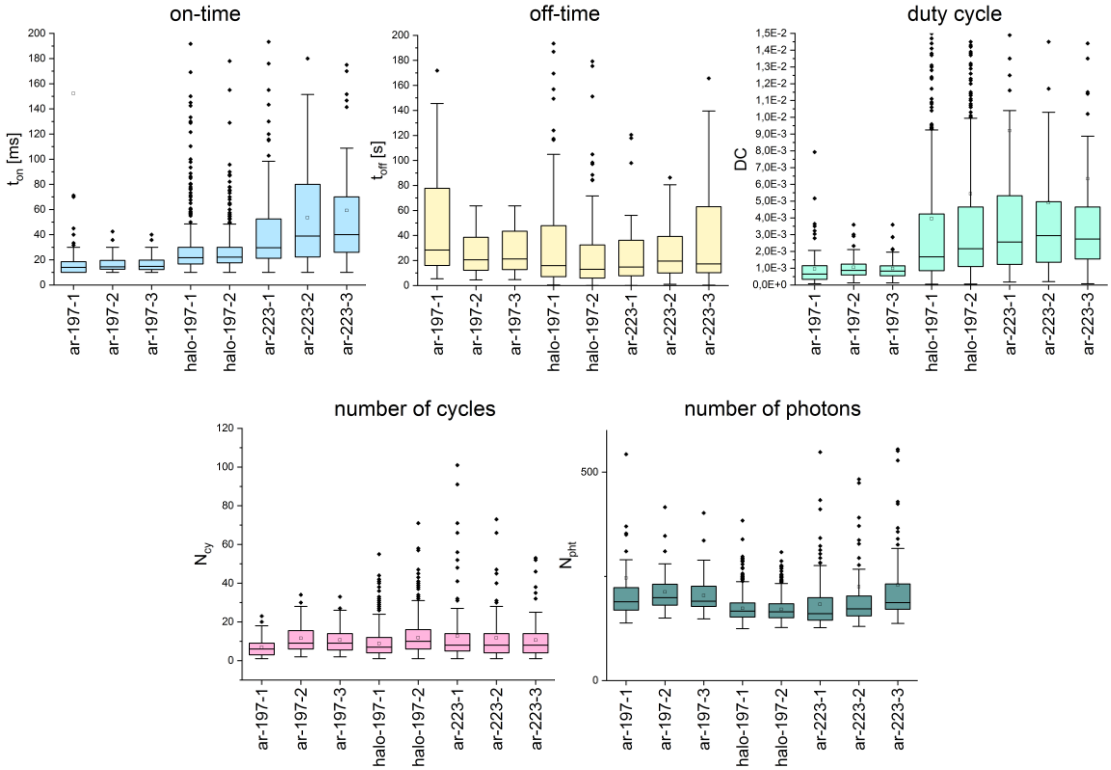

Figure A2.4: Subset comparison to test intrinsic heterogeneity. Box plots of on-times, off-times, duty cycle, number of cycles and number of photons per blinking event for the subsets of ar-197, halo-197 and ar-223. The boxes represents the middle 50% of data and the horizontal line in the boxes is the median. The whiskers represent 1.5 times the interquartile range. Data points outside of the range are outliers and denoted with a ♦ symbol. The mean is denoted by the □ symbol.

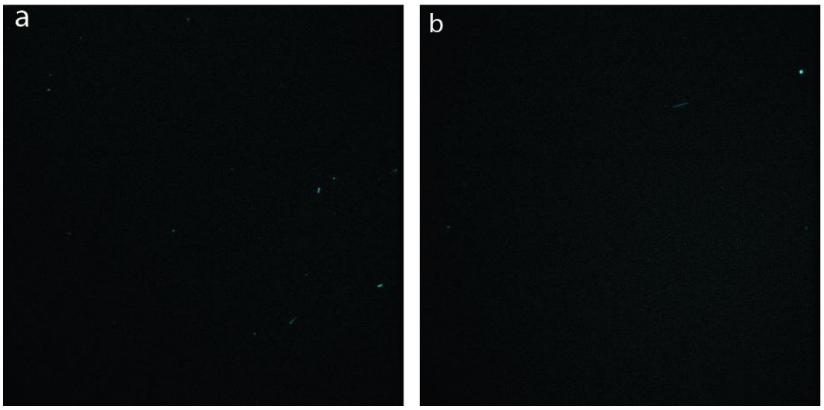

Figure A3.1: Confocal images of the controls of the antibody assay with PLL-bt, NVD, bt-DM1A and microtubules with (**a**) NVD and bt-DM1A omitted and (**b**) the concentration of NVD reduced tenfold. Size: a/b: 80 µm*80 µm; Scalebar min/max: a/b: 0/50.

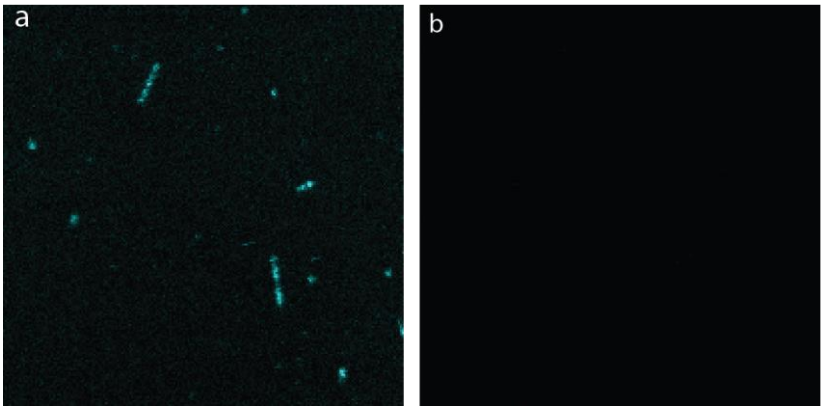

Figure A3.2: Confocal images of two color channels of (**a**) microtubules (bt-MT-AF488) immobilized via the biotinylated microtubule assay and (**b**) the secondary antibody labeled with Alexa Fluor 647 with the primary rabbit antibody (anti α-tubulin) omitted. Size: a/b: 20 µm*20 µm; Scalebar min/max: a: 0/50, b: 0/2000.

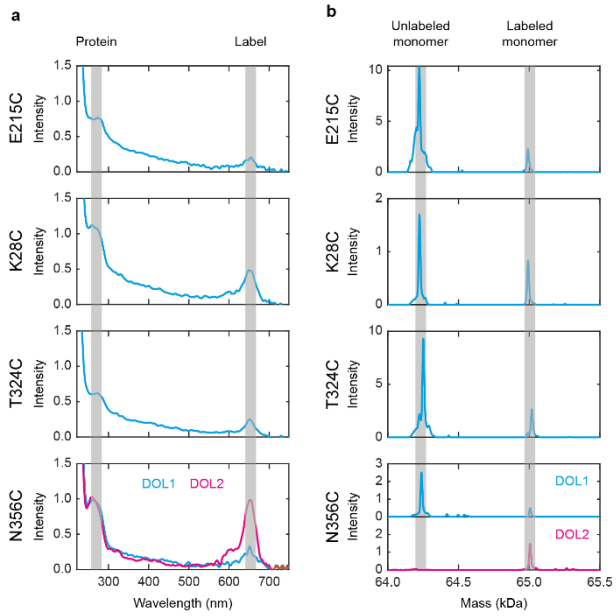

Figure A4.1: (**a**) UV-Vis spectra and (**b**) mass spectrometry (ESI) spectra of kinesin constructs labeled with maleimide-ATTO 647N. For (a), the absorption peaks of the protein (280 nm) and the fluorophore (650 nm) are highlighted. For (b), the peaks of the unlabeled and labeled monomers are highlighted.

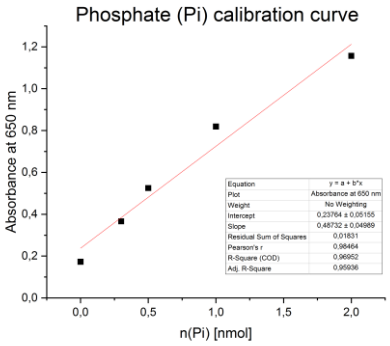

Figure A4.2: Calibration curve for calculation of Pi produced and ATP consumed. A linear fit of data gave: A(650 nm)=0.48732*n(Pi)+0.23764.

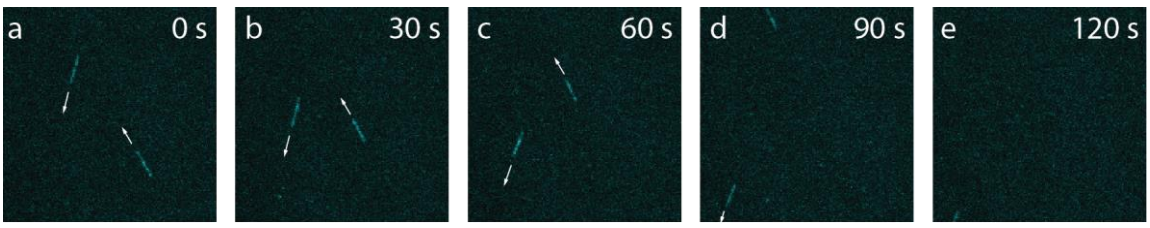

Figure A4.3: Confocal images of microtubules (labeled with VF488-tub) on a kinesin inverted assay (KIA) based on PLL-NTA/T20 with time increments of ~30 seconds. The microtubules are moved by the immobilized E215C-ATTO 647N in the presence of 1 mM ATP in the direction of the white arrows.

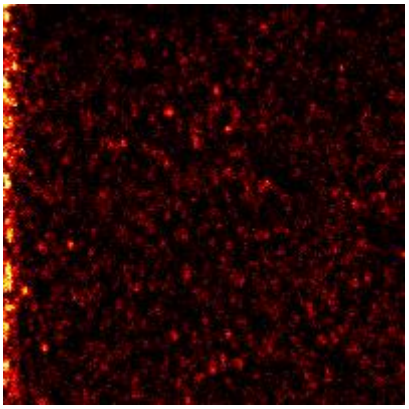

Figure A4.4: Confocal image showing strong (non-single-molecule) coverage with immobilized E215C-ATTO 647N in the red channel.

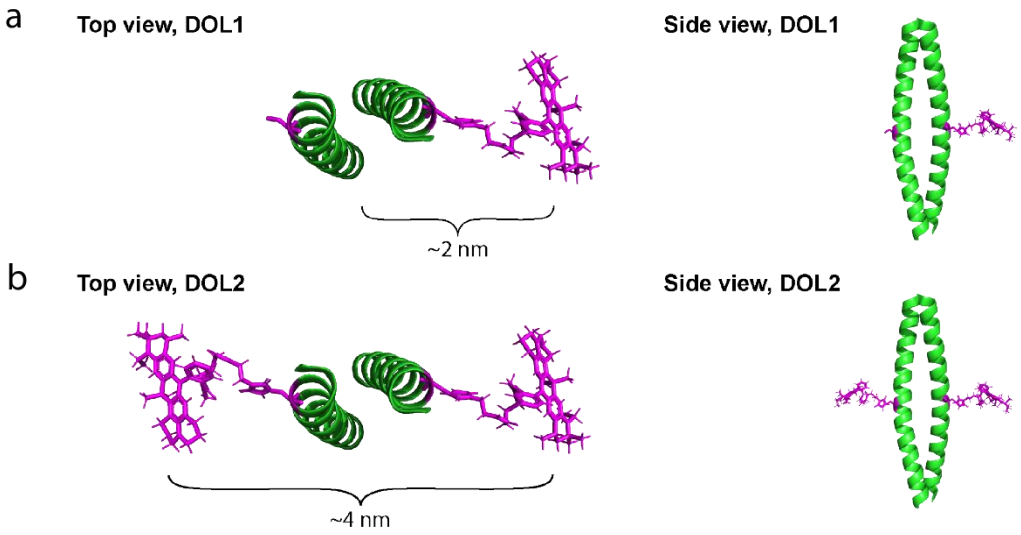

Figure A4.5: Schematic illustration of the coiled-coil stalk domain (green) in N356C labeled with maleimide-ATTO 647N with (**a**) a DOL of one and (**b**) a DOL of two. The labeled amino acid is displaced from the center axis by ~1 nm and the fluorophore (structure determined by MM2 energy minimization in Chem3D Pro (Perkin Elmer) is displaced by another ~1 nm, giving a total displacement of the fluorophore core from the coiled-coil longitudinal axis of ~2 nm. For the coiled-coil crystal structure, the representative parallel coiled-coil dimerization region of cortexillin I (PDB: 1D7M) was used and labeling position S281 chosen.

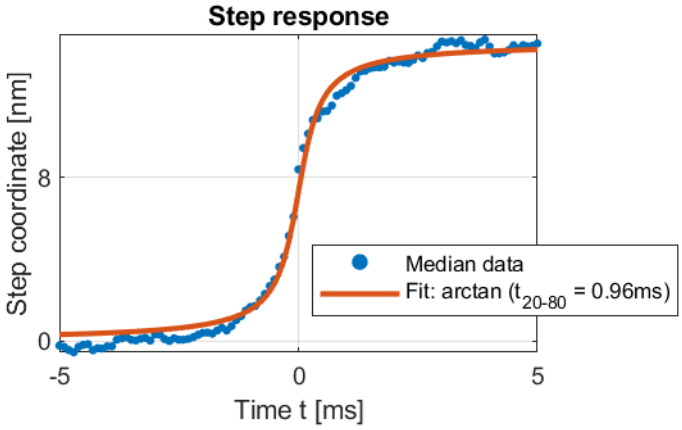

Figure A5.1: Fit of the step response data of a MINSTED experiment (E215C-ATTO 647N with 1 mM ATP) gives sub-millisecond median time resolution.

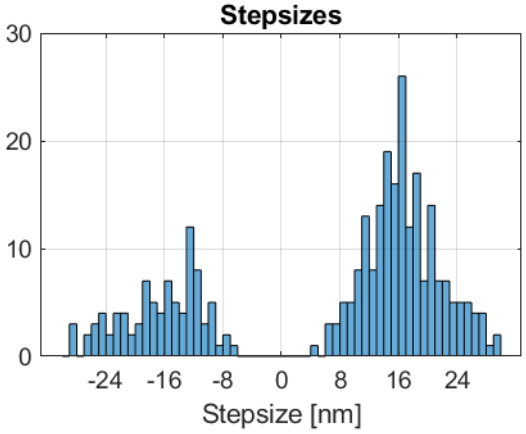

Figure A5.2: Stepsize histogram for E215C-ATTO 647N with 10 µM ATP.

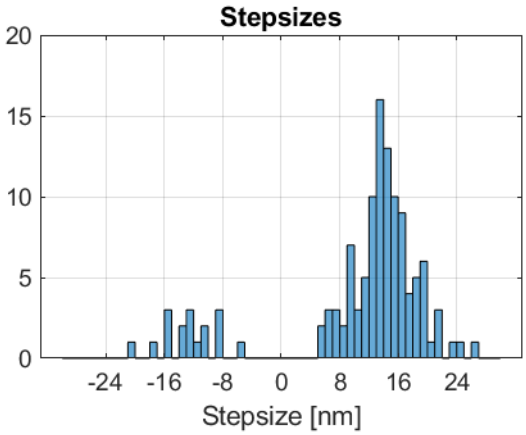

Figure A5.3: Stepsize histogram for E215C-Cy3B with 1 mM ATP.

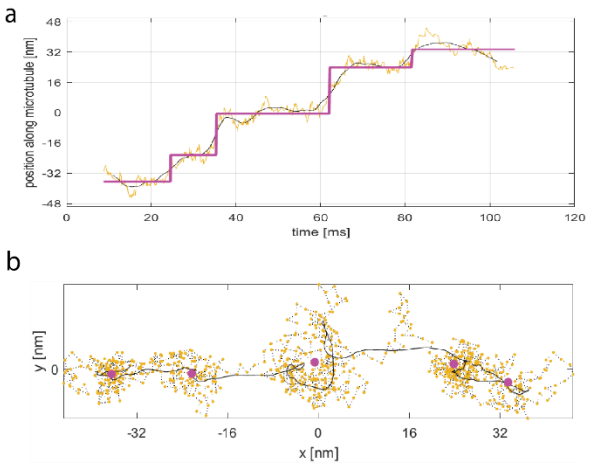

Figure A5.4: Exemplary MINSTED trace of T324C-Cy3B with 1 mM ATP. (**a**) On-axis displacement over time. (**b**) 2D-plot.

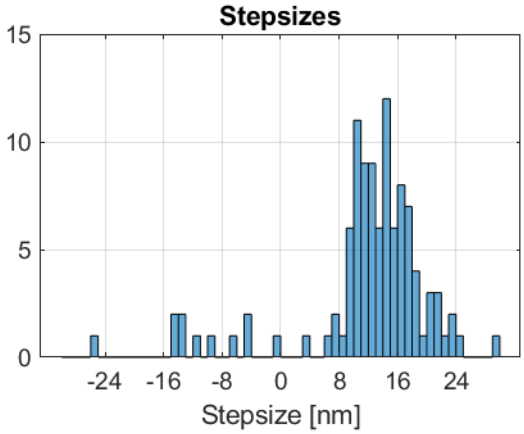

Figure A5.5: Stepsize histogram for T325C-Cy3B with 1 mM ATP.

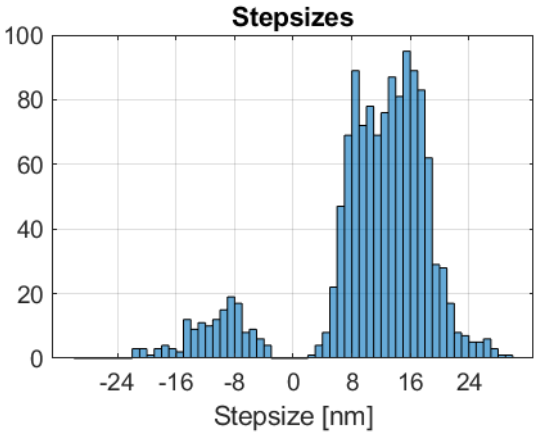

Figure A5.6: Stepsize histogram for K28C-Cy3B with 1 mM ATP.

Eidesstattliche Erklärung

Eidesstattliche Versicherung gemäß § 8 der Promotionsordnung für die Gesamtfakultät für Mathematik, Ingenieur- und Naturwissenschaften der Universität Heidelberg:

1. Bei der eingereichten Dissertation zu dem Thema

"Kinesin-1 stepping dissected with MINFLUX and MINSTED tracking – Spontaneous blinkers for live-cell MINFLUX imaging"

handelt es sich um meine eigenständig erbrachte Leistung.

2. Ich habe nur die angegebenen Quellen und Hilfsmittel benutzt und mich keiner unzulässigen Hilfe Dritter bedient. Insbesondere habe ich wörtlich oder sinngemäß aus anderen Werken übernommene Inhalte als solche kenntlich gemacht.

3. Die Arbeit oder Teile davon habe ich bislang nicht an einer Hochschule des In- oder Auslands als Bestandteil einer Prüfungs- oder Qualifikationsleistung vorgelegt.

4. Die Richtigkeit der vorstehenden Erklärungen bestätige ich.

5. Die Bedeutung der eidesstattlichen Versicherung und die strafrechtlichen Folgen einer unrichtigen oder unvollständigen eidesstattlichen Versicherung sind mir bekannt.

Ich versichere an Eides statt, dass ich nach bestem Wissen die reine Wahrheit erklärt und nichts verschwiegen habe.

---------- ----------

Ort, Datum Unterschrift